RIGA TECHNICAL UNIVERSITY

Genādijs Kobenkins

THE ENSURING OF STABLE VIBRATION-STRENGTH INDICATORS OF GEARED TRACTION MOTORS IN VARIABLE FREQUENCY AND LOAD MODES

Doctoral Thesis

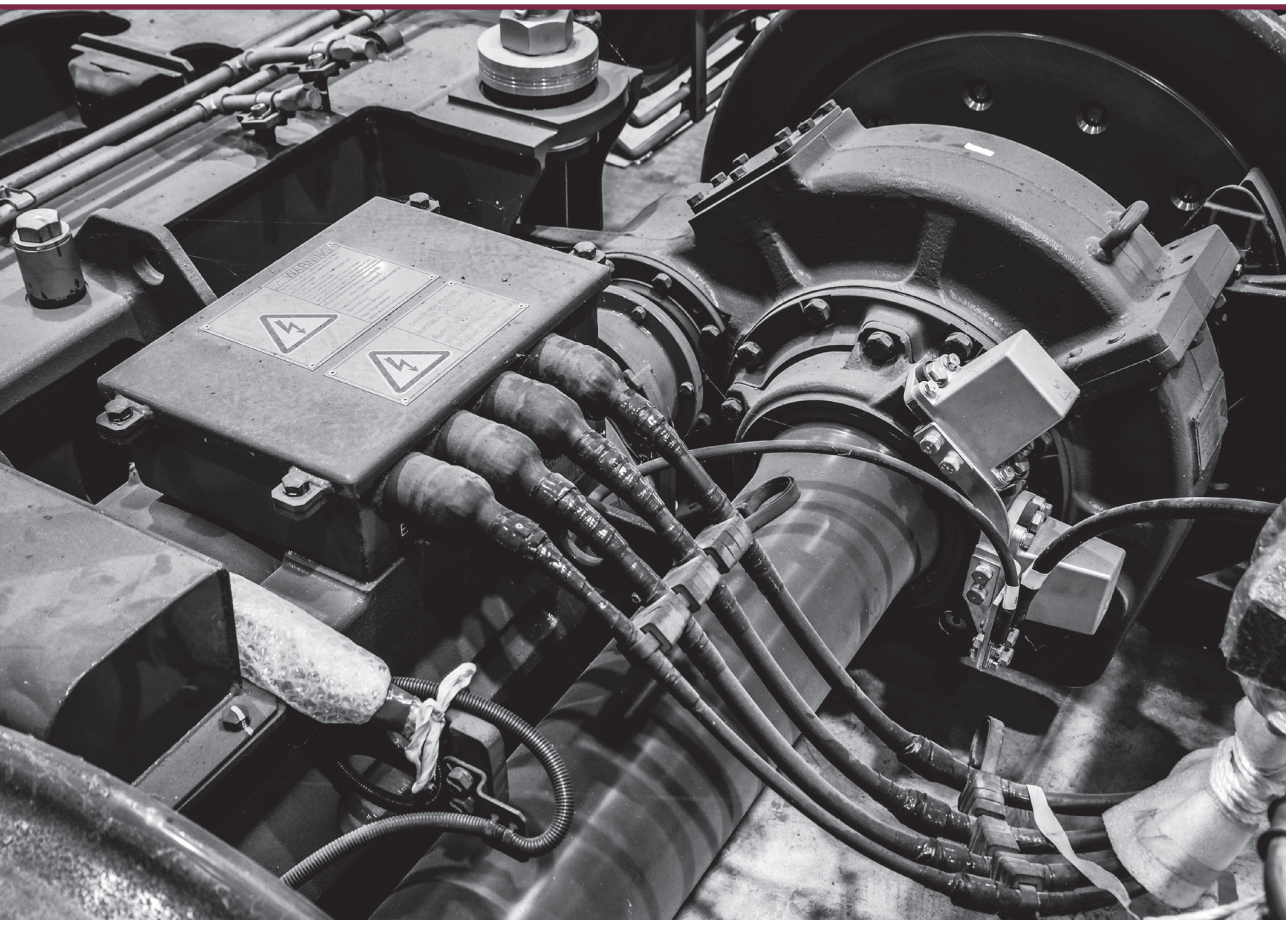

RTU Press
Riga 2025

RIGA TECHNICAL UNIVERSITY
Faculty of Computer Science, Information Technology and Energy
Institute of Industrial Electronics, Electrical Engineering and Energy

Genādijs Kobenkins
Doctoral Student of the Study Programme “Smart Power Systems”

THE ENSURING OF STABLE VIBRATION-STRENGTH INDICATORS OF GEARED TRACTION MOTORS IN VARIABLE FREQUENCY AND LOAD MODES

Doctoral Thesis

Scientific supervisor:
Professor Dr. sc. ing.
ANDREJS PODGORNOVS
Scientific advisor:
Docent Dr. sc. ing.
OĻEGS SĻISKIS

RTU Press
Riga 2025

ACKNOWLEDGMENTS

The doctoral thesis was completed at the Institute of Industrial Electronics, Electrical Engineering and Energy at the Faculty of Computer Science, Information Technology and Energy of the Riga Technical University. I extend my deepest gratitude to my doctoral thesis supervisor, doctor of technical sciences, professor, Dr.sc.ing. Andrejs Podgornovs for providing me the chance to conduct this research and offering valuable guidance on navigating through the project. A crucial individual without whom this thesis could not have been completed is my co-supervisor, docent Dr.sc.ing. Oļegs Sļiskis, His provision of access to the electrical machines laboratory for conducting essential experiments, coupled with his valuable ideas and assistance, has played a pivotal role in the completion of this thesis that is now in the hands of the reader. I am thankful to all my fellow colleagues from Riga Technical University for engaging in fruitful discussions and the exchange of ideas. Their contributions played a vital role in shaping and refining this thesis to its completion. I extend my heartfelt gratitude to my family and friends for their continuous support and encouragement during the duration of my academic studies. I am grateful for the responsiveness shown by my colleagues from JSC Riga Electric Machinery Factory, the entire designing department, and I would especially like to highlight the contribution of my research colleague Marks Marinbahs to the development of my doctoral dissertation. Finally, I want to express my gratitude to all those individuals who have assisted me throughout the years, even if they are not specifically acknowledged in this list. Your contributions have not gone unnoticed, and you have my utmost respect and appreciation.

In the development of this PhD thesis, the capabilities of ChatGPT (GPT-4) by OpenAI were extensively utilized to elevate the quality of the written content. This advanced AI tool played a significant role in refining the language, improving the clarity of expression, and ensuring grammatical accuracy and stylistic consistency throughout the document. By leveraging the sophisticated linguistic and analytical abilities of ChatGPT, the thesis benefited from enhanced readability and professional presentation. This acknowledgment is made to ensure full transparency regarding the integration of advanced technological assistance in the thesis preparation process.

CONTENTS

LIST OF ABBREVIATIONS

MGU – Motor Gear Unit
IM – Induction Motor
RMS – Root Mean Square
FFT – Fast Fourier Transform
DWT – Discrete Wavelet Transform
EMD – Empirical Mode Decomposition
EEMD – Ensemble Empirical Mode Decomposition
CEEMD – Complete Ensemble Empirical Mode Decomposition
HHT – Hilbert-Huang Transform
IMF – Intrinsic Mode Functions
IGBT – Insulated-Gate Bipolar Transistor
DTC – Direct Torque Control
PWM – Pulse Width Modulation
UMP – Unbalanced Magnetic Pull
MMF – Magnetomotive Force
EMF – Electromotive Force
EMU – Electric Multiple Unit
FEM – Finite Element Method
CW – Clockwise
CCW – Counterclockwise

TOPICALITY OF THE WORK

The relevance of the task is determined by the constant increase in passenger traffic and the continuous daily operation time of modern electrified rolling stock on suburban and regional routes. The main actuator of an electric train is an electric traction drive, complex in structure and a combination of mechanical, electromechanical and electronic devices united by a control system of the lower and upper levels. The tendency to develop and implement electric trains with an asynchronous traction drive to increase productivity during traffic intensification remains unchanged. The electric traction drive is an independent and complex system since the processes occurring in it have different physical natures and different natures of interaction and influence on each other. For enterprises operating in the industry of railway transport and transport electromechanical equipment, the main issue remains the release of high-quality and reliable products; especially this concerns a complex of enterprises producing products in a complete set, in most cases, the consumer is interested – the manufacturer of electric trains. It is clear from practice that the most common combination of an electric drive kit is most often represented by an actuator – a traction motor gear unit and a control mechanism – a traction converter for electric trains operating in a 3 kV network. For a 25 kV network, a traction transformer from the same manufacturer may also be included in the electrical equipment kit.

The basis for the release of high-quality and reliable products is compliance with technological processes according to the developed and implemented design documentation, as well as final acceptance tests, the scope of which is regulated by the current standards for the acceptance and operation of rolling stock. The main disadvantage of existing methods for testing electric drives is their disunity and the possibility of checking their interaction only as part of an electric train if we are talking about serial production and not experimental production. In this case, identifying and eliminating the causes of a malfunction becomes extremely difficult due to the frequent inaccessibility of actuators and the impossibility of identifying the true source of the malfunction.

OBJECTIVE OF THE DOCTORAL THESIS

The Doctoral Thesis aims to study the readiness and technical condition of the actuator, namely the motor gear unit of the electric traction drive of a suburban and regional electric train at the stage of factory acceptance tests together with the supplied control system. It is an important task to implementat the proposed pre-operational tests of studies in the mode and under continuous production conditions, based on the creation of a methodology for an integrated approach to monitoring and analyzing the mechanical strength and vibration activity of traction equipment.

The following tasks were set and implemented within the framework of the Thesis research:

1. Develop a methodology for acceptance testing of traction geared motor together with an electric traction drive, taking into account the relationship of the traction and energy parameters of the geared motor unit with its vibration activity.

2. Determine the safety margin of the metal structure, taking into account the dynamic loads of the drive-in long-term loading modes and short-term maximum structural loads.

3. Detect defects by analyzing changes in diagnostic parameters and determine the correlations between them.

4. Test the methodology in industrial conditions based on a set of manufactured products, i.e., a set of electrical equipment submitted for testing and successfully tested in a 1 : 1 ratio before it is delivered to the customer.

As part of the Thesis research, an analysis was made of the results of studies on the problems of vibration states of transport and energy equipment, modern methods of mathematical modelling, and applied methods of diagnostics of electromechanical equipment.

SCIENTIFIC NOVELTY OF THE WORK

1. The Thesis presents a study aimed at establishing the relationship between the dynamic-vibrational state of an object and its energy parameters, using the example of traction motor-gear units of electric trains. The presented methodology is aimed at the timely determination of technological deviations of serial samples and design flaws of new products.

2. The eccentricity of the air gap of an asynchronous motor, primarily affecting slip and, ultimately, the power factor, causes a change in the characteristics of the stator current, forming magnetic shocks of imbalance, leading to the vibration of the motor gear unit.

3. A method for determining the safety margin for the most visible design elements has been presented, considering dynamic loads on the motor gear unit.

THEORETICAL AND PRACTICAL SIGNIFICANCE OF THE WORK

The method of monitoring the vibration condition of equipment is aimed at obtaining reliable results of acceptance tests and implementing the method of monitoring the technical condition of geared motor units operating as part of a train's electrical equipment complex under real operational loads.

The technique allows for the complete use of the information content of the electric motor energy indicators and the level of vibration disturbances of the geared motor unit during testing and, if necessary, significantly facilite the detection of faults.

The presented technique formed the basis of programs for acceptance of rotating units for the needs of rolling stock manufactured by JSC "Riga Electrical Machinery Factory".

RESEARCH METHODS, RELIABILITY AND VALIDITY OF RESULTS

The presented results of the Thesis research were obtained on the basis of the analysis of the functional features of asynchronous traction motors, the dynamics of traction drive loading and the conditions of their operation. The existing methods for solving the creation of a mechanical load on the shaft of the motor gear unit were carried out in laboratory and industrial conditions. A mechanical load control system was organized using the LabView software module. Based on a three-dimensional model of the motor gear unit with the help of a field solver, studies of the maximum stressed elements of the structure were carried out.

This Thesis research is presented in five chapters and chapter conclusions.

Chapter 1 provides an overview of current regulatory acts and documents and a list of regulatory standards related to the creation and control of the technical condition of products

for rail transport. An overview of existing methods of applied vibration diagnostics is also given.

Chapter 2 provides an analysis of the physical relationships between normal and emergency operation of electric traction drives. The problems of vibration phenomena in rail transport are described. A mathematical description of the operation of gear motor units as part of an electric train drive is given.

Chapter 3 describes the operation of the traction geared motor unit and the forces acting on it and created inside it. The modes of checking the safety margin of the structure for further analysis of the critical stress of the geared motor unit housing and bearing seats are presented.

In Chapter 4, based on calculations of static and dynamic loads, an analysis of the stress of the motor gear unit structure is presented, and calculations are made to determine the safety margin of the structure.

In Chapter 5, the methodology is tested and the relationship between the vibration state of the equipment being tested and its energy indicators is established.

CHAPTER 1. CURRENT STATE OF APPROACHES TO ASSESSING THE TECHNICAL CONDITION OF RAILWAY EQUIPMENT

With the continuous growth of passenger and freight traffic and in the conditions of increasing commercialization of transportation, the load on the transport infrastructure and the rolling stock inevitably increases. The requirements for the quality and service life of the equipment supplied for the needs of the rolling stock also increase, especially in cases where trains on electric traction with a voltage of 3 kVDC and 25 kVAC, as well as trains on locomotive traction, are operated on one section. In recent years, the number of specialized conferences, councils and exhibitions has increased sharply, such as InnoTrans, Trako, RailAsia, etc., which set themselves the task of not only demonstrating technical achievements in the field of transport, but also bringing the presented samples to the required level of safe and reliable operation. Only during the last exhibition InnoTrans2024, about 1/6 of the companies represented were certification and technical supervision bodies of railways and rolling stock.

As was noted during the IMECO conference, there might be a possible increase in technical use, the so-called safety factor by more than 12 %, due to the introduction of diagnostic tools and preliminary equipment control before transferring it to serial operation. In turn, the time for downtime and repair of rolling stock due to preventive control and diagnostic measures can be reduced to 40 %. In turn, the quality and completeness of diagnostic measures, as well as the set of interrelations of controlled parameters determine the reliability of diagnostic signs and accompanying phenomena.

The author of the Thesis, based on the methods of vibration diagnostics of motor gear units (hereinafter – MGU) of railway transport (see Fig. 1.1), set the task of identifying the most informative combinations of signs of major faults reflected in the frequency and time domains. In this case, the traction and energy indicators of the MGU are presented in the frequency domain of the hormonal spectrum, and the root-mean-square value of vibration is presented in the time domain [1].

Diagnostics of defects of rotating equipment by vibration signal spectra of rotating equipment is usually considered by practical diagnosticians to be the main and most effective due to several important reasons.

Firstly, the distinctive features of most defects of rotating equipment are easily differentiated in the vibration signal spectra.

Secondly, for more than half of the diagnosed defects, the set of characteristic harmonics in the spectrum is unique. For the remaining defects, the sets of characteristic harmonics can overlap each other in composition and harmonic ratio, however, if the diagnostician has sufficient practical experience, these defects can be confidently separated.

Thirdly, devices for recording and analyzing vibration signals that have a built-in spectral transformation function are the most common in practice; this is an almost mandatory function of the device. For example, it is currently quite difficult to find a vibration device equipped with a modal signal analysis function or having a built–in wavelet transformation function. Fourthly, diagnostics of defects based on vibration defect spectra can be most easily created in the form of an expert diagnostic system implemented in a personal computer, and even in the device itself, if we are talking about the most advanced versions of such diagnostic equipment.

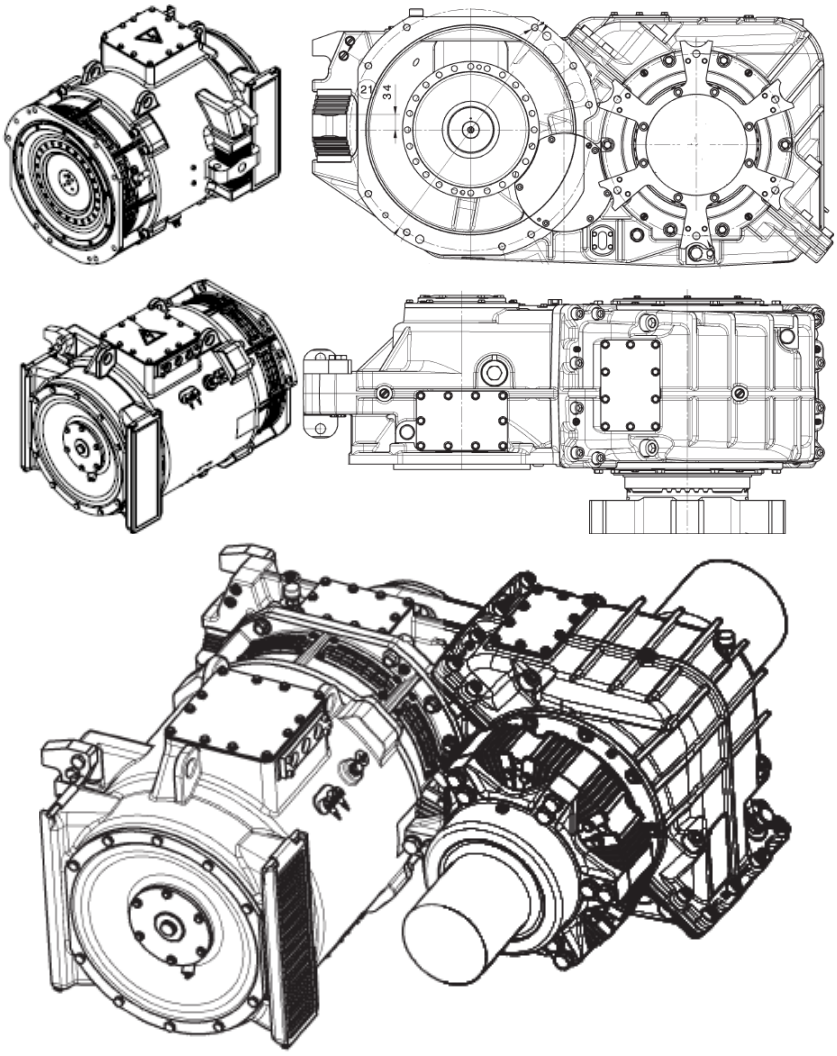

Fig. 1.1. Structure of traction MGU.

Due to the use of both single-support and two-support structures of traction motors as actuators of the traction electric drive, the requirements for the quality of rotor balancing increase, and exceeding the level of residual rotor imbalance is therefore becoming the most common defect of rotating traction machines. Taking into account both the design and technological features of manufacturing rotors of asynchronous motors and synchronous motors with fixed magnets, as well as synchro-reactive, or relaxant motors, namely the error in cutting and blending of rotor iron sheets, pressing of copper rods and the quality of their soldering (for asynchronous motors), it is possible to conditionally systematize the causes of imbalances:

- manufacturing defects in the manufacture of stamped parts and parts manufactured by laser or hydroabrasive cutting;
- due to the accumulated error in the assembly of poor-quality parts - as a result, a defective assembly unit, in particular a blended and pressed rotor, in which the accumulated

error and displacement of the sheets form a "comb" and problematic installation of copper rods of the "squirrel cage";

- insufficiently high-quality processing of support parts, i.e. shields and flanges, in particular the bearing mounting holes, as a result of uneven wear of the bearings themselves;
- the resulting distorted operation of the assembled product, represented by the traction motor - uneven air gap, local overheating and, as a result, distortion of the magnetic flux, slip and deterioration of the traction-energy parameters - the power factor of the motor and its efficiency.

The most seminal research in the domain of torsional vibrations is expounded in the work entitled Electric Motors and Drives in Torsional Vibration Analysis and Design, authored by Timo P. Holopainen, Jauko Niiranen, Pieder Jörg, and Davide Andreo, who represent various divisions of ABB in Switzerland and Finland [1]. The work presented by the authors sets the goal of determining the causes and occurrence and development of further influence of torsional vibrations in a closed system of traction electric drive. The Thesis presents in detail the understanding of torsional vibrations and their influence on dynamic processes, in particular those occurring in the air gap of the motor. The undoubted advantage of the Thesis is not only laboratory research but also experiments in real operation mode. Due to the fact that the study covers various types of traction motors, the author presented for analysis various electric traction control systems, namely voltage and frequency converters, current converters and switching loads. The study also determines the role of feedback and its noise immunity, as a possible accompanying link in increasing torsional vibrations [1].

1.1. Common Terminology Used for Machinery Vibration

The **velocity** of vibration is measured in peak units such as millimetres per second (mm/s). Another way of looking at velocity is distance per time or how much is the machine moving every second in three important directions at all main bearing points (AXIAL, VERTICAL, HORIZONTAL). Velocity measurements and monitoring of vibration are the most common units to identify various problems or acceptability such as unbalance, misalignment, looseness (machinery structural, foundations, or bearings), harmonics, and many other issues in the machinery frequency range and many multiples of actual speed [1].

Velocity measurements (if using a single axis sensor/probe and hand–held meter) are recorded in three directions: axial, horizontal and vertical at all main bearing blocks or motor frame end bells. The convenient thing about vibration velocity is that it is not related to speed. Advanced computers with triaxial sensors can measure in all three planes from one location.

Overall or Broadband Vibration Severity using Velocity is applicable to all types of general rotating equipment (*ISO/ANSI*) operating at full load or speed condition. The relationship of the above vibration velocity levels is found on the Vibration Severity Graph as shown on Fig. 1.2.

Acceleration is very important for the detection of faults with bearings, gear mesh or electrical issues. Acceleration is measured in acceleration units of G. Simplified – millimetres per second/second (mm/s/s). Acceleration is very important bearing and gear fault data in the high frequency ranges. Acceleration is also a sudden change in velocity. Acceleration data are relevant in the rotational axis only.

Displacement is measured in peak-to-peak units of millimetres (mm). Displacement measurements are recorded in the same three directions as velocity – axial, horizontal and

vertical. Displacement is not used or recommended for recording or monitoring because severity or acceptability is speed dependent. Displacement is also used to identify problems in the lower frequency ranges. Displacement can be used for measuring reference values = walls, floors, beams, pads, frames = very slow moving or stationary objects.

Frequency – knowing the frequency of vibration peaks helps to pinpoint the potential sources. Frequency is used in advanced vibration analysis to identify all types of bearing fault frequencies, real time spectrums, and motor current signature analysis, etc.

Phase is the angle of vibration issue. Phase is used to dynamic balance and identifies resonance (critical speed) problems. Phase is not used in everyday vibration measurements or monitoring. Phase of vibration is recorded using a stroboscope or infrared tachometer in conjunction with a vibration analyzer instrument. New technology and software is being used to add phase analysis to the final evaluation and diagnostics [2].

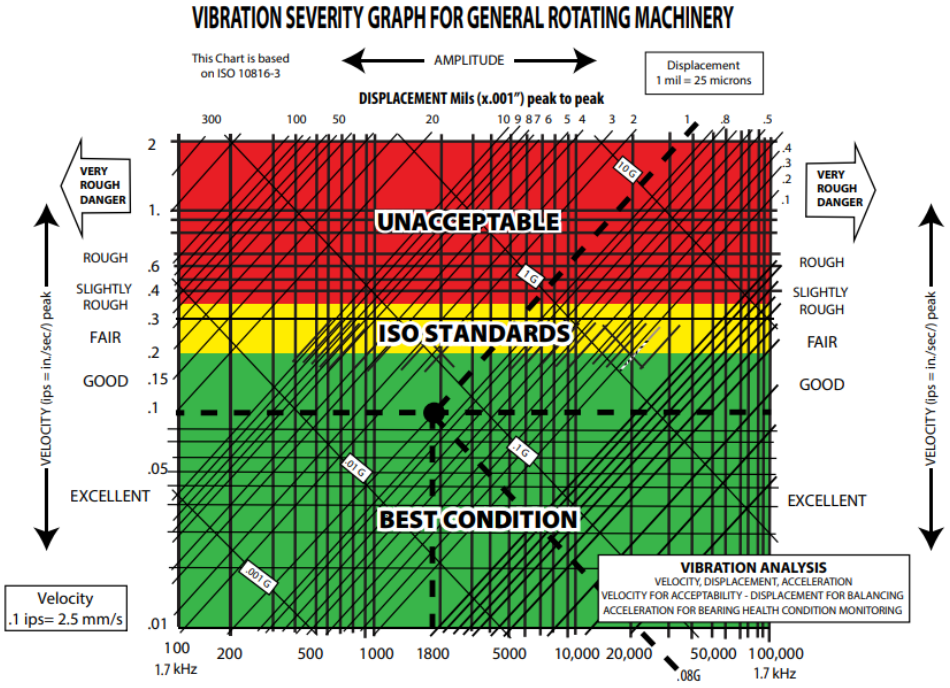

Fig. 1.2. Vibration severity graph for rotating machinery.

1.2. Mechanisms Behind Rail – Induced Vibrations

During the movement, the train creates a combined dynamic system, causing vibration excitations, primarily in the track circuit. Despite the vibration damping systems provided in the designs of the electric train bogies, such as shock absorbers, springs and cushions, the moving train remains a powerful source of vibration excitations. In turn, the smooth passage of the wheel pair along the rails is affected by their wear, laying and the condition of the embankment, which together also have some shock-absorbing properties capable of suppressing vertical vibrations [2].

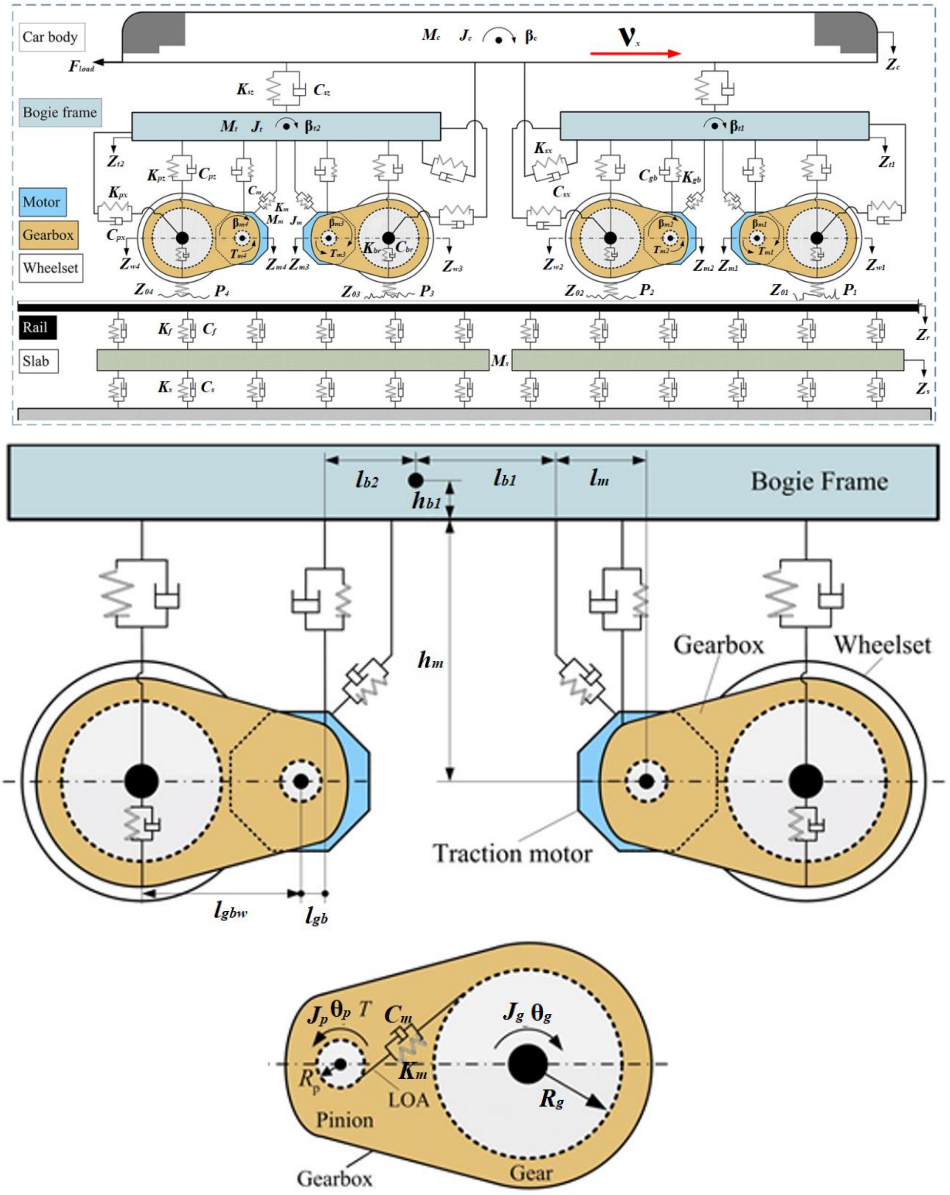

Fig. 1.3. Vehicle–track coupled dynamics model of vehicle with traction motors and gear transmissions [2].

where:

$K_{pz}, C_{pz}, K_{px}, C_{px}$ – primary suspension refers to the steel spring and the shock absorber between the bogie frame and the axle box;

$K_{sz}, C_{sz}, K_{sx}, C_{sx}$ – secondary suspension denotes the air spring between the bogie frame and the car body;

T_{mi} – gear transmission systems in gearboxes transmit the traction torques from traction motors to wheelsets, generating longitudinal creep force at the wheel-rail contact interface.

Due to its design and the method of fastening and support, the sleeper-rail system also has a certain degree of freedom of interaction, and in combination with the influence of the ballast layer of the track embankment, resonant vibrations are also possible, the range of which must be "isolated" from the permissible operating vibration frequencies of the rolling stock [3]. It is extremely difficult to provide for the interaction of dynamic oscillatory systems of an electric train and a railway track also due to the different nature of the occurrence of these vibrations. In addition to the provided structural irregularities of the track, there is a natural change in the rigidity of the railway track, soil crumbling, etc (see on Fig. 1.3). With increasing wheel wear and weakening of the car suspension, the oscillatory influence from the train increases, the vibration activity increases. In the range of resonant frequencies, when the natural vibrations of the rail system and the electric train bogie coincide, vibration damping by means of the provided shock absorption is less effective, and the attenuation of the vibration occurs much more slowly. A detailed model of the interaction of oscillatory systems is presented in [4].

In general, the vibration source is a complex system, which makes it difficult to accurately predict the occurrence of vibrations, primarily due to the difficulty of identifying the original sources.

- Quasi-static excitation, i.e. the deflection of the track and support system moving together with the movement of the train. If a point on the track is fixed, then the variable loads acting on it cause the appearance of bending waves both in the rails themselves and in the adjacent soil.
- Dynamic excitation can manifest itself from four sources:
  - parametric excitation (as shown in Table 1.1) is the excitation of oscillations occurring in an oscillatory system as a result of periodic changes in the value of any of the "oscillatory parameters" of the system (i.e. parameters on the value of which the values of potential and kinetic energies and the periods of natural oscillations of the system essentially depend);
  - rail corrugation, which occurs from repeated wear on the rail head surface;
  - track discontinuities at the wheel–rail interface;
  - irregularities on the wheel surface, commonly referred to as wheel out-of-roundness (affecting low frequencies) or wheel roughness (affecting high frequencies). Wheel roughness results in broadband vibration, while polygonal wear results in periodic vibration [5].

The vibration frequencies generated by the described mechanisms are influenced by the train's speed. Table 1.1 illustrates the frequency range for each vibration source at train speeds of 40 km/h, 80 km/h, and 160 km/h. For rail, higher velocities are possible, though they are not included in this table.

For vibrations transmitted through the ground, the suitable frequency spectrum is specified in *ISO 14837* – Mechanical vibration – ground–borne noise and vibration aris caused from rail systems, as spanning from 1 and 80 Hz. The table shows which mechanisms are most pertinent (by color coding). Fig. 1.4 below illustrates the frequency ranges of concern for ground–borne vibrations, ground–borne noise, and general audible noise.

Table 1.1

Approximate Frequencies of Standard Vibrations for Each of the Producing Mechanisms, Based on Train Speed (for illustrative purposes only)

Vehicle speed	40 km/h	80 km/h	160 km/h
Moving load (axle gap around 1.8 m)	3 Hz	5 Hz	11 Hz
Track irregularities	4 Hz 100 Hz	2 Hz 200 Hz	4 Hz 400 Hz
Rail surface wear	~ 500 Hz	~ 1000 Hz	~ 2000 Hz
Wheel surface irregularities	4 Hz	8 Hz	15 Hz
Wheel polygonal wear (with a wavelength of 0.1 m)	~ 100 Hz	~ 200 Hz	~ 400 Hz
Bogie gap (around 8 m)	~ 1 Hz	~ 3 Hz	~ 5 Hz
Sleeper gap (0.6 m)	Multitudes of 16 Hz	Multitudes of 32 Hz	Multitudes of 64 Hz

The figure illustrates that there is a frequency spectrum, approximately between 15 and 80 Hz, where all three effects overlap. Within this range, it can be challenging to differentiate between them, as the presence of one may influence the perception of another. This can result in either a hiding effect (for instance, vibrations becoming noticeable only after the installation of a noise barrier) or an additive effect (vibrations feeling more intense when combined with audible or low-frequency sound) [5].

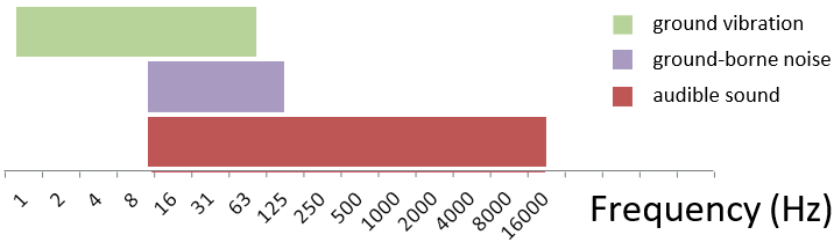

Fig. 1.4. Frequency spectrum for perceivable sound, tangible ground vibrations, and noise transmitted through the ground.

1.3. Standards and Regulations

It is important to highlight that there are multiple regulations for vibration monitoring. The majority of systems and equipment control frameworks rely on the following standards:

1) *ISO 13373–1–2002* – Vibration condition monitoring of machines. This guideline outlines the fundamental principles of vibration monitoring, the kinds of sensors used, and their mounting locations [6].

2) *ISO 15242–1–2015* – Vibration measurement methods. This regulation defines the vibration rating of rolling bearings and sets the criteria for environmental conditions during measurement (limited to a test bench) [7]. This standard also details how to measure vibration parameters across one or more frequency ranges between 20 and 10 000 Hz. Specific frequency spectrum is designated for different bearing types. When assessing the vibration of ball deep groove and angular contact bearings within a certain dimension's category for low, medium, and high–frequency ranges, the following limits are defined: from 50 to 300 Hz, from 300 to 1800 Hz, and from 1800 to 10 000 Hz.

3) *ISO 2041:2009* – Vibration Terms and definitions. This international standard defines the fundamental terms and concepts used in the field of vibration [8].

4) *ISO 20816–3:2022* – Mechanical vibration – Measurement and evaluation of machine vibration. Part 3: Industrial machinery with a power rating above 15 kW and operating speeds between 120 r/min and 30 000 r/min. This standard specifies criteria for assessing machine vibration at their operational locations by measuring vibrations on the casings or bearing housings [9].

5) *ISO 17359:2018* – Condition monitoring and diagnostics of machines – General guidelines. Vibration generated by rotodynamic pump and compressor units. Applicable to units with power exceeding 2 kW, this standard provides guidelines for evaluating their vibration status during operation and acceptance tests post-installation and repair. It also defines vibration thresholds that characterize the condition of drive components [10].

Due to the fact that approaches to equipment operation are changing, the equipment itself is changing and becoming more complex, and industrial and environmental safety requirements are becoming more stringent. A large number of units, the hidden nature of the origin and development of faults, and accumulated equipment fatigue are often the causes of emergency situations that are accompanied by significant economic and natural losses. The trends of recent years force us to rethink the requirements for the reliability of assessing the current state of railway transport, its equipment, and determining its remaining life, considering the latest achievements of science and technology in the field of technical diagnostics. Over the years of using vibration diagnostics tools, as practical experience was accumulated and statistical material was developed, the regulatory framework was subject to a number of revisions (VDI 2056, *ISO 2372*, etc.). A classification of rotary equipment (*ISO 3945*) was introduced, threshold values for assessing the level of vibration activity of units of various groups and requirements for the measuring tools used were revised [11].

Several standards also offer main guidelines for data interpretation and machine diagnostics:

1) *ISO 13379–1:2012* – Condition monitoring and diagnostics of machines – Data interpretation and diagnostics techniques. Part 1: General guidelines. This standard outlines the objectives of machine diagnostics and helps establish methodologies for diagnosing machinery [12].

2) *ISO 13379–2:2015* – Condition monitoring and diagnostics of machines – Data interpretation and diagnostics techniques. Part 2. Data driven approach. This standard provides guidance on using data–driven methods for monitoring and diagnosing component condition [13].

The aforementioned normative documents demonstrate the advanced development of vibration diagnostic methods. Modern hardware and software technologies enable high–quality data acquisition and analysis.

1.4. Analytical Review of Motor Monitoring and Diagnostic Methods

1.4.1. Common Faults in Induction Motors

1.4.1.1. Fault Classification

Induction motors (IMs) are susceptible to different kinds of faults. The classification of common faults is illustrated in Fig. 1.5. IMs faults can be divided into mechanical and electrical sections. Based on the research [14], the most frequent mechanical issues include air gap eccentricity and bearing failures. Electrical faults are split into stator and rotor categories. The

main stator faults include winding breaks and short circuits, while major rotor faults include defects in the rotor bars and rings [15].

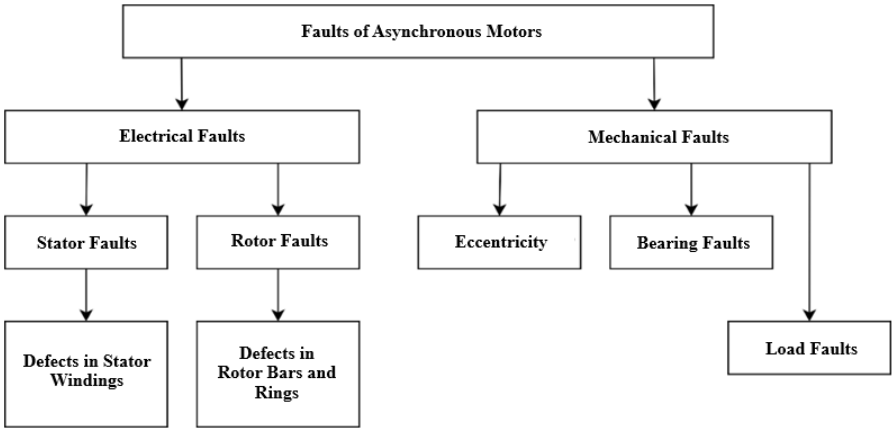

Fig. 1.5. Classification of common faults in induction motors.

Data from the Institute of Electrical and Electronics Engineers (IEEE) and the Electric Power Research Institute (EPRI) show that over 40 % of all IM failures are due to bearing issues, as depicted in Fig. 1.6.

These failures are critical as they increase both vibration and noise levels in IMs [16]. The main reasons for bearing defects include material fatigue, heightened air gap eccentricity, unbalanced loads, shaft misalignment, nearby equipment vibrations, and torque fluctuations.

The main stator faults include open winding circuits and short circuits. An open circuit in the stator winding leads to an increase in the reverse sequence current amplitude, which can be detected by comparing the direct and reverse sequence current amplitudes, and when these values approach each other, the protection system is triggered. Short circuits in stator windings are among the most challenging faults to detect, often caused by increased core temperature, contamination with oil, moisture, or dust, electrical discharges, or coolant system leaks [17].

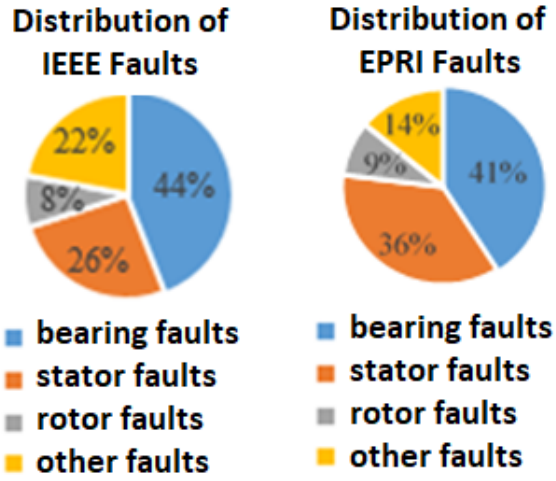

Fig 1.6. Fault distribution according to IEEE and EPRI.

1.4.1.2. Rotor Eccentricity

In engineering documentation, rotor eccentricity is characterized as a condition where the air gap between the rotor and stator becomes grungy. This irregularity, known as eccentricity, leads to accelerated bearing wear and can cause additional malfunctions. Researches suggest that eccentricity accounts for over 80 % of IMs breakdowns, making it one of the most critical defects to detect.

Eccentricity is typically divided into static, dynamic, and combined forms, often resulting from improper motor assembly, shaft misalignment, wear or malfunction of bearings, load imbalances, or issues with the gearbox.

Rotor eccentricity results in uneven load distribution of stress on the bearings, causing faster degradation. Moreover, the radial magnetic force generated due to eccentricity impact the stator core, subjecting the stator windings to unnecessary and potentially harmful vibrations [18].

1.4.1.3. Rotor Faults

The fracturing or cracking of rotor bars and rings contributes to 5–10 % of all IM breakdowns. The primary reasons for these defects include thermal stress in the rotor bars, magnetic imbalances caused by asymmetric electromagnetic forces, electromagnetic noise and vibrations, exposure to chemicals and moisture causing corrosion, and material fatigue that results in uneven mechanical loads.

Numerous research papers concentrate on detecting faults specifically in rotor bars, emphasizing the importance of diagnosing this defect.

Failure to identify and correct these defects promptly can lead to serious consequences [19]:

- Fractured bars can generate sparks, creating a severe risk in explosive environments;
- The increased current through the remaining intact bars can overheat the rotor core due to elevated temperatures near the broken bars;
- Broken bars can cause variations in rotor torque and speed, which may accelerate bearing wear and induce failures in other components;
- Large gaps in the rotor windings may lead to uneven expansion, resulting in rotor bending and imbalance, which in turn causes excessive vibration;
- During high-speed rotation, fragments of broken bars may be propelled from their positions due to centrifugal forces, potentially damaging the stator windings and leading to total motor failure;
- Asymmetric electromagnetic fields, caused by rotor damage, can increase eccentricity, both static and dynamic, leading to contact between rotor and stator windings, which may severely damage the rotor core and possibly cause an emergency shutdown.

1.4.2. Techniques for Monitoring and Diagnosing Induction Motors

Techniques used to monitor and diagnose the technical condition of IMs are classified by the parameters measured:

- Stator current;
- Vibrations in stationary components;
- Acoustic vibrations and emission;
- Torque;
- Electrical and magnetic fluxes;
- Temperature.

Diagnostic methods that utilize current analysis and vibration monitoring are the most commonly employed due to their convenience and practicality of measurement. These techniques enable for the early detection of critical IM faults, making them highly suitable for inclusion in IM condition monitoring systems. These methods, along with the associated signal processing techniques for current and vibration analysis, are covered in Section 1.5.

Methods based on measuring acoustic vibrations are similar to those that analyze mechanical vibrations since acoustic vibrations originate from the machine's mechanical parts. However, for some scenarios, acoustic methods are more advantageous because they do not require physical contact with the IM. Acoustic signal analysis is mainly used to detect mechanical defects [20]. A major limitation of these methods is the high level of signals noise due to interference from surrounding hardware.

Torque measurement techniques are used to identify problems caused by fluctuations in torque. The torque within the air gap reflects the combined impact of all the flux linkages and currents in both the stator and rotor, therefore, most potential IM defects affect the torque. The main drawback of these methods is the high expense of torque sensors [21]. In some researches, it was noted, that these methods are less accurate when the IM is operating under dynamic conditions. Electromagnetic diagnostic methods are based on measuring electrical and magnetic fluxes either inside or near the IM [14], [20]. These methods are mostly used to detect rotor eccentricity by identifying irregularities in the electromagnetic fields. These methods are recognized for their precision in detecting asymmetries and, by extension, diagnosing faults.

These approaches are extensively applied in diagnosing high-voltage machines. However, a key disadvantage is the difficulty of installing the sensors, often requiring partial disassembly of the motor or integration of the sensors during the manufacturing process. Moreover, these techniques are inherently invasive, necessitating direct access to the equipment being diagnosed, which can be particularly problematic in some cases [22].

Thermal diagnostic methods rely on measuring the temperature of one or more components within IM. To evaluate the motor's thermal characteristics, both contact and non-contact temperature sensors, as well as thermal imaging cameras, are used. Contact sensors, like thermocouples and thermistors, offer advantages like low cost and high measurement accuracy, but they require direct access to the motor [23]. Non-contact temperature sensors are generally costlier and are sensitive to environmental factors like humidity, dust, and ambient air temperature. Thermal imaging cameras provide a more comprehensive assessment of the motor's thermal condition and are typically used for periodic inspections rather than continuous monitoring of IMs. The disadvantages of thermal imaging equipment include their high cost and limitations related to lower temperature sensitivity limits.

However, the limitations of thermal diagnostic methods include the fact that faults are often detected only after they have significantly progressed, as well as a high dependency on environmental conditions. Specifically, the use of these methods becomes challenging in environments with high ambient temperatures [24].

1.5. Vibration Diagnostics Techniques for Induction Motors

1.5.1. Overview of Vibration Diagnostics Techniques

Vibration diagnostics have become extensively utilized for assessing and monitoring the technical condition of IM, with commercial applications. Leading companies offering vibration

diagnostic solutions include Bruel & Kjaer (Denmark), Metravib Instruments (France), PCB Piezotronics (USA), ABB (Sweden, Switzerland), VAST LLC (Russia), INCOTES LLC (Russia), Vibro–Center LLC (Russia), and Dimrus LLC (Russia).

The main benefits of vibration diagnostics include high precision in detecting issues and the ability to localize specific defects. However, drawbacks include the necessity for direct access to the IM and the high sensitivity of vibration signals to interference from nearby equipment. Vibration diagnostics can reveal a variety of IM issues, including bearing failures, loosened mounting structures, electromagnetic system defects (e.g., broken rotor bars), air gap eccentricity, and other faults [25].

1.5.2. Monitoring Overall Vibration Levels and Peak Factor

Several methods are used in vibration diagnostics. The simplest ones are based on tracking overall vibration levels and calculating the peak factor. Monitoring overall vibration levels entails measuring the RMS values of vibration acceleration and velocity and observing their trends over time. The peak factor method calculates the ratio of the maximum amplitude during a given time frame to the RMS value of the signal. Surpassing a predefined peak factor threshold indicates the presence of impact impulses. A high frequency of such impulses may suggest a potential bearing issues, making continued operation of the machine potentially unsafe. These techniques provide only a general indication of the motor's health, and emerging defects might go unnoticed, as they cause minimal change in the monitored parameters [26], meaning that problems are typically detected when they are already considerably developed.

1.5.3. Fourier Spectrum Analysis of Vibration Signals

The most precise diagnostic methods are based on spectral analysis, although these are more complicated to apply. These techniques are seen as more promising, especially as advances in microcontroller technology allow them to be integrated into monitoring systems. The FFT is one of the most widely used algorithms for converting signals into the frequency domain [27]. The key advantage of FFT is its low computational cost, with a complexity of $O(n \log n)$. However, FFT has its limitations:

- It requires long signal sampling durations to achieve high–frequency resolution, such as 100 seconds of data to reach a resolution of 0.01 Hz.
- The existence of two dominant harmonics tied to the motor’s power supply frequency and rotor speed, which are 5–10 times stronger than fault indicators.
- The positions of fault signatures depend on the motor slip.

1.5.4. Envelope Analysis Method

The envelope analysis technique is widely used in vibration diagnostics. This approach involves examining low-frequency modulations of high–frequency components in the time–domain signal, which can reveal faults [26]. The presence of harmonics in the envelope spectrum points to defects, while their amplitude indicates the severity. The envelope is usually extracted using amplitude/phase detectors or the Hilbert transform. The envelope spectrum is typically obtained through FFT, which means this method inherits both the strengths and limitations of FFT. However, some researchers have moved towards using the DWT for envelope spectrum analysis, which offers lower computational demands and higher accuracy in detecting fault signatures. Envelope analysis is particularly useful for diagnosing bearing and rotor defects.

Advantages of this method include: high sensitivity, early fault detection, the ability to localize faults, and the absence of dominant harmonics from power supply or rotor frequencies. The disadvantages include the need for extended signal sampling durations, dependence on IM slip, and spectral leakage [28], [29].

1.5.5. Empirical Decomposition Methods

Empirical Mode Decomposition (EMD) and its variants, such as Ensemble Empirical Mode Decomposition (EEMD) and Complete Ensemble Empirical Mode Decomposition (CEEMD), are also widely applied in vibration diagnostics of induction motors. These methods are based on the Hilbert-Huang Transform (HHT), where the signal is decomposed into intrinsic mode functions (IMFs), separating harmonics associated with faults [30], [31]. HHT offers time–frequency analysis without needing a pre-defined functional basis, as the IMFs are derived adaptively from the signal. This method can detect rotor eccentricity, broken rotor bars, and bearing defects. As indicated by the study [32] the required signal sampling length is 10 seconds. The strengths of EMD include high noise resistance, no need for predefined basis functions, and low computational complexity – $O(n \log n)$. However, it lacks a definitive criterion for determining the total number of IMFs, and fault localization requires knowledge of motor speed or slip values.

1.5.6. Wavelet Transform-based Methods

Wavelet analysis is another popular method in vibration diagnostics [26]. A key feature is that the frequency resolution does not depend on the sample length, making it suitable for implementation in embedded systems. The method involves decomposing the signal into multiple wavelet bases, which allows noise removal and identification of relevant frequency regions where faults are present. Wavelet analysis has proven effective in diagnosing major motor issues, including bearing faults by processing vibration signals [33]. A method for monitoring critical operating modes of high-energy installations based on wavelet analysis of vibration signals was developed. The advantage of wavelet analysis is its low computational cost $O(n)$ and shorter sample length requirement compared to FFT, as shown in [26], where a 1–second sample was sufficient. The main disadvantages include the lack of a standardized criterion for wavelet selection, difficulty in estimating computational errors, which are compounded by other random factors during data processing, and challenges in interpreting the results.

1.5.7. Vibration Manifestations in Transport Systems

The issue of studying vibration manifestations in transport systems and traction drives is the subject of an impressive number of scientific works and implementations, some of which are presented in thematic ranking in Fig. 1.7.

Fig. 1.7. Overview of torsional vibration research.

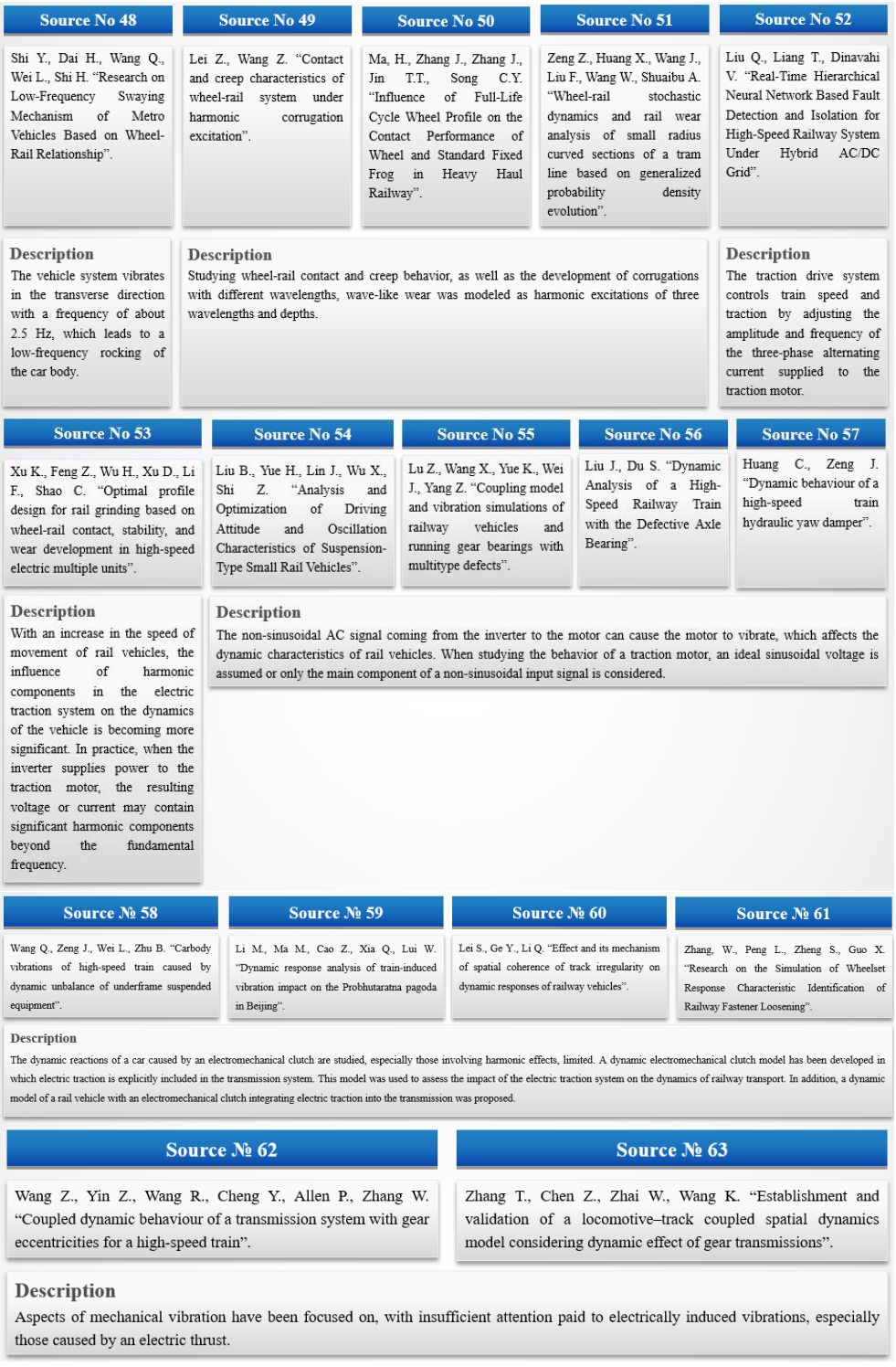

Fig. 1.7. Overview of torsional vibration research.

1.6. First Chapter Conclusions

1. The analysis of various maintenance strategies suggests that continuous monitoring of the technical condition is optimal from both economic and energy perspectives.

2. The most promising approaches are those based on current and vibration measurements since the main types of faults affect these parameters. These indicators are also convenient for monitoring; in particular, current diagnostics can be easily integrated into existing motor protection systems since it already involves measuring the current in the stator windings. The main disadvantages of current methods include:

- requirement for long-term signal sampling;
- high computational complexity;
- need for prior knowledge of motor slip.

CHAPTER 2. EFFECT OF TRACTION TRANSMISSION ON THE DYNAMICS OF ELECTRIC TRAINS

2.1. Impact of Electrical Component of Traction Transmission on Dynamic Characteristics of Railway Vehicles

The power supply system of the train can be represented by various configurations of power and actuator mechanisms, the role of which is performed by traction MGU in the train. For MGU with asynchronous traction motors, the power source is a traction converter – a source of alternating non-sinusoidal current [34]. Further, MGUs located on motor bogies can be connected individually or in pairs to the power outputs of the traction converter. The train layout can include purely motor cars, but another option is also possible with the installation of a motor bogie on each car. Recently, preference has been given to the second option. Usually, the power part of the converter includes an adjustable DC link, a block of traction inverters, the function of which is to regulate the voltage and frequency level, and directly the inverter control system, often implemented on IGBT transistor modules [35], [36]. In addition, the converter is equipped with a processing unit for feedback signals, motors, braking systems, etc., which makes it possible to regulate the torque and speed of the motor rotor.

2.1.1. General Approach to Development of Mathematical Model of Traction Transmission. Analytical Representation of Transmission System

To include the traction motor model in the general mathematical model of the electric train power drive, it is recommended in [64] to resort to the following assumptions:

- to assume that the three-phase supply windings of the motor are symmetrical, and in view of the limited number of stator slots, to neglect the harmonic magnetomotive forces;
- to ignore the presence and magnitude of magnetic saturation and losses in the motor core;
- the self-induction and mutual inductance of each winding are considered linear;
- the possible influence of temperature on the motor resistance is not taken into account.

In the 2-phase coordinate system dq, which is in arbitrary rotation, the mathematical model of the motor is described by the following expressions:

Torque Equation [65]:

$$T_e = \frac{3}{2} n_p \times \frac{L_m}{\sigma L_s L_r} \times |\psi_s| \times |\psi_r| \times sin\,\theta. \quad (2.1)$$

Motion equation:

$$T_e = T_L + \frac{J}{n_p} \times \frac{d_{\omega r}}{dt}, \quad (2.2)$$

where: ψ_s – stator flux linkage;

ψ_r – rotor flux linkage;

L_s – stator intrinsic inductance;

L_r – rotor intrinsic inductance;

L_m – reciprocal inductance of two-phase winding;

n_p – polar logarithm;

J – moment of inertia;

r – angular velocity;

σ – leakage inductance;

θ – the angle between the stator and the rotor flux linkages.

When the motor is supplied to the non–sinusoidal power source, the time harmonic magneto–motive force in the air gap will result in extra harmonic torques. The harmonic torque of traction motor consists of both constant harmonic torque and oscillating harmonic torque. If the air gap harmonic flux and rotor harmonic currents are of the equivalent order, their interaction generates constant harmonic torque. If the main and harmonic waves in the air gap create n rotating magnetic fields, $(n-1)$ consistent harmonic torques will be produced. The $k-th$ constant harmonic torque can be expressed as [64]:

$$T_k = \pm\frac{mn_p}{2\pi f_1} \times I_{2k}^2 \times \frac{R_{rk}}{(k\pm1)}. \tag{2.3}$$

If the harmonic flux and rotor current are of different orders, their interaction results in vibrating harmonic torque. When main and harmonic waves produce n rotating magnetic fields in the air gap, (n^2-n) vibrating harmonic torques arise. For 5th and 7th harmonics value of vabration torque can be calculated as:

$$T_{5-1} = \frac{3n_p}{2\pi f_1} \times I_{25} \times E_2\, cos(6\omega t - \varphi_2) = \frac{3n_p}{2\pi f_1} \times I_{25} \times \\ \times E_2\, cos(6\omega t + \pi - \varphi_2). \tag{2.4}$$

$$T_{7-1} = \frac{3n_p}{2\pi f_1} \times I_{27} \times E_2\, cos(6\omega t - \varphi_2). \tag{2.5}$$

The interaction between the 11th and 13th harmonics and the main magnetic field creates the 12th harmonic torque. In the simplified gear transmission system [65], pure torsional vibration is considered, as depicted in Fig. 2.1. Here, k_i and k_0 represent the torsional stiffness of the drive and driven shafts, respectively; c_i and c_0 represent their torsional damping coefficients; α_i and α_0 are the angular displacements, and n_i and n_0 are their angular velocities. The driving torque is denoted as T_i and T_0, where the gear ratio is specified as:

$$N = \frac{n_i}{n_0}. \tag{2.6}$$

The dynamic equation for gear transmission torque is [65]:

$$T = k \times (\alpha_0 - \frac{\alpha_i}{N}). \tag{2.7}$$

It can be assumed that for the right and left wheels of the motor sled the value of rotational inertia will have an equal value, then the system of equations of torsional vibrations will take the form:

$$\begin{bmatrix} J_1 & 0 \\ 0 & J_2 \end{bmatrix}\begin{bmatrix} \ddot{\theta}_1 \\ \ddot{\theta}_2 \end{bmatrix} + \begin{bmatrix} c & -c_2 \\ -c_1 & 2c_2 \end{bmatrix}\begin{bmatrix} \dot{\theta}_1 \\ \dot{\theta}_2 \end{bmatrix} + \begin{bmatrix} k & -k_2 \\ -k_1 & 2k_2 \end{bmatrix}\begin{bmatrix} \ddot{\theta}_1 \\ \ddot{\theta}_2 \end{bmatrix} = \begin{bmatrix} -\frac{J_1}{J}T_e - T_1 \\ T_1 - T_2 \end{bmatrix}, \tag{2.8}$$

The torque control system in the traction drive can be implemented indirectly, by recalculating the values of currents and voltages, and can also be implemented in the form of direct torque control, DTC, when the control system implements the function of tracking and comparing the values of the flow and torque. In turn, the torque value corresponds to the system of equations [66]:

$$\begin{cases} \psi_{s\alpha} = \int (u_{s\alpha} - i_{s\alpha}R_s)dt \\ \psi_{s\beta} = \int (u_{s\beta} - i_{s\beta}R_s)dt \end{cases}. \tag{2.9}$$

The observed electromagnetic torque values are:

$$T_e = n_p \cdot (\hat{\psi}_{s\alpha} i_{s\beta} - \hat{\psi}_{s\beta} i_{s\alpha}). \tag{2.10}$$

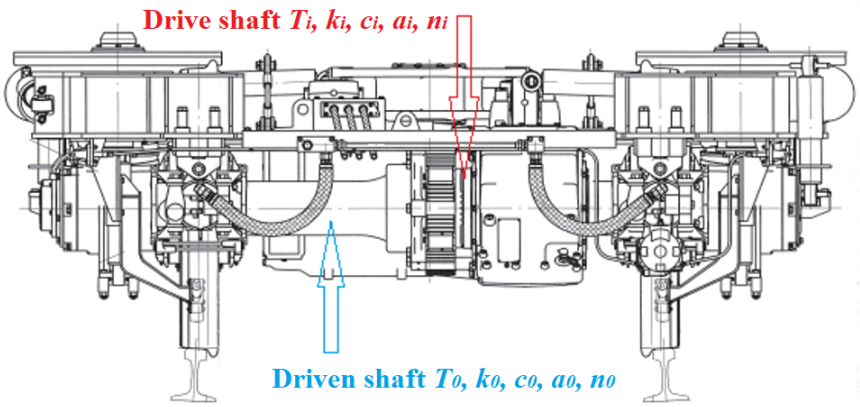

J – equivalent rotational inertia of the entire transmission system as referred to the wheel axle; J_1 – inertia of the left wheel; J_2 – inertia of the right wheel; k_1 – the equivalent torsion stiffness between the transmission system and the wheel–set; k_2 – torsion stiffness of wheel–set; c_1 – equivalent torsion damping between the transmission system and the wheel–set; c_2 – torsion damping of wheel–set; T_e – electromagnetic torque generated by the traction motor; T_1 – opposing torque exerted by the rail to the left wheel; T_2 – opposing torque exerted by the rail to the right wheel; θ_1 – torsion angle displacement between the traction motor and the left wheel; θ_2 – torsion angle displacement between the left and right wheels.

Fig. 2.1. Gearbox built in bogie and a schematic representation of the torsional vibration [66].

Direct torque control mainly includes several components, as illustrated in Fig. 2.2. The voltage and current signals of the traction inverter are measured, from which the flux ψ_α and ψ_β are obtained through a flux observation and calculation unit. Then, the actual torque value, denoted as T_e, is calculated using the torque calculation unit. Flux signals ψ_α and ψ_β generate the flux regulation signal ψQ via the flux linkage adjustment unit. Simultaneously, the flux linkage interval number is determined by the flux linkage position judgment unit. Finally, the torque adjustment signal TQ is produced by the torque adjustment unit [66].

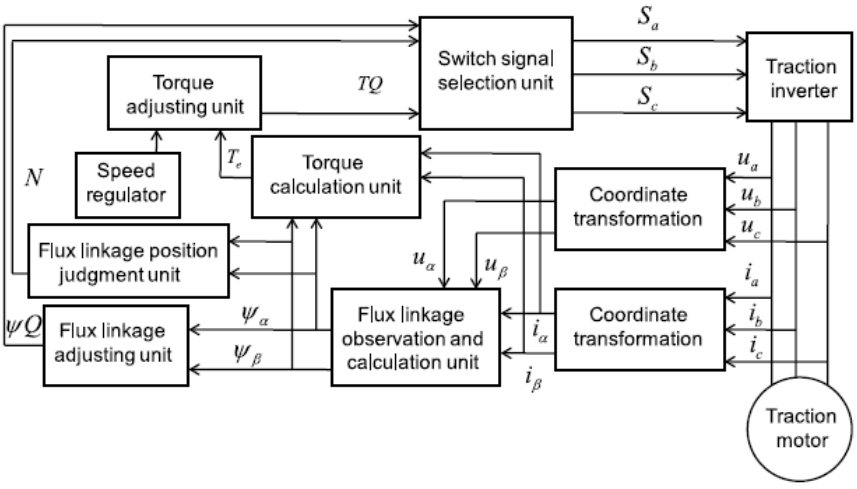

Fig. 2.2. Block diagram of direct torque control for traction motor [67].

2.2. Analysis of Vibration Studies of Traction Drive System Components Based on Field Tests of Electric Trains

2.2.1. Dynamic Characteristics and Problems in Traction Drive Systems of Regional and Suburban Trains

The design of traction drives for regional and suburban trains is very close in execution and primarily depends on the level of supply voltage 3 kVDC or 25 kVATS, as well as the layout of the car sections. The section includes the presence of 1 motor car, or 1 motor bogie, if each car of the train is driven [68]. The same applies to dual-system electric trains operating with two voltage levels, for example, as it happens on Estonian Railways. Regardless of the operating voltage, the receiving mechanism is a pantograph, or current collector, responsible for the uninterrupted supply of voltage to the input filter, and then to the converter circuit, which provides three-phase current power to traction asynchronous motors illustrated in Fig. 2.3. The motor, in turn, converts electrical energy into mechanical energy, the gearbox performs the function of converting the motor rotor speed to the speed of the wheel pair required for movement [69]. The MGU drive pinion performs the function of transmitting torque, transmitting it to the large (drive) pinion of the bogie connected to the wheel pair, thereby reducing the high speed and low torque of the traction motor to a low speed and high torque, which implements the possibility of moving the train [70], [71]. Due to the presence of combinations of nonlinear elements and various sources of both mechanical and electrical excitations in the circuit, as well as taking into account the periodicity of the loads and their intensity, oscillatory processes are inevitable [72]. The situation is also aggravated by high passenger traffic, as well as a combination of short and long hauls. Separately, it should be emphasized that trains with a collector drive and with an asynchronous drive can be operated simultaneously within one route branch, which also has a detrimental effect on the electromagnetic compatibility of the operating equipment [73], [74].

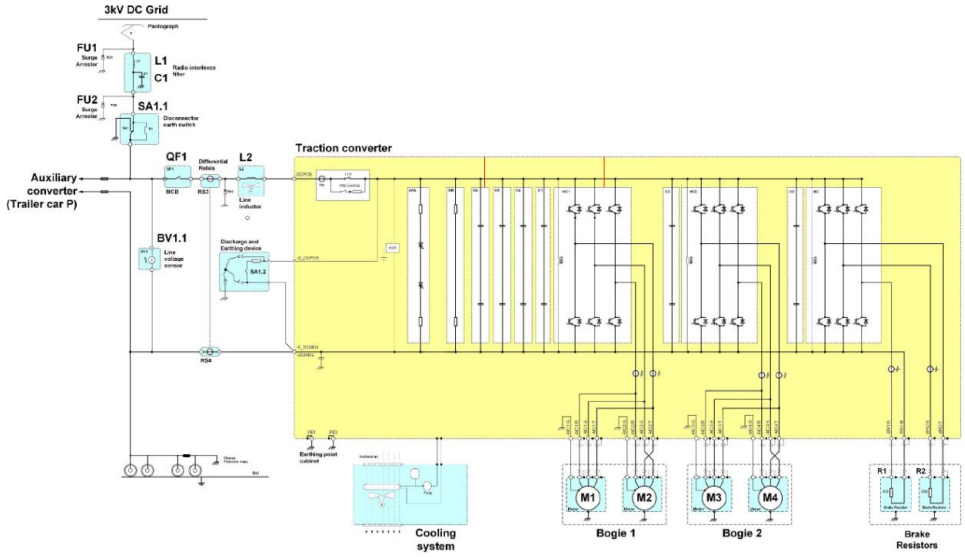

Fig. 2.3. Schematic representation of traction drive system for a regional train.

The combination of external factors and their impact on the stable operation of the drive is often determined by the quality of manufacturing the executive units of the rolling stock and the degree of their wear, or insufficiently high-quality maintenance and violation of routine maintenance and defect detection [75]. This especially applies to hard-to-reach places of the drive, one of which is the MGU, where access to the internal compartments and even visual inspection are very difficult. There is a high probability of wear, contact fatigue and cracks in the MGU mechanism due to continuous internal stresses of the structure, vibrations and single impacts [76], [77]. The dynamic behavior and response of the traction system to various excitation sources in various frequency ranges are the subject of works. Among the studies conducted, one can highlight the tendency to adhere to purely mechanical, such as the quality of the gear meshing of the MGU gears and the fatigue of transmission elements, or purely electrical excitation, for example, the harmonic torque of the electric motor, oscillations of the power supply system and harmonics generated by the PWM conversion [78], [79], [80].

2.2.2. Vibration Properties of Traction Motor

Due to the difference in the frequency of the voltage on the drive side and the power supply of the railway network, expressed in a multiple ratio, fluctuations in the motor current and electromagnetic torque, and as a result, accumulated vibrations, are inevitable.

Based on the equivalent mathematical model of a traction rectifier, the input power can be described as [79]:

$$P_{in} = U_s I_s \cos(\varphi) + U_s I_s \cos(2\omega_s t + \varphi). \tag{2.11}$$

The output power is given as:

$$P_{out} = U_{dc} I_L + C_d U_{dc} \frac{d_{u_{dc}}}{dt}. \tag{2.12}$$

where: U_s – effective value of grid side voltage;

I_s – effective value of grid side current;

ω_s – angular frequency on the grid side;

φ – phase angle between the grid-side current and voltage;

U_{dc} – average output voltage on the DC side;

$d_{u_{dc}}$ – fluctuation in the DC side voltage;

I_L – average load current.

The ripple component of the DC voltage can be determined as [79]:

$$u_{dc} = \frac{I_L \times sin(2\omega_s t + \varphi)}{2\omega_s \times C_d \times cos(\varphi)}. \tag{2.13}$$

From equation (2.13), we can deduce that the fluctuation frequency of the pulsating voltage on the DC side is twice the grid–side frequency, i.e., 100 Hz. Let $\Delta U_{dc} = I_L / 2\omega_s C_d \cos(\varphi)$, and the actual value of DC side voltage can be defined as:

$$u_{dc} = U_{dc} + \Delta U_{dc} \sin(2\omega_s t + \varphi). \tag{2.14}$$

Assuming that all switching devices within the traction inverters behave as ideal switches, the switching function can be described as:

$$S_v(t) = \frac{1}{2} + \sum_{k=odd}^{\infty} A_{vk} \times \cos k(\omega_n t + \varphi_v), \ (v = a, b, c). \tag{2.15}$$

where: $\varphi_a = 0$; $\varphi_b = -\frac{2\pi}{3}$; $\varphi_c = \frac{2\pi}{3}$; ω_n is the angular frequency of the inverter output voltage.

The output phase voltage of the traction inverter can be expressed as:

$$u_{vo} = u_{dc} \times \left(S_v - \frac{1}{2}\right) = U_{dc} \sum_{k=odd}^{\infty} A_{vk} \cos k(\omega_n t + \varphi_v) +$$
$$+ \frac{\Delta U_{dc}}{2} \sum_{k=odd}^{\infty} A_{vk} \times sin[(2\omega_s \pm k\omega_n)t + \varphi + k\varphi_v). \quad (2.16)$$

The output phase voltage of the traction inverter includes odd harmonic components from the steady–state DC voltage and harmonic components from the beat frequency. Since the coefficient A_{vk} is inversely related to $k\omega_n$, the higher the order of the beat frequency voltage component, the smaller its amplitude. Consequently, the amplitude of the beat frequency voltage component with angular frequency $2\omega_s \pm \omega_n$ is the largest. The beat frequency current in the traction motor is induced by the voltage beat frequency component of the traction inverter, forming a beat frequency torque with angular frequency $2\omega_s \pm \omega_n$, as follows:

$$T_d = \frac{3n_p}{2\pi f_1} \times I_{2d+} \times E_2 \times cos(2\omega_s t - \varphi_d) + \frac{3n_p}{2\pi f_1} \times I_{2d-} \times$$
$$\times E_2 \cos(2\omega_s t + \pi - \varphi_d). \quad (2.17)$$

where: f_1 – fundamental frequency of the motor stator voltage;

n_p – number of pole pairs;

E_2 – electromotive force generated by the motor;

$I_{2d\pm}$ – reduced value of rotor current at an angular frequency of $2\omega_s \pm \omega_n$ parts.

To dampen torque pulsations in AC-DC-AC traction drive systems, two methods are used: software and hardware using DC components in the DC link [79]. In case of imperfect calculations, or as a result of incorrect selection of filter components, this method may not be effective, in which case the pulsating torque of the motor will increase and already, to a greater extent, will affect the fatigue damage of the suspension and fasteners of the MGU. The MGU is located on the motor frame and is fixed in places, as shown in Fig. 2.4.

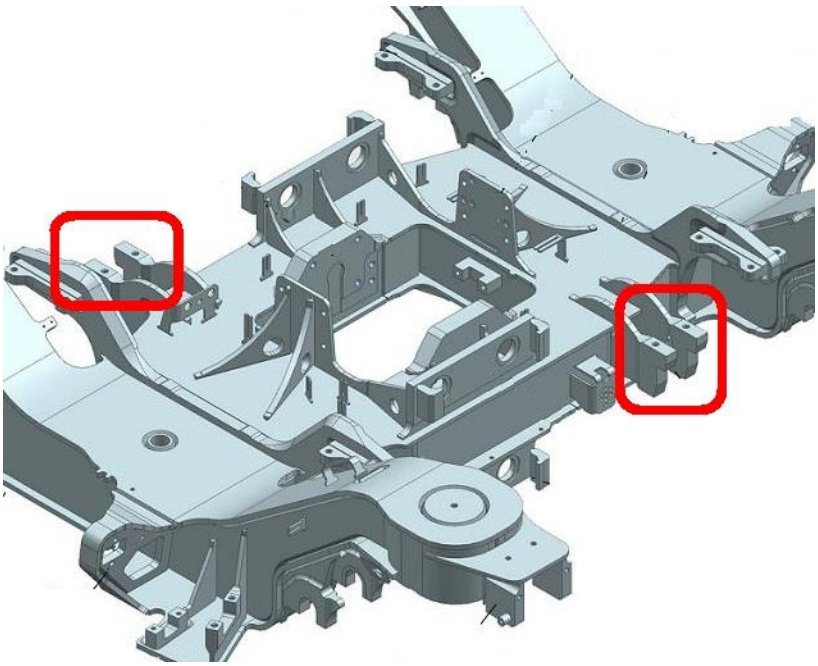

Fig. 2.4. Configuration of the traction motor suspension system.

Due to the fastening of the supporting MGU elements by welding to the bogie frame, fatigue processes in these connections occur even faster, especially under the influence of vibration and with a worn-out shock absorption system of cars. In addition to the above, among the external sources of vibration disturbances, the most obvious are excitations transmitted from the "rail-wheel" contact [81], [82].

The large and small gears within the gearbox generate meshing frequencies during their engagement. As a train operates, the meshing frequency escalates with increasing speed. The gear meshing frequency for the train's gearbox is defined as follows:

$$f_n = f_\omega n_z;\ f_{\omega 1} = \frac{v}{2\pi r};\ f_{\omega 2} = f_{\omega 1} a, \tag{2.18}$$

where: f_ω – gear rotation frequency, Hz;

$f_{\omega 1}$ – large gear rotation frequency, Hz;

$f_{\omega 2}$ – pinion rotation frequency, Hz;

v – train running speed, m/s;

r – wheel radius, m;

n_z – number of gear teeth;

a – gear ratio.

As can be seen in Fig. 2.5 (a), three main vibration frequencies can be present: the fundamental component f_i and two harmonic components $f_i + 2f_{net}$ and $f_i - 2f_{net}$. According to motor control theory, the operational speed of the train is governed by the fundamental frequency f_i. The other two components represent current harmonics generated by the pulsating component of the $2f_{net}$ frequency from the DC–link. As the fundamental current frequency f_i approaches the DC voltage pulsation frequency $2f_{net}$, the current components of these harmonic frequencies become more significant. From Fig. 2.5 (b), we can observe the two vibration frequencies, $2f_{net}$ and $4f_{net}$ throughout the acceleration, steady speed, and deceleration phases. Notably, the motor's electromagnetic torque harmonic component is most prominent when the fundamental current frequency f_i nears the DC voltage pulsation frequency $2f_{net}$.

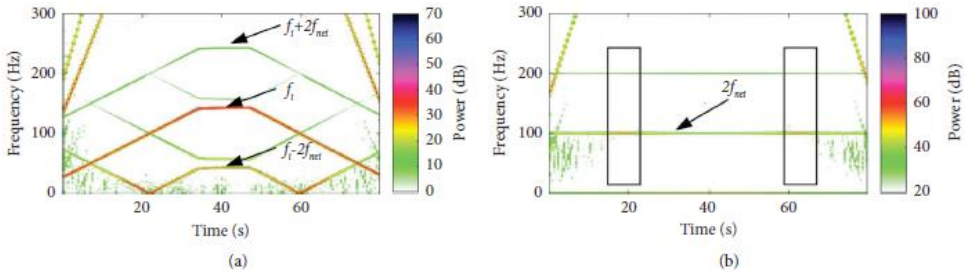

Fig. 2.5. Simulated results depicting the effects of 100 Hz dc voltage pulsation on the traction motor: (a) spectrum of stator current and (b) spectrum of torque [80].

2.2.3. Vibration Characteristics of Gearbox

The MGU is designed to transmit torque from the motor to the wheel of the motor bogie. Usually, in suburban and regional electric trains, the motor bogie contains two-wheel pairs and, accordingly, two MGUs. Inside the MGU, the motor rotor is connected to the input shaft of the gearbox (from the small gear side) by insulated elastic half-couplings, which are the first step

in damping vibrations from the drive side, then the system of gears and bearings, the output hollow shaft of the gearbox is connected by means of a wedge-packet clutch to the axle of the wheel pair, which is another step in damping torsional vibrations. Unlike the case of rigid coupling of the axle of the wheel pair with the input shaft of the gearbox, in the case described, the suspension and shock absorption system of the MGU itself is simplified [83], [84].

In Fig. 2.6. a) the process of tooth meshing of the gears of the traction gear is clearly oscillographed, where in the region of the natural vibration frequency equal to 2500 Hz, resonance of the MGU occurs. As a result, a significant increase in the vibration activity of the MGU can be observed. Fig. 2.6. b) represents a more detailed sample of the same process that is shown in Fig. 2.6. a).

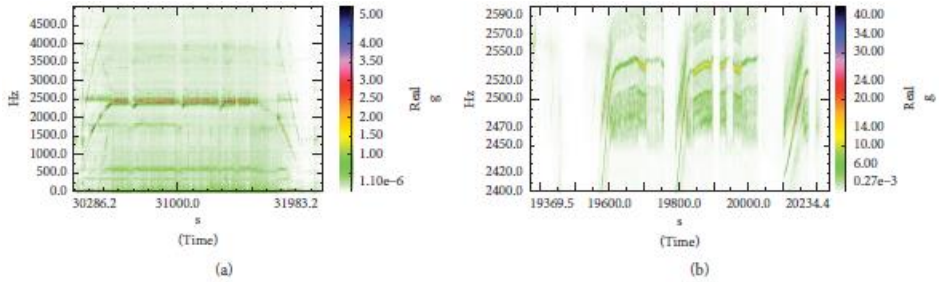

Fig. 2.6. Time–frequency diagram of gearbox vibration acceleration: (a) 0–5000 Hz and (b) 2400–2600 Hz [80].

2.3. Dynamics of Electric Machines

The primary mode of a motor reflects the intrinsic vibration properties of its mechanical structure, with each mode having a unique natural frequency, damping ratio, and vibration pattern. When the motor's electromagnetic force order corresponds with the modal order, and the frequency of the electromagnetic force is close to the natural modal frequency, even a minor electromagnetic force can lead to substantial vibration noise [85]. Therefore, understanding how motor design influences the natural frequency of the modal is key to preventing resonance and reducing motor vibration noise. An accurate model of the motor's stator system is vital for analyzing electromagnetic vibrations and noise, as well as conducting sensitivity studies of anisotropic material properties. Research shows that the damping coefficient can vary by more than sixfold at different temperatures, and modal frequencies can shift by several hundred Hz depending on temperature changes. However, only a limited number of studies have taken the core laminations and winding structure into account when modeling the stator, and there is currently no reliable method to determine the anisotropic parameters of the stator while considering the effects of windings and silicon steel laminations.

The main contributor to electromagnetic vibration noise in motors is the radial electromagnetic force created by the magnetic field in the air gap. In studies of electromagnetic force excitation, most research focuses on radial force excitation under ideal sinusoidal current inputs. Nevertheless, some studies have started investigating the effects of tangential electromagnetic forces, radial forces, and current harmonics on vibration noise. Traditional electromagnetic noise models tend to focus mainly on radial forces, often overlooking other components of electromagnetic force, which can reduce the precision of simulations. In

reference [86], only radial electromagnetic forces and the combination of radial, tangential, and axial forces are examined. Tangential electromagnetic forces affect electromagnetic noise, and models that include all three components – radial, tangential, and axial forces – offer a more accurate and dependable representation.

In reference [87], the researchers simulated the transient dynamics of a permanent magnet synchronous motor, considering both radial and tangential electromagnetic forces affecting vibration. The results, examined via frequency response analysis [88], revealed that tangential forces induce considerably greater tangential deformation in the stator teeth than radial forces. In the frequency spectrum, the second–order torque ripple frequency, closely tied to tangential electromagnetic forces, has a significant impact on electromagnetic vibration. In reference [89], a computational approach was proposed to investigate the influence of inverter harmonics on vibration noise in an electric vehicle equipped with an internal permanent magnet synchronous motor, spanning a wide speed range. The research identified the key parameters of the motor's electromagnetic power wave under the application of inverter current harmonics and examined the spectral characteristics of vibration noise during both constant speed torque control and weak magnetic speed control. The accuracy of the combined simulation model was validated through experimental testing.

2.3.1. Dynamics of Electric Machines in the Context of Magnetic Attraction

Mechanical oscillations in electrical machines are distinct due to the presence of a fluctuating magnetic field. If there is an uneven air gap between the rotor and stator, which can be caused by static or dynamic eccentricity of the rotor, the electromagnetic field generates a radial force acting on the rotor's centre, directed towards the region with the smallest air gap. This force is referred to as unbalanced magnetic pull (UMP).

UMP serves as a source of forced vibrations in hydro-generators and induction motors. In traction motors, the pronounced effect of electromagnetic forces on rotor oscillations is linked to both the multi-pole structure and the relatively narrow radial air gap between the rotor and stator. In alternating current (AC) induction motors, this air gap is minimal, which makes UMP comparable to other unbalanced forces. Additionally, the impact of UMP on rotor dynamics is also observed in various other types of electrical machines. Therefore, taking UMP into account is crucial in analyzing rotor dynamics in electrical machines [90], [91].

Currently, fully addressing UMP in rotor system analysis, and evaluating the effect of electromagnetic forces on rotor dynamics in electrical machines, remains a complex challenge. Numerous studies on rotor dynamics focus on understanding the influence of UMP on rotor systems. In research [91] was investigates the stability of hydrogenerator rotors while considering UMP. In study [92] explored the nonlinear effects of UMP on a turbogenerator. In research [93] examine the influence of UMP on the natural frequencies of rotor systems. In study [94] is used UMP in rotor dynamics research on hydrogenerators. In study [95] examines UMP and its effects on motor dynamics.

The magnitude of UMP is influenced by several factors: rotor eccentricity, the geometry of the machine, the induction of the magnetic field in the air gap, the magnetic properties of the rotor material, and the presence of parallel windings in the stator.

One particular approach, described in [95], is noteworthy. This method relies on numerical modeling and theoretical analysis of the electrical machine. The core idea is that the relationship between UMP and rotor eccentricity can be represented by a parametric dependency:

$$F_{em}(s) = K(s)z(s), \tag{2.19}$$

where $F_{em}(s)$ – electromagnetic interaction force;

$z(s)$ – describes the displacement of the rotor's center;

$s = i\omega$ – Laplace variable;

$K(s)$ – second–order transfer function.

$$K(s) = k_0 + \frac{k_{p-1}}{s-a_{p-1}} + \frac{k_{p+1}}{s-a_{p+1}}, \tag{2.20}$$

where: k_0, k_{p-1}, k_{p+1}, a_{p-1}, a_{p+1} – model parameters obtained through numerical computation based on the finite element analysis of the electrical machine;

p – number of pole pairs in the machine.

While these methods yield highly accurate results, analytical methods are also valuable for solving dynamic problems due to their efficiency and ease of result interpretation. Analytical techniques for calculating UMP often utilize Maxwell's stress tensor [92], [96]. To determine the force, the integral of the tensor over the surface is computed:

$$F_{UMP} = \oint_s \sigma \times n dS. \tag{2.21}$$

The primary components of Maxwell's tensor for the magnetic field are:

$$\sigma_r = \frac{1}{2\mu_2} \times (B_r^2 - B_\theta^2), \tag{2.22}$$

$$\sigma_\theta = \frac{1}{\mu_0} \times B_r \times B_\theta. \tag{2.23}$$

Since B_θ is negligible, it is assumed to be zero for simplification. This leads to an integral whose solution provides the UMP value:

$$F_{UMP} = \frac{lR}{2\mu_0} \int_0^{2\pi} B_r^2 n d\varphi. \tag{2.24}$$

Various solutions exist depending on specific assumptions. The simplest solution establishes a linear relationship between UMP and eccentricity:

$$F_{UMP} \approx \pi \times D \times l \times \left(\frac{B_\delta}{5000}\right) \times \frac{\varepsilon}{2k_c}, \tag{2.25}$$

where: $\varepsilon = \frac{e}{\delta_0}$.

The magnetic stiffness coefficient k_e can also be calculated:

$$k_e = \frac{\pi D l}{4\mu_0} \times \frac{B_\delta^2}{\delta_0}, \tag{2.26}$$

Nonlinear relationships provide more accurate values [96], [97]. For instance, there is an analytical expression for calculating UMP in isotropic electrical machines:

$$F_{UMP} = \frac{l \times J(\varepsilon,p) \times 2 \times \pi \times R_s \times \left(\frac{B_\delta}{k_c}\right)^2}{2 \times \mu_0}, \tag{2.27}$$

where: $J(\varepsilon, p)$ – function dependent on the relative rotor eccentricity ε and the number of pole pairs p.

The function $J(\varepsilon, p)$ is defined as:

$$J(\varepsilon,p) = \frac{\varepsilon^2 - \left(\frac{\left(1-\sqrt{1-\varepsilon^2}\right)}{\varepsilon}\right)^{2p} \times \left(\varepsilon^2 + 2*p*\sqrt{1-\varepsilon^2}\right)}{2 \times \varepsilon \times (\sqrt{1-\varepsilon^2})^3}, \tag{2.28}$$

Hydrogenerators, which have a large number of poles, have an average UMP value expressed as:

$$F_{UMP} = \frac{\mu_0 S_S^2 R_S^3 l\pi}{2(2p)^2 \delta_0^2} \times \frac{\varepsilon}{\sqrt{(1-\varepsilon^2)^3}}, \tag{2.29}$$

In the nonlinear formulation, the matrix equation describing the rotor system's dynamic model is:

$$[M]\{\ddot{u}\} + [C]\{\dot{u}\} + [K]\{u\} = \{F(t)\} + \{R\}, \quad (2.30)$$

where: $[M]$ – inertia matrix;

$[C]$ – damping matrix;

$[K]$ – stiffness matrix;

$\{\ddot{u}\}$, $\{\dot{u}\}$, $\{u\}$ – vectors of vibration accelerations, vibration velocities, and vibration displacements, respectively;

$\{F(t)\}$ – dynamic loads of any kind - both internal and external;

$\{R\}$ – reactions from nonlinear interactions accounting for the magnetic force between the rotor and stator.

Various integration methods, such as Runge–Kutta, Adams, and finite difference methods, can be applied to solve equation (2.30).

In the linear formulation, equation (2.30) can be simplified by including the magnetic force through the stiffness coefficient derived from equation (2.26) [95].

2.3.2. Unbalanced Magnetic Pull Forces in Axial Inductor Machines

Electromagnetic attraction forces that develop in electrical machines are due to the change in magnetic energy stored within the air gap as a function of the moving part's displacement. In rotating machinery, the tangential components of these forces produce electromagnetic torque, while the radial components generate forces acting perpendicular to the rotor's axis. These radial forces can be determined using the equation:

$$T = -\partial W_M / \partial \delta, \quad (2.31)$$

where: W_M is the magnetic energy stored in the air gap δ.

In machines featuring a symmetrical magnetic system–uniform air gap, consistent magnetic permeability of active materials along the flux path, an even number of slots in the tooth zone, and so forth–the radial magnetic attraction forces are balanced and do not adversely affect the machine's operation. However, when this transverse magnetic symmetry is disrupted, UMP forces emerge. These forces lead to increased shaft deflection, the creation and amplification of alternating radial loads on the shaft, and heightened bearing pressure, all of which must be accounted for in the machine's design. In machines with linear motion of the moving part, UMP forces increase slider deflection and bearing loads, accelerate wear, and necessitate greater mechanical strength of the slider [98].

Ultimately, the impact of UMP forces reduces the specific power output and torque of the electrical machine.

The main cause of UMP forces in rotating machines is the non-uniform air gap, usually resulting from the asymmetric (eccentric) positioning of the rotor in relation to the stator bore, assessed through rotor eccentricity. In linear machines, this imbalance is due to the uneven positioning of the slider in relation to the stator packs, measured by its transverse displacement. Even without radial rotor eccentricity, the uneven structure of the active magnetic materials in both the stator and rotor can induce UMP forces. The magnetic energy stored in the air gap is described as [98]:

$$W_M = \frac{1}{2} F^2 \times \Lambda. \quad (2.32)$$

Accordingly, the unilateral magnetic pull force is given by:

$$T = -\frac{1}{2} F^2 \frac{\partial \Lambda}{\partial \delta}. \quad (2.33)$$

Here F, Λ – denote the total MMF and the machine's permeance, respectively. However, the variation in magnetic permeance Λ due to steel structure inhomogeneity and the resultant

UMP force is negligible compared to the force caused by rotor eccentricity and the associated change in Λ. Therefore, this factor is typically disregarded in this context. The impact of asymmetry in the machine's tooth zone structure on the generation of radial electromagnetic attraction forces can only be assessed with specific structural details and is not considered here [98].

Rotor eccentricity can stem from both manufacturing and operational factors. Manufacturing errors include inaccuracies in the machining and assembly of parts, radial clearance caused by bearing backlash, and shaft deflection due to the weight of the rotor. Technological rotor eccentricity ε_t is typically considered constant, with its value determined by design and manufacturing standards. This eccentricity is usually around 5–15 % of the working air gap δ, i.e $\varepsilon_t = (0.05 \dots 0.15)\delta$. As manufacturing technology improves, ε_t decreases.

Operational eccentricity ε_{eq} arises during the machine's operation, primarily due to radial bearing wear. Its magnitude depends on manufacturing quality, operating conditions, the machine's purpose, and its expected service life; it is approximately $\varepsilon_{eq} = (0.1 \dots 0.2)\delta$. Operational eccentricity increases the machine's magnetic asymmetry and, consequently, the UMP force.

The total eccentricity of the machine is the sum of manufacturing and operational eccentricity, $\varepsilon = \varepsilon_t + \varepsilon_{eq}$. Taking this into account, and switching from a partial derivative to the ratio of increments, equation (2.31), without the negative sign, can be expressed as [99]:

$$T = \frac{W_{M_{(\delta\pm\varepsilon)}} - W_{M_{(\delta)}}}{\varepsilon}, \tag{2.34}$$

where: $W_{M_{(\delta)}}$ – magnetic energy stored in the air gap δ without radial rotor displacement;

$W_{M_{(\delta\pm\varepsilon)}}$ – magnetic energy stored with eccentricity ε.

For an inductor machine with p pole projections on the stator and n_R rotor segments (as in an axial inductor machine) [99], the magnetic field energy in the air gap can be calculated using equation (2.32):

$$W_M = n_R \times \frac{\sum_1^p F_i \cdot \Lambda_i}{2} = n_R \times \frac{(F_\delta \cdot K_E)^2 \cdot \sum_1^p \Lambda_i}{2}, \tag{2.35}$$

where: $F_i = F_\delta K_E$ – MMF of the $i-th$ projection;

F_δ – MMF across the air gap beneath the pole projection;

K_E – coefficient that accounts for the increase in MMF and EMF, considering voltage reduction due to the armature reaction.

By substituting equation (2.35) into equation (2.34), we obtain:

$$T = n_R \times (F_\delta K_E)^2 \times \frac{\left(\sum_1^p \Lambda_{i\varepsilon} - \sum_1^p \Lambda_{i\delta}\right)}{2\varepsilon}, \tag{2.36}$$

where: $\sum_1^p \Lambda_{i\delta}$ – total magnetic permeance of all pole projections in one stator segment when there is no rotor displacement ($\varepsilon = 0$);

$\sum_1^p \Lambda_{i\varepsilon}$ – sum of magnetic permeances of all pole projections in one stator segment when rotor displacement ($\varepsilon \neq 0$).

Since $\sum_1^p \Lambda_{i\varepsilon} = \Lambda_{1\varepsilon} + \Lambda_{2\varepsilon} + \cdots + \Lambda_{p\varepsilon}$ and $\sum_1^p \Lambda_{i\delta} = \Lambda_{1\delta} + \Lambda_{2\delta} + \cdots + \Lambda_{p\delta}$ the difference between these sums can be expressed as:

$$\sum_1^p \Lambda_{i\varepsilon} - \sum_1^p \Lambda_{i\delta} = \sum_1^p (\Lambda_{i\varepsilon} - \Lambda_{1\delta})_i = \sum_1^p \Delta\Lambda_i, \tag{2.37}$$

where: $\Delta\Lambda_i = (\Lambda_{i\varepsilon} - \Lambda_{i\delta})_i$ – change in magnetic permeance for $i - th$ pole projection ($i = 1.2 \ldots p$) between the cases with ($\Lambda_{i\varepsilon}$) and without ($\Lambda_{i\delta}$) rotor eccentricity.

Thus equation (2.37), UMP force can be calculated as:

$$T = n_R \times (F_\delta K_E)^2 \times \frac{\sum_1^p \Delta\Lambda_i}{2\varepsilon}, \quad (2.38)$$

To compute these sums of magnetic permeances in equation (2.36) or the sum of permeance differences in equation (2.38), the first step is to determine the air gap δ_i under each of the p stator pole projections must first be calculated using the expression:

$$\delta_i = \delta + \Delta_i, \quad (2.39)$$

where the variation in air gap size Δ_i under each pole projection due eccentricity ε is:

$$\Delta_i = \varepsilon \times \cos\gamma_i, \quad (2.40)$$

where: δ – uniform air gap when $\varepsilon = 0$.

The angle γ_i specifies the position of the pole projection and, when pole projections are evenly distributed around the stator bore, is given by:

$$\gamma_i = 360° \times (i - 1)/p, \quad (2.41)$$

measured clockwise from the vertical axis of symmetry of the first pole projection. To improve accuracy, it is essential to account for the pole projection shift angles according to the tooth zone structure.

Next, utilizing the parameters of the tooth zone and reference tables for specific magnetic permeances in different areas [100], the following specific permeabilities are calculated: λ_{PS} – specific permeability of the stator slot located opposite the rotor slot; λ_{P1} – specific permeability of the stator tooth opposite the rotor slot; λ_{P2} – specific permeability of the rotor tooth opposite the stator slot.

The specific permeability of the stator tooth facing the rotor tooth is determined using the following equation:

$$\lambda_{\delta i} = b_{zs}/\delta_{eqi}, \quad (2.42)$$

where: b_{zs} – width of the stator tooth;

δ_{eqi} – equivalent air gap for the for $i - th$ pole projection [99].

The magnetic permeabilities of each of the p pole projections are computed without rotor eccentricity and with eccentricity. After computing these permeances or their differences the sums of these permeabilities or the sums of their differences, are then used to calculate the pull force according to equation (2.36) or (2.37).

Initially, calculations are performed for the case where rotor eccentricity is absent ($\varepsilon = 0$). In this situation, assuming $p = zr$, i.e., $ts = tr$ [100]:

1. ratios defining the specific magnetic permeabilities of the tooth zone:

a) when $b_{nr}/b_{ns} \leq 1$; b_{ns}/δ; b_{ns}/b_{nr}; b_{zr}/b_{ns}; $b_{nr}/\delta_\ni$; b_{zr}/b_{nr}; where b_{nr}, b_{ns} – rotor and stator slot widths; b_{zs}, b_{zr} – rotor and stator tooth widths; δ and δ_{eq} – uniform and equivalent air gaps, where $\delta_{eq} = \delta \times K_\delta$, and K_δ – air gap coefficient;

b) when $b_{nr}/b_{ns} > 1$ (stator and rotor effectively swap roles) – b_{ns}/b_{nr}; b_{nr}/δ_{eq}; b_{zs}/b_{nr}; b_{nr}/δ; b_{zr}/b_{ns}; b_{ns}/δ;

2. specific magnetic permeabilities of the tooth zone from tables 1, 2 and 3:

a) when $b_{nr}/b_{ns} \leq 1$

$$\lambda_{PS} = f_P\left(\frac{b_{Pr}}{b_{Ps}}; \frac{b_{Pr}}{\delta}\right) \quad \lambda_{P1} = f_1\left(\frac{b_{zr}}{b_{Ps}}; \frac{b_{Ps}}{\delta}\right) \quad \lambda_{P2} = f_2\left(\frac{b_{zs}}{b_{Pr}}; \frac{b_{Pr}}{\delta_{eq}}\right).$$

b) when $b_{nr}/b_{ns} > 1$

$$\lambda_{PS} = f_P\left(\frac{b_{Ps}}{b_{Pr}}; \frac{b_{Pr}}{\delta_{eq}}\right) \quad \lambda_{P1} = f_1\left(\frac{b_{zs}}{b_{Pr}}; \frac{b_{Pr}}{\delta}\right) \quad \lambda_{P2} = f_2\left(\frac{b_{zr}}{b_{Ps}}; \frac{b_{Ps}}{\delta}\right).$$

3. The specific magnetic conductivity of the stator tooth:

when $b_{nr}/b_{ns} \leq 1$; $\lambda_\delta = b_{zs}/\delta_{eq}$ and when $b_{nr}/b_{ns} > 1$; $\lambda_\delta = b_{zr}/\delta_{eq}$;

4. The maximum and minimum permeances of the pole projection are given by:

$$\Lambda_{max} = \left(\lambda_\delta + \lambda_{PS}\frac{l+b_{zr}}{l}\right) \times a \times l \times \mu_0; \Lambda_{min} = (\lambda_{P1} + \lambda_{P2}) \times a \times l \times \mu_0, \quad (2.43)$$

where: l – axial length of one stator packet; a – number of teeth on the pole projection; $\mu_0 = 4\pi * 10^{-7}$ H/m – magnetic constant;

5. zero coefficients (constant) and first harmonic components of the Fourier series expansion of the pole projections magnetic conductivity (assuming that higher harmonics are significantly weakened by appropriate parameters of the tooth zone):

$$a_0 = \frac{\Lambda_{max}+\Lambda_{min}}{2}\chi_{eq} + \Lambda_{min}; a_1 = \frac{\Lambda_{max}+\Lambda_{min}}{2}, \quad (2.44)$$

where: $\chi_{eq} = \chi + \Delta\chi$, with $\chi = b_{zr}/0{,}5t_z$, and $\Delta\chi$ – correction factor [100];

6. magnetic conductivity of the pole projection:

$$\Lambda_{i\delta} = a_0 + a_1 \times cos[\alpha - (i-1) \times z_r \times \gamma_i], \quad (2.45)$$

where: α – rotor rotation angle; z_r – number of rotor teeth; $(i-1)z_r\gamma_i$ – phase lag of the first harmonic of the $i-th$ pole projection's magnetic permeability relative to the first harmonic of the first pole projection's permeability. Since the total magnetic permeability of the pole projections in an inductor machine is constant (does not depend on the rotor's rotation angle), $\lambda_{i\delta}$ м can be calculated at any angle α. It is naturally more convenient to do this at $\alpha = 0$, assuming that in this case, the rotor teeth and the teeth of the first pole projection coincide, resulting in $\lambda_{1\delta} = \Lambda_{max}$;

7. total magnetic permeability of the pole projections:

$$\sum_1^p \Lambda_{i\delta} = \Lambda_{1\delta} + \Lambda_{2\delta} + \cdots + \Lambda_{p\delta}. \quad (2.46)$$

A similar calculation is performed in the presence of rotor eccentricity ε, determining:

1) angle characterizing the position of the pole projection relative to the stator bore:

$$\gamma_i = 360° \times (i-1)/p; \quad (2.47)$$

2) air gap under each $i-th$ pole projection:

$$\delta_i = \delta + \varepsilon \times cos\,\gamma_i; \quad (2.48)$$

3) tooth zone parameter ratios determining specific magnetic permeabilities:

b_{nr}/δ_i; b_{nr}/δ_{eqi}; with $\delta_{eqi} = \delta_i K_\delta$, and relation b_{nr}/b_{ns}; b_{zr}/b_{ns}; b_{zs}/b_{nr} and others are taken from p.1, a and δ of the previous calculation;

4) specific magnetic conductivity of the tooth zone [100]:

$$\lambda_{PSi} = f_{Pi}\left(\frac{b_{Pr}}{b_{Ps}}; \frac{b_{Pr}}{\delta_i}\right) \quad \lambda_{P1i} = f_1\left(\frac{b_{zr}}{b_{Ps}}; \frac{b_{Ps}}{\delta_i}\right) \quad \lambda_{P2i} = f_{2i}\left(\frac{b_{zs}}{b_{Pr}}; \frac{b_{Pr}}{\delta_{eqi}}\right), \quad (2.49)$$

or

$$\lambda_{PSi} = f_{Pi}\left(\frac{b_{Ps}}{b_{Pr}}; \frac{b_{Pr}}{\delta_{eqi}}\right) \quad \lambda_{P1i} = f_{1i}\left(\frac{b_{zs}}{b_{Pr}}; \frac{b_{Pr}}{\delta_i}\right) \quad \lambda_{P2i} = f_{2i}\left(\frac{b_{zr}}{b_{Ps}}; \frac{b_{Ps}}{\delta_i}\right), \quad (2.50)$$

depending on the coefficent value b_{nr}/b_{ns};

5) specific magnetic permeability of the tooth:

$$\lambda_{\delta i} = \frac{b_{zs}}{\delta_{eqi}} \text{ when } \frac{b_{Pr}}{b_{Ps}} \leq 1 \text{ or } \lambda_{\delta i} = \frac{b_{zr}}{\delta_{eqi}} \text{ when } \frac{b_{Pr}}{b_{Ps}} > 1; \quad (2.51)$$

6) maximum $\Lambda_{i\,max}$ and minimum $\Lambda_{i\,min}$ conductivity of the pole projections:

$$\Lambda_{i\,max} = \left(\lambda_{\delta i} + \lambda_{PSi}\frac{l+b_{zr}}{l}\right) al\mu_0;\ \Lambda_{i\,min} = (\lambda_{P1i} + \lambda_{P2i}) al\mu_0. \quad (2.52)$$

7) coefficients a_{0i} and a_{1i}:

$$a_{0i} = \frac{\Lambda_{i\,max}+\Lambda_{i\,min}}{2}\chi_{eq} + \Lambda_{i\,min};\ a_{1i} = \frac{(\Lambda_{i\,max}-\Lambda_{i\,min})}{2}. \quad (2.53)$$

8) magnetic permeances of the pole projections at the chosen parameter from p. 6 of the earlier α:

$$\Lambda_{i\varepsilon} = a_{0i} + a_{1i} \times cos[\alpha - (i-1) \times z_r \times \gamma_i]. \quad (2.54)$$

9) variation in magnetic permeances of the pole projections with and without eccentricity:

$$\Delta\Lambda_i = \Lambda_{i\varepsilon} - \Lambda_{i\delta}. \quad (2.55)$$

10) combined magnetic permeability of the pole projections:

$$\sum_1^p \Lambda_{i\varepsilon} = \Lambda_{1\varepsilon} + \Lambda_{2\varepsilon} + \cdots + \Lambda_{p\varepsilon}. \quad (2.56)$$

11) total difference in magnetic permeances of the pole projections:

$$\sum_1^p \Delta\Lambda_i = \Delta\Lambda_1 + \Delta\Lambda_2 + \cdots + \Delta\Lambda_p. \quad (2.57)$$

12) asymmetrical magnetic attraction force is calculated using either formula (2.36) or (2.37).

Thus, when the rotor has an eccentricity of approximately 20 % of δ, the resulting unbalanced magnetic attraction force surpasses 30 % of the rotor's weight, which should be accounted for.

2.3.3. Mathematical Representation of an Induction Motor in a Multiphase Coordinate System with Rotor Circuit Asymmetry

To develop an $n-phase$ mathematical model, commonly accepted principles and formulas from the simulation of induction motors were utilized [101].

The system of differential equations for an $n-phase$ machine is expressed as:

$$\begin{cases} \frac{d\psi_s^{(1)}}{dt} = U^{(1)} - R_s \times i_s^{(1)}; \\ \quad .. \\ \frac{d\psi_s^{(n)}}{dt} = U^{(n)} - R_s \times i_s^{(n)}; \\ \frac{d\psi_R^{(1)}}{dt} = 0 - R_R \times i_R^{(1)}; \\ \quad .. \\ \frac{d\psi_R^{(n)}}{dt} = 0 - R_R \times i_R^{(n)}, \end{cases} \quad (2.58)$$

where: R_s, R_R – stator and rotor resistance;

i_s, i_R – stator and rotor current;

ψ_s, ψ_R – stator and rotor flux linkage;

U – input voltage to the stator winding.

From the above system of equations (2.58), it is clear that the variable determines the number of cores. As the number of rotor cores increases, the complexity of the system also grows.

The developed mathematical model is intended for studying an induction motor with a squirrel-cage winding when rotor cores are broken. The input voltage vector is composed of components from both the stator and rotor, but since the motor has a squirrel-cage winding, the input effects on the rotor circuit will always be zero [102].

The input voltage vector is formulated as:

$$U_{IN} = [U^{(1)}U^{(2)}..U^{(n)}0..0^{(n)}]^T. \quad (2.59)$$

The voltages in the multidimensional coordinate system are defined as:

$$U^{(n)}(t) = U_m \times cos(\theta + \varphi_{ps}), \tag{2.60}$$

where U_m – amplitude value, $\theta = 2\pi ft$; φ_{ps} – phase shift angle.

Voltages in a three–phase system are represented by:

$$U_A(t) = \sqrt{2}U_A\, sin(\omega t), \tag{2.61}$$

$$U_B(t) = \sqrt{2}U_B\, sin(\omega t - \tfrac{2\pi}{3}), \tag{2.62}$$

$$U_C(t) = \sqrt{2}U_C\, sin(\omega t + \tfrac{2\pi}{3}), \tag{2.63}$$

where: U_A, U_B, U_C – effective voltages.

The amplitude of the voltage for each stator phase is unaffected by the choice of the coordinate system and can be described as:

$$U_m = \sqrt{U^2(t) + \frac{\left(U_B(t) - U_C(t)\right)^2}{3}} = \sqrt{2}U, \tag{2.64}$$

where: U – effective voltage for each stator phase.

The angle θ is calculated from the voltage equations in the three–phase system:

$$\theta = arctan\left(\frac{U_A(t)\sqrt{3}}{U_B(t) - U_C(t)}\right). \tag{2.65}$$

The angular phase difference between the voltage components in the multidimensional system is determined by the number of cores n:

$$\varphi_{ps} = \frac{2\pi}{n}. \tag{2.66}$$

Using Ampère's law, the stator and rotor currents are calculated as follows:

$$\begin{bmatrix}\overline{\Psi}_S\\ \overline{\Psi}_R\end{bmatrix} = L_0 \begin{bmatrix}\overline{I}_S\\ \overline{I}_R\end{bmatrix} \Rightarrow \begin{bmatrix}\overline{I}_S\\ \overline{I}_R\end{bmatrix} = {L_0}^{-1} \begin{bmatrix}\overline{\Psi}_S\\ \overline{\Psi}_R\end{bmatrix}, \tag{2.67}$$

where: $L_0 = \begin{bmatrix}L_{S0} & L_{SR}\\ L_{RS} & L_{R0}\end{bmatrix}$ – inductance matrix;

L_{S0}, L_{R0} – self–inductance matrices for the stator and rotor;

L_{SR}, L_{RS} – mutual inductance matrices.

$\overline{\Psi}_S = \begin{bmatrix}\Psi_S^{(1)}\\ \vdots\\ \Psi_S^{(n)}\end{bmatrix}$ – stator flux linkage vector;

$\overline{\Psi}_R = \begin{bmatrix}\Psi_R^{(1)}\\ \vdots\\ \Psi_R^{(n)}\end{bmatrix}$ – rotor flux linkage vector;

$\overline{I}_S = \begin{bmatrix}I_S^{(1)}\\ \vdots\\ I_S^{(n)}\end{bmatrix}$ – stator current vector;

$\overline{I}_R = \begin{bmatrix}I_R^{(1)}\\ \vdots\\ I_R^{(n)}\end{bmatrix}$ – rotor current vector.

The self–inductance matrices are determined using an auxiliary matrix $Corr(\varphi)$, which depends on the phase angle φ. This auxiliary matrix is represented as:

$$Corr(\varphi) = \begin{bmatrix} 0 & cos(\varphi) & cos(2\varphi) & .. & cos(-a\varphi)\\ cos(-\varphi) & 0 & cos(\varphi) & .. & cos(-b\varphi)\\ cos(-2\varphi) & cos(-\varphi) & 0 & .. & cos(-c\varphi)\\ \vdots & \vdots & \vdots & .. & \vdots\\ cos(-\alpha\varphi) & cos(-b\varphi) & cos(-c\varphi) & .. & 0 \end{bmatrix}, \tag{2.68}$$

$$a = (n-1); b = (n-2);\ c = (n-3).$$

The stator self–inductance matrix is defined as:

$$L_{S0} = L_m \times Corr(\varphi) + diag\left[L_S^{(1)}, L_S^{(2)} \dots L_S^{(n)}\right], \tag{2.69}$$

where: L_m – maximum mutual inductance between the stator and rotor phases.

Similarly, the rotor self–inductance matrix is given by:

$$L_{R0} = L_m \times Corr(\varphi) + diag\left[L_R^{(1)}, L_R^{(2)} \dots L_R^{(n)}\right]. \tag{2.70}$$

Calculating the matrices L_{S0} and L_{R0} does not require significant computational power, as there is no dependence on the rotor's rotation angle [102]. The elements of L_{SR} and L_{RS} are also determined using an auxiliary matrix dependent on φ and γ:

$$Cosr(\gamma, \varphi) = \begin{bmatrix} cos(b) & cos(b-\varphi) & .. & cos(b-a*\varphi) \\ cos(b-\varphi) & cos(b-\varphi-\varphi) & .. & cos(b-a)(\varphi-\varphi) \\ \vdots & \vdots & .. & \vdots \\ cos(b-\alpha\varphi) & cos(b-\varphi-a\varphi) & .. & cos(b-a)\varphi-a\varphi) \end{bmatrix}, \tag{2.71}$$

$$a = (n-1); b = \gamma_e.$$

where: $\frac{d\gamma_e}{dt} = z_p \times \int \omega_r dt$ – rotor rotation angle.

The final expressions for determining L_{SR} and L_{RS} are:

$$L_{SR} = L_m \times Cosr(\gamma, \varphi)^T, \tag{2.72}$$

$$L_{RS} = L_m \times Cosr(\gamma, \varphi). \tag{2.73}$$

After all transformations, the system of differential equations becomes:

$$\begin{bmatrix} \frac{d_{\Psi_S^{(1)}}}{dt} \\ \vdots \\ \frac{d_{\Psi_S^{(1)}}}{dt} \\ \frac{d_{\Psi_S^{(1)}}}{dt} \\ \vdots \\ \frac{d_{\Psi_S^{(1)}}}{dt} \end{bmatrix} = \begin{bmatrix} U^{(1)} \\ \vdots \\ U^{(n)} \\ 0 \\ \vdots \\ 0^{(n)} \end{bmatrix} - R \cdot L_0^{-1} \times \begin{bmatrix} \Psi_S^{(1)} \\ \vdots \\ \Psi_S^{(n)} \\ \Psi_R^{(1)} \\ \vdots \\ \Psi_R^{(n)} \end{bmatrix}, \tag{2.74}$$

where: $R = \begin{bmatrix} R_{S0} & 0 \\ 0 & R_{S0} \end{bmatrix}$ – primary resistance matrix;

$R_{S0} = diag\left[\mathrm{R}_S^{(1)}, \mathrm{R}_S^{(2)} .. \mathrm{R}_S^{(n)}\right]$ – stator resistance matrix;

$R_{R0} = diag\left[\mathrm{R}_R^{(1)}, \mathrm{R}_R^{(2)} .. \mathrm{R}_R^{(n)}\right]$ – rotor resistance matrix.

The electromagnetic torque of the induction motor is calculated using the stator and rotor currents:

$$M_{et} = -z_p \times \bar{I}_S^{\ T} \times L_n \times \bar{I}_R \times \frac{3}{n}, \tag{2.75}$$

where: z_p – number of pole pairs;

$$s(\varphi, b) = \begin{bmatrix} sin(b) & sin(b-\varphi) & .. & sin(b-a\times\varphi) \\ sin(b-\varphi) & sin(b-\varphi-\varphi) & .. & sin(b-a)(\varphi-\varphi) \\ \vdots & \vdots & .. & \vdots \\ sin(b-\alpha\varphi) & sin(b-\varphi-a\varphi) & .. & sin(b-a)\varphi-a\varphi) \end{bmatrix}, \tag{2.76}$$

$$a = (n-1); b = \gamma_e$$

– an auxiliary matrix.

$$L_n = \frac{d[L_{RS}]}{d\gamma_e} = -s(\varphi, \gamma_e) \times L_m. \tag{2.77}$$

To ensure the required power on the motor shaft in the $n-$ phase coordinate system, a coefficient $3/n$, which allows the rated torque of the motor to be maintained regardless of the dimensionality of the differential equation system [103]. The mechanical part of the motor is modeled as a single-mass system:

$$M_{et} - M_C = J \times \frac{d\omega}{dt}, \tag{2.78}$$

where: J – motor moment of inertia; M_C – load torque.

Simulation of bar breakage in this mathematical model is implemented by introducing additional resistance into the R_{R0} matrix for the corresponding core.

For diagnosing rotor bar breakage, the resultant stator current vector magnitude (envelope of stator currents) is used:

$$I_{m1}(t) = \sqrt{I_S^{(1)}(t) + I_S^{(2)}(t) + I_S^{(3)}(t) + \cdots I_S^{(n)}(t)}, \tag{2.79}$$

where: $I_S^{(1)}(t)$ – stator phase current.

To align the stator current envelope in the $n-phase$ coordinate system with the three–phase system, a scaling factor k, which depends on the system's dimensionality:

$$k = \sqrt{\frac{3}{n}}. \tag{2.80}$$

The stator current envelope in the three–phase system can be found using the expression:

$$I_m(t) = I_{m1}(t) \cdot k, \tag{2.81}$$

where $\mathrm{I}_{m1}(t)$ – envelope of the stator currents in the multiphase system.

2.4. Design and Technological Model of the Air Gap in the Asynchronous Motor

The design of the MGU is such that, due to the single-support device of the traction motor, the second end of the rotor is attached to the input shaft of the gearbox through an insulated coupling, due to which the requirements for the accuracy of the stator core (inner diameter) are extremely strict [104]. In such a design, the air gap is the most vulnerable point, and its unevenness negatively affects the energy parameters of the machine. The effect of the eccentricity of the rotor axis relative to the stator axis of the motor can be described by the expression:

$$\varepsilon_{max} = \frac{\varepsilon_{max}}{\gamma_{min}} \times 100\%, \tag{2.82}$$

where: ε_{max} is maximum eccentricity of the rotor core axis relative to the stator bore axis, mm, both parameters γ_{min} and ε_{max} included in the equation are determined by establishing the dimensional chain of the sample shown in Fig. 2.7.

The presence of an uneven air gap between the stator and the rotor of the motor, in addition to reducing the efficiency of the asynchronous motor, can significantly increase the unbalanced magnetic force acting on the rotor, which can be multiple compared to the calculated values. At the same time, the service life of the bearings is reduced, and in the worst case, when the shaft axis is shifted, direct contact between the rotor and the stator can occur. The rotor eccentricity is a significant factor that also affects magnetic noise. With an increase in misalignment from 0.05° to 0.5°, the equivalent load can increase by 2.6–2.9 times [105].

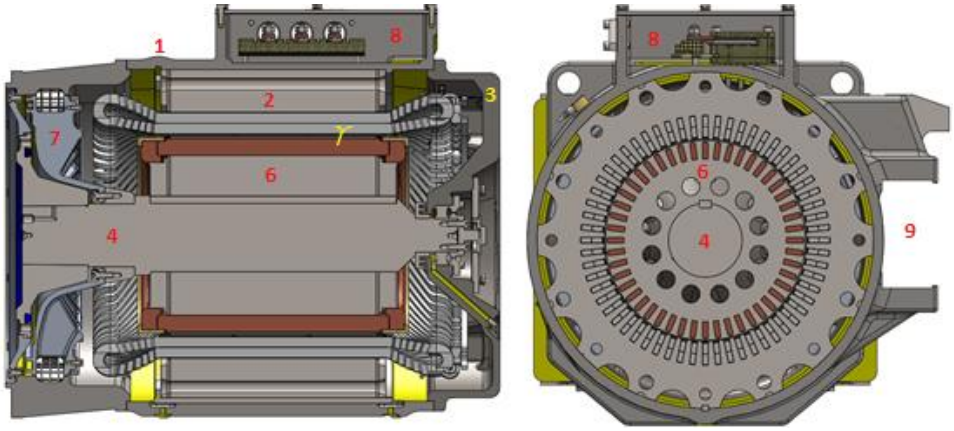

Fig. 2.7. Design and Schematics of Dimensional Chains for Asynchronous Motors,

where: 1 – housing; 2 – stator core; 3 – bearing shields; 4 – shaft; 5 – rotor core; 6 – ventilator; 7 – terminal box; 8 – mounting location; 9 – casing; Υ – air gap.

To create a mathematical model in [105] the following expression is proposed:

$$\gamma_{din} = \gamma - e_{st}\cos\varphi - z_0 \times cos[48EJ(l^3 mp\omega^2)^{-1}\varphi]^{\frac{1}{2}}, \quad (2.83)$$

where:

- φ, z_0 – generalized coordinates representing the rotor's rotation angle (degrees) and the dynamic eccentricity of the rotor axis relative to the stator (mm), respectively;
- E – modulus of elasticity of the rotor shaft material (kg/mm²);
- J – moment of inertia of the rotor (mm⁴);
- l – distance between rotor supports (mm);
- mp – rotor's mass (kg);
- ω – rotational frequency of the rotor (s⁻¹);
- e_{st} – eccentricity of the rotor's axis relative to the stator hole (static eccentricity).

For the three-dimensional model the following expression is proposed [105]:

$$\gamma_{vdin} = \frac{a_c(z)b_c(z)}{[b_p^2(z)cos^2\alpha + \alpha_p^2(z)sin^2(\alpha)]^{\frac{1}{2}}} - \frac{a_p(z)b_p(z)}{[b_p^2(z)cos^2\alpha + \alpha_p^2(z)sin^2(\alpha)]^{\frac{1}{2}}} -$$
$$-e_{st}\cos\varphi - z_0 \times cos[48EJ(l^3 mp\omega^2)^{-1}\varphi]^{\frac{1}{2}}, \quad (2.84)$$

where:

- z – coordinate of the asynchronous motors cross-section along its rotation axis;
- α – angle between the current radius of the stator or rotor and the horizontal plane;
- α_c, α_p, b_c, b_p – major semi–axes of the stator and rotor bore cross–sections, considered respectively along the horizontal X and vertical Y axes of the asynchronous motor.

To assess the contribution of precision design and operational factors to the air gap deviations, expression (2.84) can be transformed as follows:

$$\Delta\gamma_{vddin} = \Delta\gamma_n + \Delta\gamma_e + \Delta\gamma_{ke}, \quad (2.85)$$

where:

- $\Delta\gamma_n = \gamma_n - \Delta\gamma_n$ – deviation of the air gap value from the nominal due to errors in the stator and rotor hole.
- $\Delta\gamma_e = -e_{st}\cos\varphi$ – deviation of the air gap value from the nominal due to static eccentricity of the rotor relative to the stator.

$$\Delta\gamma_{keq} = -z_0 \times cos\sqrt{\frac{48EJ}{l^3 m\omega^2}}\varphi, \tag{2.86}$$

– deviation of the air gap value from the nominal due to design–operational factors.

An analysis of the factors contributing to the overall air gap error shows that the greatest impact comes from the static eccentricity of the rotor ($\Delta\gamma_e = 56$ %). This is followed by errors in the stator and rotor ($\Delta\gamma_n = 35$ %), and design-operational factors ($\Delta\gamma_{keq} = 9$ %) [106].

Deviation from the required geometric dimensions specified by the drawing may result in unevenness of the motor air gap. To describe the set of geometric factors and their influence on the manufacturing accuracy of mating parts in [107] a system of equations is proposed.

As a result, mathematical models were derived to describe the changes in ovality Δp_n and shrinkage $\Delta\overline{R}_n$ of the stator core hole during the pressing process into the housing:

$$\Delta p_n = c\left[1 - \frac{1}{\pi}\right]\left[\overline{\Delta}_n + \frac{1}{2}(p_{nn} + p_h) - \Delta_c\right]. \tag{2.87}$$

$$\Delta\overline{R}_n = -\frac{c}{2}\left[1 + \frac{1}{\pi}\right]\left[\overline{\Delta}_n + \frac{1}{2}(p_{nn} + p_h) - \Delta_c\right], \tag{2.88}$$

where:

- Δ_c – interference on one side between the core and the housing;
- c – coefficient representing the influence of design factors.

The non–roundness p_c and average radius $\overline{R}_c$ of the stator hole after pressing into the housing:

$$p_c = p_n + c\left[1 - \frac{1}{\pi}\right]\left[\overline{\Delta}_n + \frac{1}{2}(p_{nn} + p_h) - \Delta_c\right]. \tag{2.89}$$

$$\overline{R}_c = \overline{R}_n - \frac{c}{2}\left[1 + \frac{1}{\pi}\right]\left[\overline{\Delta}_n + \frac{1}{2}(p_{nn} + p_h) - \Delta_c\right]. \tag{2.90}$$

These models help determine the precision of the stator hole, based on the interference fit and the accuracy of the housing and stator core parameters.

Using these mathematical models, a method was developed to calculate the dimensions and tolerances for the geometric parameters of stator assemblies [107]:

- The tolerance for changes in the ovality of the stator core hole is:

$$\delta_{\Delta p_n} = \frac{1}{K_p}\sqrt{\delta_{p_c}^2 - K_p^2\delta_{p_n}^2}. \tag{2.91}$$

- The tolerance for stator frame ovality:

$$\delta_{p_h} = \frac{\sqrt{\delta_{\Delta p_c}^2 - \sum_{i=1}^{n-1}\left(\frac{\partial F}{\partial xi}\right)^2 K_i^2\omega_i^2}}{\left|\left(\frac{\partial F}{\partial p_c}\right)\right|K_p}. \tag{2.92}$$

- The diameter of the stator core bore:

$$D_n = D_c + c\left[1 + \frac{1}{\pi}\right]\left[\overline{\Delta}_N + \frac{1}{2}(p_{nN} + p_{cm}) + \Delta_{NA}\right] - z. \tag{2.93}$$

where:

z – allowance for machining the stator hole.

Statistical and calculated data reveal that over 80 % of the errors in the diameter and shape of the stator hole are caused by errors in the housing hole.

2.5. Second Chapter Conclusions.

Based on the content of Chapter 2, the following conclusions can be drawn regarding the dynamics of electric trains and the role of traction transmission:

1. Harmonic vibrations, especially due to non-sinusoidal AC inputs, directly affect the motor and drive systems, influencing speed variations and vibrations throughout the vehicle.
2. Non-sinusoidal currents introduced by inverters lead to harmonic distortions, which in turn cause pulsating torques. These torques impact the overall stability of the train, increasing mechanical vibrations that propagate through the drive system.
3. In practice, modeling methods such as synchronous remodulation methods have been applied to control and reduce harmonic oscillations. These methods improve the smoothness of the traction system and reduce mechanical wear by optimizing the inverter performance and controlling harmonic effects.
4. Direct torque control systems, along with vibration analysis models, help mitigate the adverse effects of electrical harmonics and mechanical vibrations. These systems are essential for maintaining the performance and longevity of the traction drive components.
5. In electrical machines, particularly with narrow air gaps, UMP forces significantly influence rotor dynamics, contributing to mechanical oscillations and vibrations. These forces must be accounted for in the design of rotor systems to prevent mechanical failures.
6. Gearbox resonance, especially around specific frequencies (e.g., 2500 Hz), can lead to increased vibration amplitudes, highlighting the need for precise gearbox designs to mitigate the impact of natural frequency interactions with operational stresses.
7. The coupling between the electrical and mechanical components of the train, including the rotor and gear systems, plays a critical role in the vehicle's dynamic responses. Effective management of this coupling is vital for reducing system vibrations and ensuring the reliability of trains.

CHAPTER 3. ANALYSIS OF WEAR IN TRACTION GEAR SYSTEMS OF ELECTRIC RAIL TRANSPORT

A number of reports submitted on the results of investigations conducted on the failure of traction drive systems of rolling stock show the insufficiency of organized initiatives to substantiate the importance of the role of diagnostics of manufactured products and the proper level of their operation in subsequent periods of the equipment life cycle. In connection with the increased load on the railway network, constant coordination of the implementation of regulatory procedures aimed at improving the quality of products supplied to the railway is required.

3.1. Operational Conditions and Requirements for Traction Drives

The main tasks that need to be implemented at the design and testing stage of the rolling stock traction equipment kit are:

1. Perform the main function of the drive – provide traction, i.e., convert and transmit energy from the source to the drive (executive) mechanism. Here, it is necessary to consider both a wide operating range of torque and operating speeds, and among the operating modes, it is necessary to highlight the most critical ones – starting the movement and breaking the train.

2. Damp vibrations and prevent the possible influence of high-frequency regulation on the vibration state of the driven object, in particular the MGU.

3. Ensure reliable and safe operation of electric rolling stock in a wide climatic range.

Here it should be noted that the traction drive itself is a strong source of heat generation, which in some cases, such as disconnecting the drive after a long period of operation during the overnight period of standing, can cause the formation of condensate inside the motor with subsequent insulation flashover when it is turned on [108], [109].

Of course, when designing the traction drive of an electric train, in addition to the main traction-energy rating, i.e., when all the provided units and mechanisms operate without disconnection, an allowance is made for semi-emergency and emergency modes, when the train can move to the repair site without disembarking passengers, or to the nearest parking place for disembarking passengers [109].

The traction drive of an electric train is mainly subjected to the load created by the traction torque.

When the EMU moves over uneven support surfaces, the torque on its drive wheels will be different, even on a straight horizontal section. This applies even more to curved sections of the support surface. But when analyzing the traction and speed properties of the EMU, it is customary to consider them for rectilinear motion, without considering the unevenness of the support surface and the difference in radii between the wheels of the same axle. In the absence of external slip of the drive wheels, the number of drive axles (wheel pairs) is of no fundamental importance for the model built on the above assumptions. When determining the total traction torque of the drive wheels, it is necessary to consider all the components of the resistance overcome by the motor in the process of transmitting energy to the drive wheels, as well as the dissipation of energy in the transmission mechanisms. In the transmission, this torque is converted by reduction elements (gear transmissions). The conversion of torque is accompanied by losses, which are considered by means of the efficiency of the mechanical transmission. At

the same time, part of the transmitted energy of the electric motor is spent on accelerating the rotating masses (parts) of the transmission, which are also connected to the drive wheels. Therefore, when overcoming the resistance to the acceleration of the transmission masses, it is necessary to consider the efficiency of the reduction gear elements.

The motion mode of the EMU is determined by the ratio of all forces and moments acting on it. An analysis of all forces acting on the EMU during its motion shows that under normal operating conditions, three motion modes are possible: traction, coasting and braking, Fig. 3.1. (see *V* characteristic).

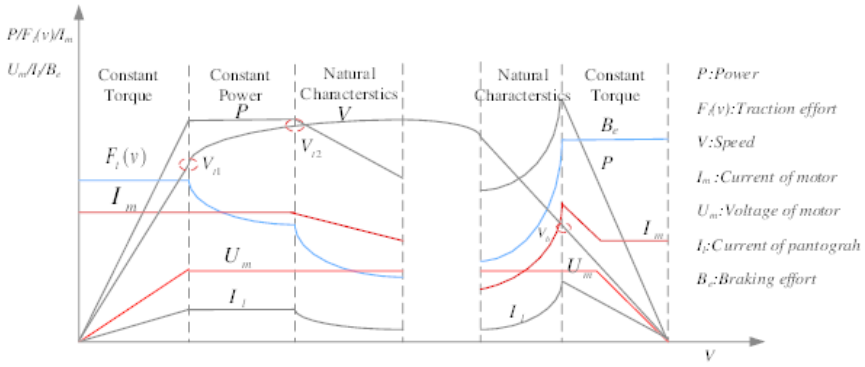

Fig. 3.1. Traction and braking characteristics of EMU.

The EMU motion mode is determined by the ratio of all forces and moments acting on it. Analysis of all forces acting on the EMU during its motion shows that three motion modes are possible under normal operating conditions: traction, coasting and braking, Fig. 3.1. In the traction mode, when the longitudinal reaction R_{x2} on the drive wheels (traction force of the drive wheels $F_к$) is greater than the forces of resistance to movement F_f, the acceleration of the EMU is greater than zero (0), therefore, the EMU moves with acceleration. If in the traction mode ($F_к = F_f$) the acceleration of the rolling stock is zero (0) and the EMU moves at a constant speed. In the coasting mode, the traction force is zero ($F_к = 0$), the EMU motion mode is determined by the force of resistance to movement F_f during coasting. On a horizontal section of the track in the latter case, the acceleration of the EMU is negative (0), acceleration becomes deceleration and the speed of the EMU decreases.

3.2. Dynamics and Durability of Electric Train Traction Drives

For each type of electric train, which is designed for a specific railway network and schedule, there is a loading cyclogram that takes into account the distances on the platforms between stations, the speed of movement on the platforms taking into account the load on the branch, as well as the required time for the train to be in the main operating modes – starting, moving at nominal speed, coasting, braking and stopping [110].

The main calculated values required for performing traction-energy calculations are the motor power on the shaft, the traction force on the wheel rim when starting off, the continuous traction force on the stretches, as well as the value of the maximum traction force, taking into account the adhesion limitation.

The force in the gear mesh and the vertical reaction in the gear bearings can be calculated based on the transmission geometry (see Fig. 3.2):

$$P_1 = \frac{D_w F}{D_{gw}}, \tag{3.1}$$

where D_w is the diameter of the wheel band around the riding circle; and D_{gw} is the diameter of the large gear wheel at the base circle.

The longitudinal forces in the gearbox suspension yoke are determined as:

$$P = \frac{P_1}{\cos \alpha}, \tag{3.2}$$

where: $\alpha = 15°$, $\cos \alpha = 0.966$.

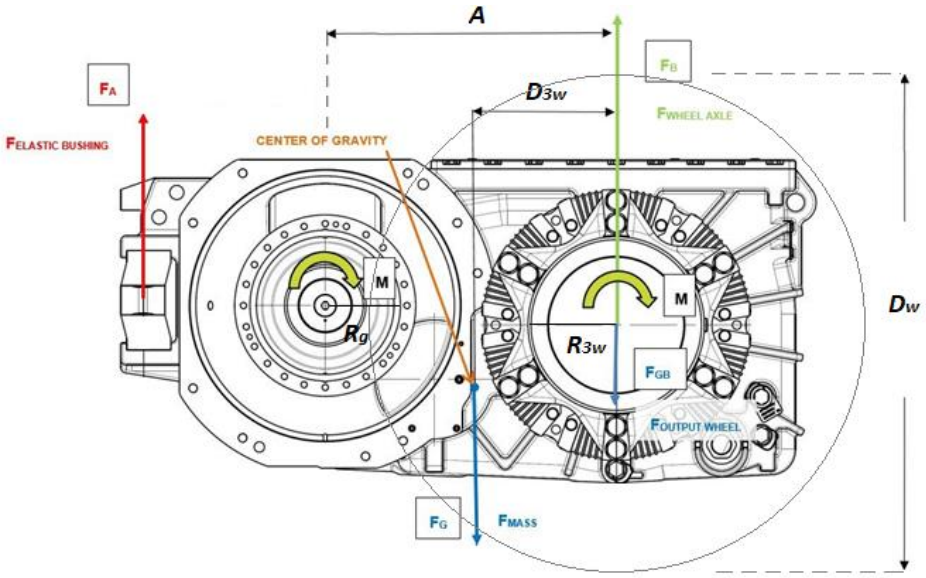

Fig. 3.2. Geometric dimensions of the traction drive.

When a wheel pair passes an uneven rail track, it moves vertically by an amount Z_k with an acceleration $\ddot{Z}_k$. The large pinion of the gearbox moves together with it. The center of the gearbox, point A, rotates by the angle φ (see Fig. 3.3) [110]. If the pair of wheels maintains adhesion to the rail, the rotor of the traction motor must rotate by the angle $\Psi = (i + 1)\varphi$. The angular acceleration of the center of the toothed wheel relative to the center of the pinion is equal to $\ddot{\varphi} = \frac{\ddot{Z}_k}{A}$.

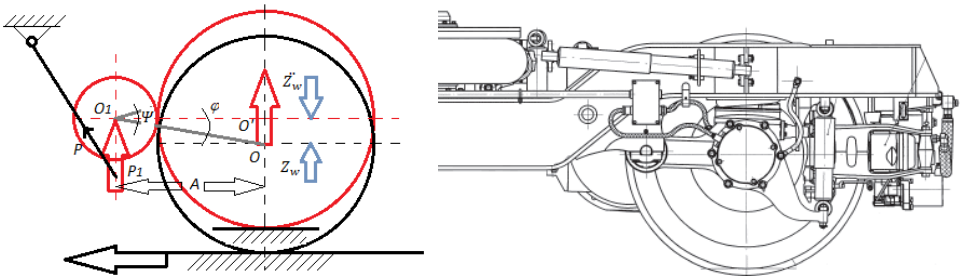

Fig. 3.3. Diagram of the wheelset passing a track irregularity.

The angular acceleration of the traction motor rotor will be equal to:

$$\Psi = (i+1)\ddot{\varphi} = (i+1)\frac{\ddot{Z}_k}{A}. \tag{3.3}$$

Based on the moment theorem [111]:

$$\sum ME = I_r \ddot{\Psi}, \tag{3.4}$$

where: $\sum ME$ – sum of external moments relative to the traction motor rotor axis;

I_r – moment of inertia of the rotor, including the coupling and the pinion.

In this context, the moment is expressed as:

$$\sum ME = P_1 r_g, \tag{3.5}$$

where: P_1 – force acting in the gear engagement;

r_g – radius of the initial circle of the small gear.

Substituting the expression of the external moments $\sum ME$ into the equation (3.4), we get:

$$P_1 = I_r \frac{(i+1)\ddot{Z}_k}{A r_g}. \tag{3.6}$$

The force exerted on the gearbox suspension due to traversing a track irregularity, caused by the angular acceleration of the traction motor's rotor is calculated as:

$$P = \frac{P_1}{\cos\alpha} = \frac{I_r(i+1)\ddot{Z}_k}{A r_g \cos\alpha}. \tag{3.7}$$

To estimate the magnitude of these dynamic forces due to rotor rotation, it's essential to determine the vertical acceleration Z_k at point O which is at the center of the large gear.

While passing over a joint, the gearbox housing undergoes translational motion with an acceleration $\ddot{Z}_c$ at the center of gravity and rotates around the center of gravity with an angular acceleration $\ddot{\varphi}$.

As the wheelset moves over track irregularities (see Fig. 3.4), point O of the gearbox, along with the wheelset, experiences vertical acceleration $\ddot{Z}_k$. In this case, the acceleration of the center of gravity is determined as [111]:

$$\ddot{Z}_c = \frac{\ddot{Z}_k a_c}{A}. \tag{3.8}$$

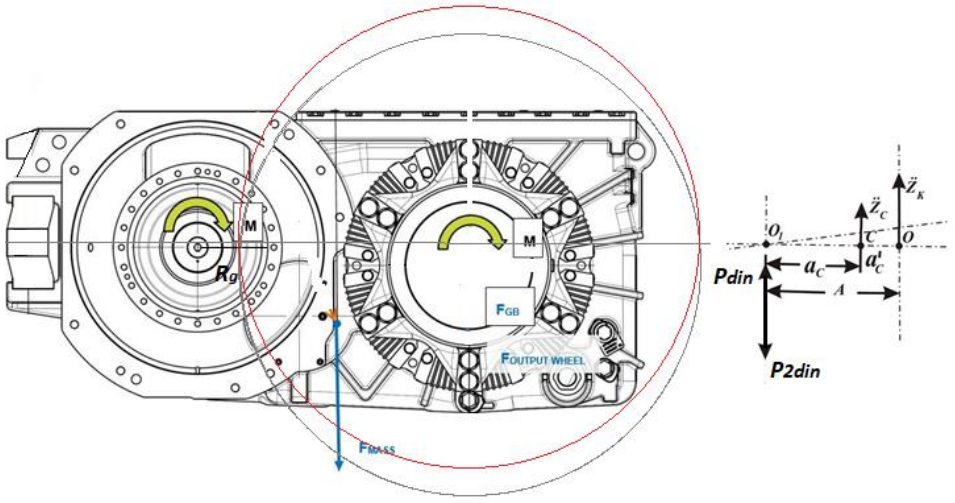

Fig. 3.4. Schematic of the forces affecting the traction gearbox when passing track irregularities.

The inertia force of the gearbox housing generates an additional load on the gearbox suspension, calculated as:

$$P_{1din} = \frac{M_k \ddot{Z}_c (A - a_c)}{A} = \frac{M_k \ddot{Z}_k a_c (A - a_c)}{A^2} = \frac{M_k \ddot{Z}_k a_c a_c'}{A^2}, \quad (3.9)$$

where: M_k – mass of the gearbox housing, including the pinion and half-coupling.

The rotational acceleration of the gearbox casing $\ddot{\varphi} = \frac{\ddot{Z}_k}{A}$ due to inertia reduces the load on the suspension by the amount:

$$P_{din} = \frac{I_c \ddot{\varphi}}{A} = \frac{I_c \ddot{Z}_k}{A^2}, \quad (3.10)$$

where: I_c – moment of inertia of the gearbox casing, inclusive of the pinion and half–coupling, relative to its center of mass.

The overall increase in suspension loads due to inertial forces acting on the gearbox housing when crossing track irregularities is given by:

$$P_{din} = \frac{P_{1din} - P_{2din}}{\cos \alpha} = \frac{M_k \ddot{Z}_k a_c a_c'}{A^2 \cos \alpha} - \frac{I_c \ddot{Z}_k}{A^2 \cos \alpha} = \frac{\ddot{Z}_k}{A^2 \cos \alpha} (M_k a_c a_c' - I_c). \quad (3.11)$$

Thus, it can be assumed that the point of action is at O_1 and the influence of the inertia forces of the gearbox can be disregarded.

The dynamic forces acting on the gearbox suspension during vertical bogie oscillations include galloping, bouncing, and lateral swaying.

The suspension design ensures that point O_1 moves vertically during bogie vibrations as if it were rigidly connected to the bogie frame.

3.3. Impact of Gear Wear on the Longevity of the Traction Drive

Since the dynamic forces within the gearbox, which are conveyed to the wheel-rail contact, generally do not surpass the traction forces, the wheelset can be assumed to be stationary as a first approximation [111]. A simplified mechanical model of the drive system is proposed, which is represented by a system of differential equations with three degrees of freedom: torsional oscillations of the motor in the suspended state, the rotor of the motor on the shaft, and the motor itself in the suspended state, along with the tailshaft of the rotor and gear mounted on the rotor's tailshaft. The equations governing the system are:

$$\left[m_{m.eq} + \frac{I_r}{r_g^2}\right] \ddot{z}(t) + C_f \dot{z}(t) + s_s z(t) = [\ddot{\varphi}_v(t) - \ddot{\varphi}_r(t)] m_{m.eq} r_g. \quad (3.12)$$

$$I_r \ddot{\varphi}_r(t) + C_{1\varphi} \dot{\varphi}_r(t) + s_{1\varphi} \varphi_r(t) = \left[\varphi_v(t) - \frac{z(t)}{r_g}\right] s_{1\varphi} + [\dot{\varphi}_v(t) - \frac{\dot{z}(t)}{r_g}] C_{1\varphi}. \quad (3.13)$$

$$m_{m.eq} \ddot{z^*}(t) + \left(C_f + C_{1n}\right) \dot{z^*}(t) + (s_s + s_{1n}) z^*(t) = \\ = \left[\varphi_v(t) - \varphi_g(t)\right] r_g s_{1n} + [\dot{\varphi}_v(t) - \dot{\varphi}_g(t)] r_g C_{1n}. \quad (3.14)$$

$$I_g \ddot{\varphi}_g(t) + C_{1\varphi}^* \dot{\varphi}_g(t) + s_{1\varphi} \varphi_g(t) = \left[\ddot{\varphi}_v(t) - \frac{\ddot{z}(t)}{r_g}\right] I_g. \quad (3.15)$$

where: $m_{m.eq}$ – equivalent mass of the motor relative to the coordinate z;

- I_r, I_g – moments of inertia of the motor rotor and the gearbox's driving gear, respectively;
- r_g – radius of the pitch circle of the driving gear;
- $C_{1\varphi}$, $C_{1\varphi}^*$, C_{1n}, $C_{m.eq}$ – linearized friction coefficients in the elastic connections;
- s_s – stiffness coefficient in the suspended state relative to the coordinate z;

- $\varphi_r(t)$, $\varphi_g(t)$ – angular oscillations of the motor rotor and the gear on the rotor's tailshaft;
- $z^*(t)$, $z(t)$ – vertical displacements of the traction motor in the suspended state and the rotor's tailshaft only in the suspended state.

Given the narrowband characteristic of the process, the first and second derivatives of $\varphi_v(t)$, can be defined as:

$$\dot{\varphi}_v(t) = -2\pi f \varphi_v(t). \tag{3.16}$$

$$\ddot{\varphi}_v(t) = -(2\pi f)^2 \varphi_v(t). \tag{3.17}$$

The set of equations (3.12) – (3.15) can be efficiently solved using approximation methods, which provide acceptable accuracy due to the substantial difference in natural frequencies between the motor rotor and gear vibrations [111]. For a narrow frequency range that includes frequency f_1 the following approximate equality is valid:

$$I_r \ddot{\varphi}_r(t) = r_g[m_{m.eq}\ddot{z}(t) + C_f \dot{z}(t) + s_s z(t)]. \tag{3.18}$$

By substituting $\varphi_r(t)$ from equation (3.18) into equation (3.12) and solving for $z(t)$, gives an approximate formula for the oscillation amplitude near frequency f_1:

$$z(t) = \frac{4\pi^2 f^2}{s_s(1+\frac{m_{m.eq} r_g^2}{I_r})} \times \frac{m_{m.eq} r_g \varphi_v(t)}{\sqrt{\left[1-(\frac{f}{f_1})^2\right]^2 + (2\xi_1 \frac{f}{f_1})^2}}. \tag{3.19}$$

$$f_1 = \frac{1}{2\pi}\sqrt{\frac{s_s}{m_{m.eq}+\frac{I_N}{r_g^2}}}. \tag{3.20}$$

$$\xi_1 = \frac{C_f}{2\sqrt{s_s(m_{m.eq}+\frac{I_R}{r_g^2})}}. \tag{3.21}$$

To solve equation (3.13) similarly to the previous case, we derive the equation for the oscillation frequency f_2:

$$I_r \ddot{\varphi}_r(t) + C_{1\varphi}\dot{\varphi}_r(t) + s_{1\varphi}\varphi_r(t) = r_g[m_{m.eq}\ddot{z}(t) + C_f \dot{z}(t) + s_s z(t)], \tag{3.22}$$

from which:

$$\frac{z(t)}{r_g} = \frac{1}{k r_g^2}[m_{m.eq}\ddot{z}(t) + C_f \dot{z}(t) + s_s z(t)], \tag{3.23}$$

where:

$$k = \sqrt{(s_{1\varphi} - 4\pi^2 f^2 m_{m.eq})^2 + (2\pi f C_{1\varphi})^2}. \tag{3.24}$$

By substituting $\frac{z(t)}{r_g}$ into equation (3.12) and solving it with respect to $\varphi_r(t)$ can be expressed as follows:

$$\varphi_r(t) = \frac{\varphi_v(t)}{1+\frac{s_{1\varphi}+2\pi f C_{1\varphi}}{k r_g^2}} \times \frac{\sqrt{1+(2\xi_1 \frac{f}{f_2})^2}}{\sqrt{\left[1-(\frac{f}{f_2})^2\right]^2 + (2\xi_1 \frac{f}{f_2})^2}}. \tag{3.25}$$

where:

$$f_2 = \frac{1}{2\pi}\sqrt{\frac{s_{1\varphi}}{I_r}}. \tag{3.26}$$

$$\xi_2 = \frac{C_{1\varphi}}{2\sqrt{s_{1\varphi} I_r}}. \tag{3.27}$$

Similarly, the frequency values for expressions (3.14) and (3.15) were calculated.

Having calculated $z(t)$, $\varphi_r(t)$, $z^*(t)$, and $\varphi_g(t)$, the amplitude of the dynamic torque on the rotor tailshaft M_D was found near the oscillation frequencies f_1, f_2, f_3, f_4 using the following expressions:

$$M_D = z(t)\, s_s r_g. \tag{3.28}$$

$$M_D = \varphi_r(t)\, s_{1\varphi}. \tag{3.29}$$

$$M_D = z^*(t)\, s_{1n} r_g. \tag{3.30}$$

$$M_D = \varphi_g(t)\, s_{1\varphi}. \tag{3.31}$$

The magnitude of M_D also allows for the calculation of the motor housing's acceleration amplitude relative to the rotor using the formula [111]:

$$\ddot{z}_E = M_D / r_g m_{m.eq}. \tag{3.32}$$

It's important to note that at high oscillation frequencies, the dynamic load on the gear teeth exceeds the value calculated by M_D. In such cases, the dynamic load on the gear tooth, accounting for its moment of inertia, can be calculated as:

$$P_Z = \frac{M_D + 4\pi^2 f^2 \varphi_g(t) I_g}{r_g \cos\alpha}. \tag{3.33}$$

When a new gear is paired with a worn gear wheel, the load is approximately double as high compared to a run–in gear pair.

3.4. Vibration Protection and Acoustic Dynamics of Machines

In practical calculations, a simplified dynamic model of torsional and rotational vibrations is commonly used for machinery. This model simplifies the complex multi–mass structure, which consists of distributed masses along with elastic and inelastic resistances, into a limited number of discrete masses. These masses are interconnected by linear or non-linear, massless, elastic-damping elements. After discretizing the system, it is often necessary to reduce the model to a single equivalent shaft, especially for shafts and rotors that rotate at different angular velocities, such as those connected via gearboxes or other mechanical transmissions, and for parts of the system that experience non–torsional vibrations.

When bringing masses into equivalence, the kinetic energy of the equivalent link and the equivalent masses is ensured to be equal. Similarly, when calculating stiffness coefficients and inelastic resistances, the potential energy of the equivalent elastic or inelastic connection and the equivalent connections is ensured to be equal. For the forces and moments of forces, the power of the equivalent moment of forces and the equivalent forces and moments of forces is maintained as equal [112].

The equivalent moments of inertia of masses, along with the coefficients of elastic and inelastic resistances, are determined using the following formulas:

$$\Theta_{eq} = \sum_{i=1}^{n} \Theta_i (\omega_i/\omega_{eq})^2; \frac{1}{C_{eq}} = \sum_{i=1}^{n} \frac{1}{C_i(\omega_i/\omega_{eq})^2}; \frac{1}{b_{eq}} = \sum_{i=1}^{n} \frac{1}{b_i(\omega_i/\omega_{eq})^2}, \tag{3.34}$$

where: Θ_i; C_i; b_i – moment of inertia of masses, stiffness coefficients, and inelastic resistance coefficients of the $i-th$ component in the transmission mechanism;

ω_i; ω_{eq} – angular velocities of the $i-th$ component and the equivalent component;

n – total number of elements within the transmission system.

The moments of driving and resistance forces are determined by:

$$M_{mr} = \sum_{i=1}^{n} M_i \omega_i / \omega_{mr}, \tag{3.35}$$

where: M_i – moment of force applied to the $i-th$ component.

During steady-state machine operation, the forces and the equivalent moments of resistance exhibit periodic behavior over time:

$$M_1(t) = M_1(t + kT), \tag{3.36}$$

where: T – cycle period, k – an integer.

The moment of resistance forces, as a periodic function of time, can be represented as a trigonometric series with an infinite number of terms. Limiting to n terms of the series, we get:

$$M_1(t) = M_r + \sum_{i=1}^{n}(M_{1i}\, cos\, i\omega t + M_{2i}\, sin\, i\omega t), \tag{3.37}$$

or

$$M_1(t) = M_r + \sum_{i=1}^{n}(M_{ai}\, cos(i\omega t + \beta_i), \tag{3.38}$$

where: M_r – constant component of the moment of resistance forces;

M_{ai} – amplitude of the $i-th$ harmonic component of the moment.

$$M_{ai} = \sqrt{{M_{1i}}^2 + {M_{2i}}^2}, \tag{3.39}$$

where: M_{1i} and M_{2i} – harmonic coefficients for the cosine and sine components (3.37);

β_i – initial phase angle of the $i-th$ harmonic component of the moment, defined as $\tan\beta_i = M_{2i}/M_{1i}$.

The torque produced by the motor depends on its rotational speed [112]. For a DC motor with independent and parallel excitation, the torque, the torque can be expressed as:

$$M_m = M_{cm} - b_r\omega, \tag{3.40}$$

where: M_{cm} – constant component of the motor torque;

b_r – coefficient that represents the reduction in torque as rotational speed increases ω.

For an asynchronous motor, the mechanical characteristic is described by the following differential equation:

$$S_1 = \upsilon(M_{dm} + T_e\frac{dM_{dm}}{dt}), \tag{3.41}$$

where: S_1 – rotor slip of the motor,

T_e – electromagnetic time constant, calculated as $T_e = 1/\omega_{eq}S_k$, where ω_e – electrical network's angular frequency.

$$S_1 = \frac{\omega_{c1} - \frac{d\varphi_1}{dt}}{\omega_{c1}}. \tag{3.42}$$

where: ω_{c1} – synchronous rotational speed of the motor;

M_m – torque developed by the motor;

υ – value that characterizes the stiffness of the motor characteristic in the static mode.

$$\upsilon = S_{cr}/(2M_{cr}), \tag{3.43}$$

where: M_{cr} – critical motor torque in the static mode;

S_{cr} – critical slip, calculated as $S_{cr} = S_N(\lambda + \sqrt{\lambda^2 - 1})$, S_N – slip at nominal rotational speed ω_N and nominal torque M_N of the motor;

λ – ratio of the critical and nominal torques.

3.5. Torsional-Rotational Vibrations in Single-Mass and Two-Mass Systems

For the purpose of analyzing torsional and rotational vibrations, most machine assemblies can be simplified into a two-mass model. In this model, the concentrated masses typically

represent the rotor masses of the machine – specifically, the rotor of the motor and the rotor of the driven machine [112]. The masses of the transmission elements are reduced to these concentrated masses.

The differential equations that describe the vibrations of this system are:

$$\theta_1\ddot{\varphi}_1 + b_\varphi(\dot{\varphi}_1 - \dot{\varphi}_2) + C_\varphi(\varphi_1 - \varphi_2) = M_1(\omega); \quad (3.44)$$

$$\theta_2\ddot{\varphi}_2 + b_\varphi(\dot{\varphi}_2 - \dot{\varphi}_1) + C_\varphi(\varphi_2 - \varphi_1) = M_2(t), \quad (3.45)$$

where: θ_1 and θ_2 – moments of inertia associated with the rotors of the electric motor and the working machine, respectively;

C_φ and b_φ – equivalent stiffness and damping coefficients of the transmission system;

$M_1(\omega)$ – torque produced by the motor, which depends on its rotational speed;

$M_2(t)$ – torque due to resistance forces, which is a function of time.

The solutions to these equations (3.44) and (3.45) can be expressed as $\varphi_1 = \varphi_{11}\cos\omega t + \varphi_{12}\sin\omega t$ and $\varphi_1 = \varphi_{21}\cos\omega t + \varphi_{22}\sin\omega t$.

The amplitudes of the angular displacements for masses θ_1 and θ_2 are calculated by:

$$\varphi_{1a} = \sqrt{\varphi_{11}^2 + \varphi_{12}^2};\ \varphi_{2a} = \sqrt{\varphi_{21}^2 + \varphi_{22}^2}. \quad (3.46)$$

However, when analyzing transmission mechanisms, it's often more crucial to determine the amplitudes and phases of the relative rotational vibrations between the masses θ_1 and θ_2.

To simplify the equations, divide equation (3.44) by θ_1, and equation (3.45) by θ_2. Subtracting the second equation from the first and defining the relative angular displacement as:

$$\varphi_{12} = \varphi_1 - \varphi_2. \quad (3.47)$$

This reduction simplifies the system of equations (3.44) and (3.45) into a single differential equation that describes the relative rotational oscillations between the two masses: θ_1 and θ_2 [112].

$$\ddot{\varphi}_{12} + \frac{\text{в}_\varphi}{\theta_{eq}}\dot{\varphi}_{12} + \frac{C_\varphi}{\theta_{eq}}\varphi_{12} = m_1(\omega) - m_2(t), \quad (3.48)$$

where: θ_{eq} – equivalent moment of inertia of the masses, is given by:

$$\theta_{eq} = \frac{\theta_1\theta_2}{\theta_1+\theta_2};\ m_1(\omega) = \frac{M_1(\omega)}{\theta_1};\ m_1(\omega) = \frac{M_2(t)}{\theta_2}. \quad (3.49)$$

Assuming that $\frac{b_\varphi}{\theta_{eq}} = 2\varepsilon_\varphi$; $\frac{C_\varphi}{\theta_{eq}} = \omega_{0\varphi}^2$ where ε_φ and $\omega_{0\varphi}$ – damping coefficient and the natural frequency of the rotational oscillations of the masses.

In free vibration scenarios within a two-mass system, the masses rotate in opposite directions by angles inversely proportional to their moments of inertia: $\varphi_1/\varphi_2 = \theta_2/\theta_1$.

3.6. Torsional-Rotational Oscillations in Drives with Asynchronous AC Motors

Asynchronous motors are implemented in systems where the drive can be modeled as a two-mass structure. These systems are described by the following differential equations:

$$\theta_1\ddot{\varphi}_1 = M_m + M_{21};\ \theta_2\ddot{\varphi}_2 = M_{21} - M_{2R}, \quad (3.50)$$

where: θ_1, θ_2 – moments of inertia referred to the motor rotor and the rotor of the driven system;

φ_1, φ_2 – generalized coordinates (rotational angles of the motor and unit rotors);

M_{2R} – torque of the resistance forces reduced to the rotor of the unit;

$M_{21};\ M_{12}$ – torques acting on the motor rotor and the unit rotor through the transmission.

The transmission characteristics are expressed as:

$$M_{21} = C_{12}(\varphi_1 - u_{12}\varphi_2) - b_{12}(\dot{\varphi}_1 - u_{12}\dot{\varphi}_2), \tag{3.51}$$

$$M_{12} = C_{12}(\varphi_1 - u_{12}\varphi_2)u_{12} + b_{12}(\dot{\varphi}_1 - u_{12}\dot{\varphi}_2)u_{12}, \tag{3.52}$$

where: C_{12}; b_{12} – stiffness and damping constants of the transmission mechanisms;

$u_{12} = \frac{\omega_{1S}}{\omega_{2S}}$ – transmission ratio;

ω_{1S} – synchronous angular speed of the motor rotor;

ω_{2S} – ideal angular speed of the unit rotor.

The resistance forces M_{2R} can be represented by a trigonometric series:

$$M_{2R} = \sum_{i=1}^{k}({M_{2ai}}^{(1)} \cos i\omega_{20}t + {M_{2ai}}^{(2)} \sin i\omega_{20}t), \tag{3.53}$$

where: ${M_{2ai}}^{(1,2)}$ – amplitude coefficients of the resistance torque.

The mechanical characteristic of the motor is expressed by equation (3.41). By introducing relative parameters for the angular speeds of the motor and unit rotors S_1 and S_2, defined as:

$$S_1 = (\tfrac{\omega_{1S}-\omega_1}{\omega_{1N}});\ S_2 = (\tfrac{\omega_{2S}-\omega_2}{\omega_{2N}}), \tag{3.54}$$

The equations (3.50) can be rewritten as:

$$\theta_1 \nu T_e \frac{d^2M_m}{dt} + (b_{12}\nu T_e + \theta_1 \nu)\frac{dM_m}{dt} + \\ + \left(b_{12}\nu + C_{12}\nu T_e + \frac{1}{\omega_{1S}}\right)M_m + C_{12}\nu \int M_m\, dt = C_{12}\int S_2 dt; \tag{3.55}$$

$$\theta_2 \frac{dS_2}{dt} + (b_2 + b_{12}{u_{12}}^2)S_2 + C_{12}{u_{12}}^2 \int S_2 dt = b_{12}{u_{12}}^2 \nu T_e \frac{dM_m}{dt} + \\ + (b_{12}{u_{12}}^2 \nu + C_{12}{u_{12}}^2 \nu T_e)M_m + \\ + C_{12}{u_{12}}^2 \nu \int M_m\, dt + \sum_{i=1}^{k}(m_{2ai} \cos i\omega_{20}t + m_{2ai} \sin i\omega_{20}t), \tag{3.56}$$

where: $m_{2ai} = \frac{M_{2ai}}{\omega_{2S}}$.

The solution to the equations (3.55) and (3.56) is assumed to be in the form:

$$M_m = M_m \cos\omega t + M_m \sin\omega t; \tag{3.57}$$

$$S_2 = S_{21}\cos\omega t + S_{22}\sin\omega t. \tag{3.58}$$

Substituting the solutions (3.57) and (3.58) into the system of integro-differential equations, the harmonic coefficients M_{m1}; M_{m2}; S_{21}; S_{21}, from which the solutions are derived as:

$$M_m = M_{ma}\cos(\omega t + \beta_M);\ S_2 = S_{2a}\cos(\omega t + \beta_{S2}), \tag{3.59}$$

where: M_{ma}; S_{2a} — amplitudes of the variable components of the motor torque and slip; β_M, β_{S_2} — phase shift angles.

Using the relation (3.54), the amplitudes of the angular speed of the mass are found as:

$$\omega_{2a} = \omega_{2S}(1 - S_{2a}). \tag{3.60}$$

3.7. Operation of the Gearbox as Part of the Traction Drive

The most common and reliable scheme of electric power supply of the motor car of the suburban electric train is shown in Fig. 3.5. Depending on the region of use and passenger flow, as well as on the length of the platform and the accompanying infrastructure, suburban trains can be pumped from 4 to 12 cars, the number of motor cars is selected at the design stage, during operation, some of them can be in reserve as a trailer car. As shown in Fig. 3.6. the motor car contains two bogies, each of which contains two MGUs, M1, M2, M3 and M4. Each bogie

is powered by its inverter, the inverters are located in a single housing, together with the pre-charge device and the input filter. Between the power supply network and the converter, an electromagnetic interference filter L1 and a main disconnector QF1 are installed [113].

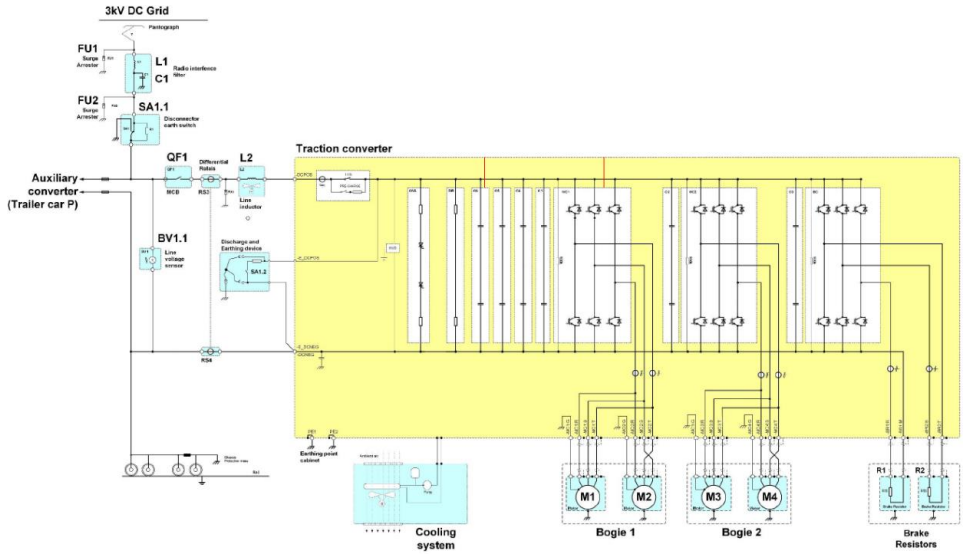

Fig. 3.5. Electrical diagram of the power equipment of a motor car.

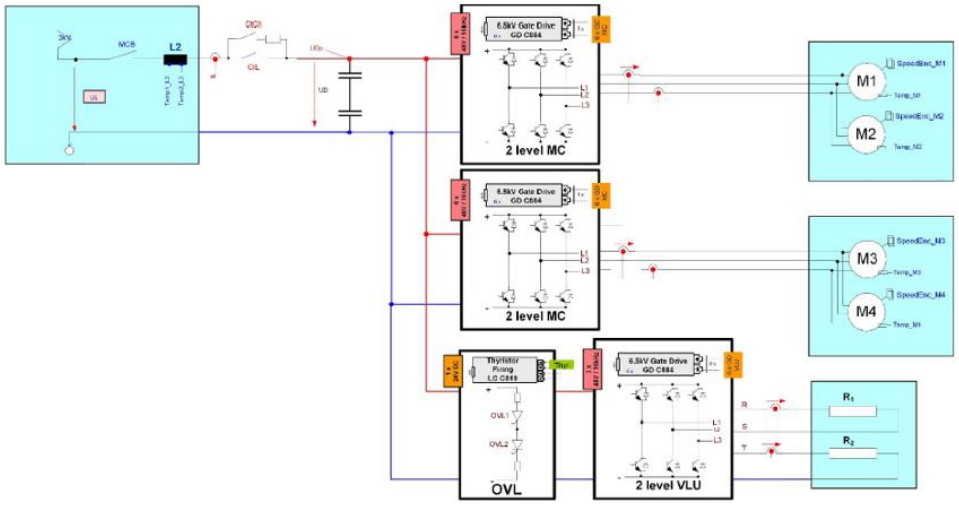

Fig. 3.6. Connection diagram for motorized bogies with MGU M1, M2, M3 and M4 to inverters and brake resistor units R1 and R2 to the chopper [113].

For prototyping and reproducing the operation of the power unit in the laboratory software for the purpose of further testing of the manufactured units of equipment, a model of the input was created in the MATLAB Simulink software, Fig. 3.7. This method of constructing a test bench implies alternate mutual loading of two MGUs according to the principle of "mutual loading of a two-machine “motor-generator” system" with control from a traction converter and

a rheostat-brake unit. The function of the motor and generator is performed by the motors equipped with gear units. The output shafts of the MGU are rigidly coupled to each other [113].

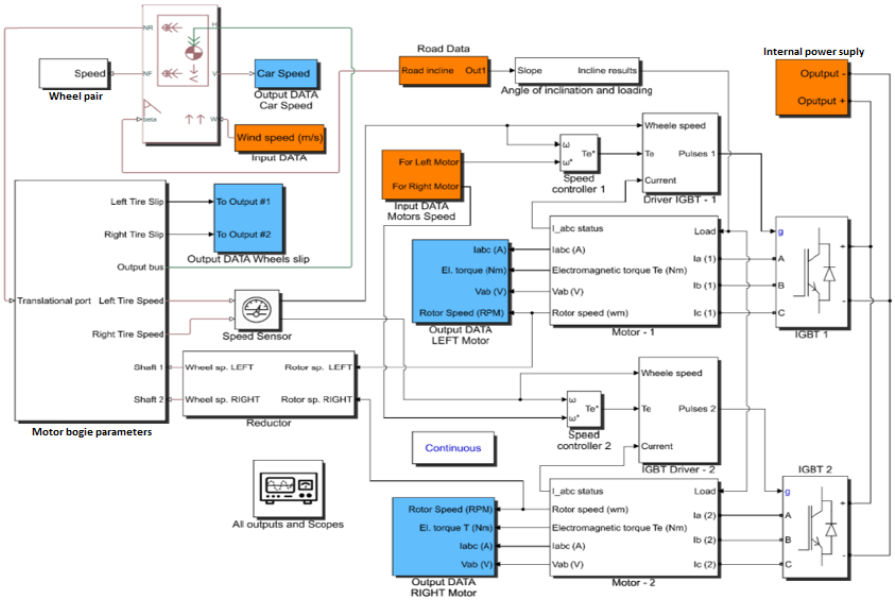

Fig. 3.7. Power unit diagram in MATLAB Simulink.

The speed controller VR, having received the control signal U_{input}, transmits it to the current controller IR through the current limitation and cutoff unit IMAX. The voltage controller UR receives the reference signal from IR, and the output signal is fed to the IGBT inverter. The same IGBT inverter supplies the loaded motor. The loading motor in turn has feedback on the EMF (presented in Figs. 3.8, 3.9 and 3.10). The operation of this scheme is described in detail in the author's publications [114], [115], [116] and [117].

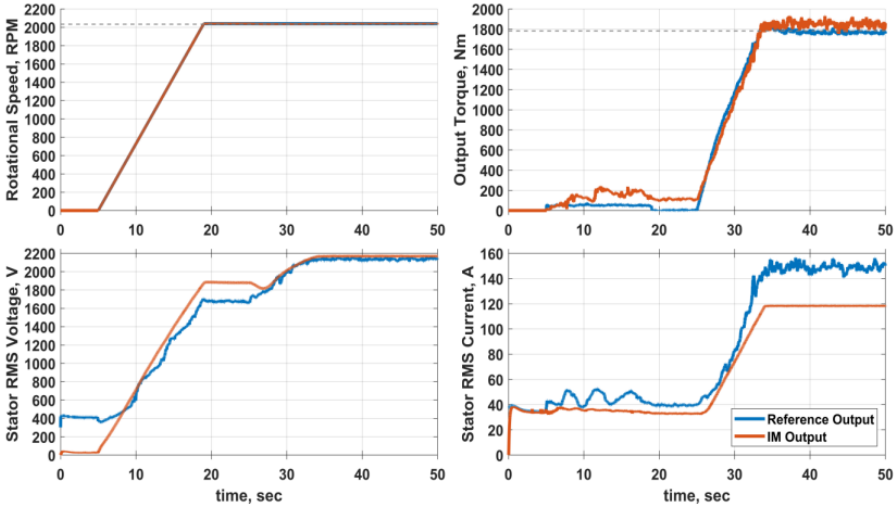

Fig. 3.8. Characteristics of the MGU during the transient process upon reaching the nominal load.

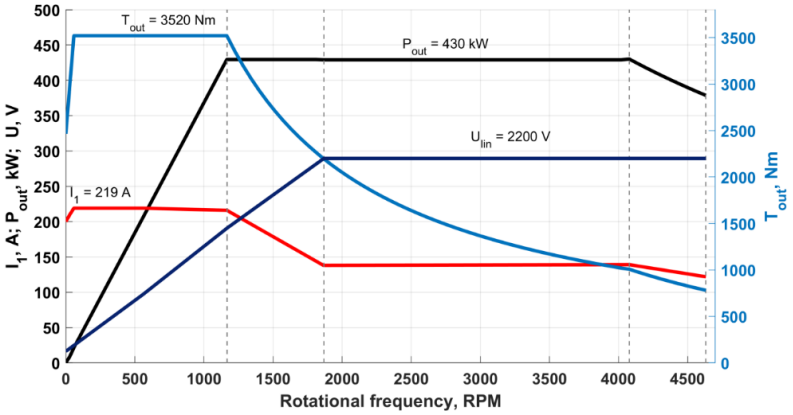

Fig. 3.9. Traction diagram of EMU.

Based on the traction drive loading cyclogram, it is possible to imagine the interrelationship between the operation of the MGU units. Since the primary operational modes of the motor bogie drive are acceleration and deceleration, investigations into the loadings on the components of the thrust gear were conducted under these conditions. In the simulation, it was assumed that there are no clearances within the mechanism, the stiffness $c_{12} \gg c_{23}$, and the first two masses are practically a single whole, as depicted in Fig. 3.11.

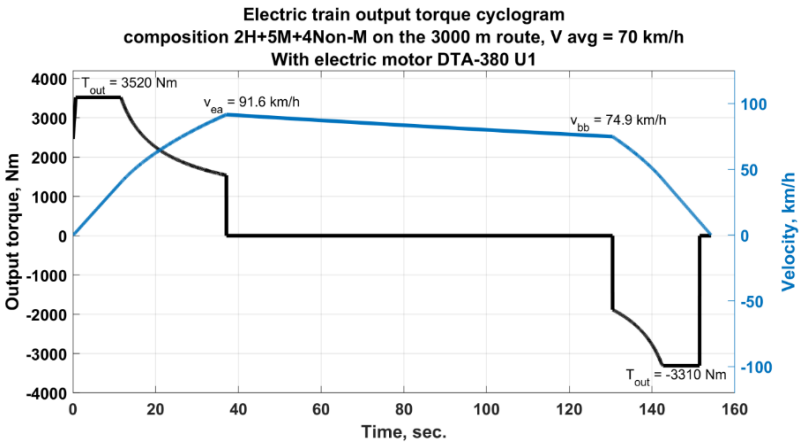

Fig. 3.10. Output torque cyclogram of EMU.

The evaluation of the loads on the gearbox components was based on the following indicators:

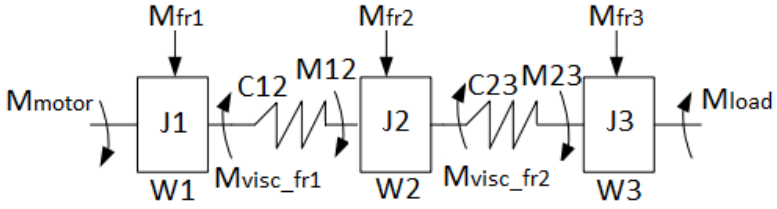

Fig. 3.11. Calculation scheme of traction gear.

$-M_{dmax} = max|(t)|$, which reflects represents the maximum dynamic torque;

$-\int M_d \frac{1}{T}\int_0^T |M_d(t)|dt$, which indicates the duration of its effect.

For passenger electric trains with a maximum speed of 120-160 km/h, the ratio of the maximum speed to the nominal speed is usually 1.4-1.6. Due to the significant influence of the aerodynamic drag of the train on the total resistance to movement for passenger electric locomotives and electric trains, it is desirable to maintain the rated power in the speed range.

For this reason, it will be necessary to develop maximum power at maximum speed. Naturally, the traction force must be maintained at its greatest both during acceleration and at maximum speed.

The power of the electric brake does not exceed the power of the traction mode, therefore the curves of power and braking forces are usually close to the corresponding curves of the traction mode.

For most types of EMU, it is advisable to combine the nominal voltage U_{1nom} with the nominal speed of movement, assuming that it will remain unchanged in the speed range. Sometimes it may be advisable to slightly increase the voltage in the speed range.

To ensure the greatest and constant traction force in the acceleration zone, the highest phase current will be required, also unchanged in value. These considerations, given the nature of the power change, fully determine the current loads of traction motors [118].

3.8. Calculation of the Strength of the MGU Housing

Taking into account the manufacturing technology of the MGU, it is necessary to highlight that it involves several types of preparation and processing of the materials used, so the motor and gearbox housings are made of steel or high-grade cast iron with subsequent heat treatment and tempering. The stator core is a pressed charge-welded structure. Each element has its own points of concentration of mechanical stresses, usually in places with a sharp change in the cross-section. Stress can also accumulate in places with potholes, chips, and as a result of long-term operation, also in places of wear.

The most applied method that has proven itself in the mechanical engineering industry has become the finite element method (FEM), the possibility of using, which is implemented in all major automatic design systems, not to mention specialized field solvers [119, 120, 121, 122, 123].

To determine the safety margin and identify the most vulnerable places in terms of mechanical stress, the critical state of which can be significantly aggravated under dynamic loads and changing vibration levels, it is necessary to have an idea of the behaviour of the object, in the specific case of the MGU, under stress-strain conditions.

The model uses the following coordinate system:

- tangential force $F_t(N)$: X–axis;
- axial force $F_r(N)$: Y–axis;
- radial force $F_x(N)$: Z–axis.

The structural material is defined as ductile iron grade EN-GJS-350-22-LT with the following strength parameters:

- Modulus of elasticity E = 169 000 MPa;
- Poisson's ratio μ = 0.275;

- Yield strength σ_y = 220 MPa.

Fig. 3.12 shows a mesh model of the MGU from the side of the gearbox bearing shield and from the side of the traction motor bearing shield.

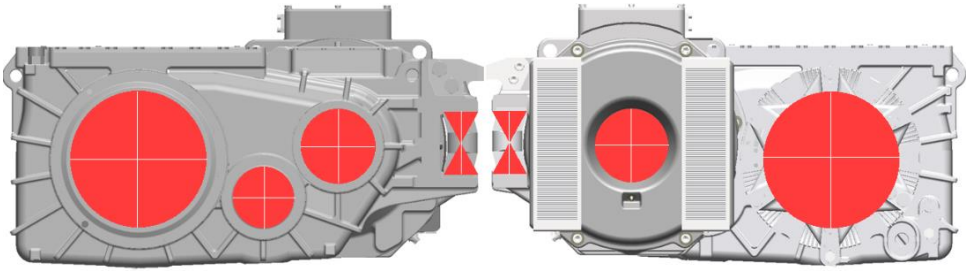

Fig. 3.12. Mesh model of the MGU.

For the most loaded element of the MGU shaft with a gear transmission with the formula *z* = 25 and *m* = 5.5, the values of dynamic loads are presented in Table 3.1.

Table 3.1

Loading characteristics of the input gear shaft (first stage with *z* = 25, *m* = 5.5)

Time		Speed		Traction force on one axle	Torque
s	%	km/hour	rpm	kN	Nm
5	3.36	13	379	37.5	3551
10	3.36	26	757	37.5	3551
15	3.36	40	1165	37.5	3551
20	3.36	53	1544	29.5	2794
25	3.36	62	1806	24.5	2320
30	3.36	72	2097	21.25	2012
35	3.36	78	2272	18.75	1776
40	3.36	85	2476	17.5	1657
45	3.36	92	2680	16.5	1563
50	3.36	98	2855	15.25	1444
52	1.34	100	3168	15	1421
102	33.56	100	3168	1.72	163
104	1.34	98	2855	- 15.25	- 1444
107	2.01	94	2738	- 16	- 1515
112	3.36	87	2534	- 17.25	- 1634
117	3.36	78	2272	- 19.25	- 1823
122	3.36	70	2039	- 21.5	- 2036
127	3.36	60	1748	- 24.75	- 2344
132	3.36	49	1427	- 30.5	- 2888
134	1.34	44	1282	- 33.75	- 3196
137	2.01	36	1049	- 36	- 3409
139	1.34	30	874	- 37.5	- 3551
142	2.01	21	612	- 37.5	- 3551
147	3.36	6	175	- 37.5	- 3551
149	1.34	0	0		

3.8.1. Initial Calculation of Bearing Loads

3.8.1.1. Gear Calculations: First Stage of the Gearbox

In order to verify the appropriateness of the selected bearings, a calculation was performed to assess the accuracy of their choice according to DIN 3990:1987 standards. The input parameters for the calculations of both the first and second stages are presented in Table 3.2 and Fig. 3.13 and Fig. 3.14.

Table 3.2

Input data for the first stage of the gearbox

PARAMETER	SYMBOL	GEAR 1	GEAR 2
Center distance (mm)	[a]	230.000	
Center distance tolerance	ISO 286:2010 Measure js7		
Normal module (mm)	[mn]	5.5000	
Pressure angle at normal section (°)	[alfa]	20.0000	
Helix angle at reference circle (°)	[beta]	15.0000	
Number of teeth	[z]	25	56
Facewidth (mm)	[b]	75.00	72.00
Hand of gear		right	left

Material Specifications for Gear 1 and Gear 2:

Both gears are made from 18CrNiMo7–6, a case–carburized and case–hardened steel, compliant with *ISO 6336–5*, with a core hardness of at least 30HRC.

Table 3.3

Results according to DIN 3990:1987 calculation method B

Safety Root:	2.43	2.31
Safety Flank:	1.37	1.37
Safety scuffing (integral)	3.69	
Safety scuffing (Flash)	4.15	

Table 3.4

Confirming with safety factor

Required minimal value of Safety Root:	1.4	Confirmed
Minimal Safety Root:	2.31	
Comfirming with Safety factor	**1.65**	
Required minimal value of Safety Flank	1.0	Confirmed
Minimal Safety Flank	1.37	
Comfirming with Safety factor	**1.37**	
Required minimal value of Safety Scuffing (Integral)	1.8	Confirmed
Minimal Safety Scuffing (Integral)	3.69	
Confirming with Safety Factor	**2.05**	
Required minimal value of Safety Scuffing (Flash)	2.0	Confirmed
Minimal Safety Scuffing (Flash)	4.15	
Confirming with Safety Factor	**2.75**	

3.8.1.2. Gear Calculations: Second Stage of the Gearbox

To verify the adequacy of the bearings, calculations were conducted to confirm their selection in accordance with DIN 3990:1987. The input data for the calculations of both the first and second stages are outlined in Table 3.5.

Table 3.5

Input data for the second stage of the gearbox

PARAMETER	SYMBOL	GEAR 1	GEAR 2
Center distance (mm)	[a]	316.000	
Center distance tolerance	ISO 286:2010 Measure js7		
Normal module (mm)	[mn]	7.0000	
Pressure angle at normal section (°)	[alfa]	20.0000	
Helix angle at reference circle (°)	[beta]	14.0000	
Number of teeth	[z]	26	61
Facewidth (mm)	[b]	97.00	95.00
Hand of gear		right	left

Material Specifications for Gear 1 and Gear 2:

Both gears are made from 18CrNiMo7–6, a case-carburized and case-hardened steel, compliant with *ISO 6336–5*, with a core hardness of at least 30HRC [124].

Table 3.6

Results according to DIN 3990:1987 Calculation Method B

Safety Root:	2.22	2.09
Safety Flank:	1.39	1.39
Safety scuffing (integral)	4.09	
Safety scuffing (Flash)	5.54	

Table 3.7

Confirming with safety factor

Required minimal value of Safety Root:	1.4	Confirmed
Minimal Safety Root:	2.09	
Comfirming with Safety factor	**1.49**	
Required minimal value of Safety Flank	1.0	Confirmed
Minimal Safety Flank	1.39	
Comfirming with Safety factor	**1.39**	
Required minimal value of Safety Scuffing (Integral)	1.8	Confirmed
Minimal Safety Scuffing (Integral)	4.09	
Confirming with Safety Factor	**2.27**	
Required minimal value of Safety Scuffing (Flash)	2.0	Confirmed
Minimal Safety Scuffing (Flash)	5.54	
Confirming with Safety Factor	**2.77**	

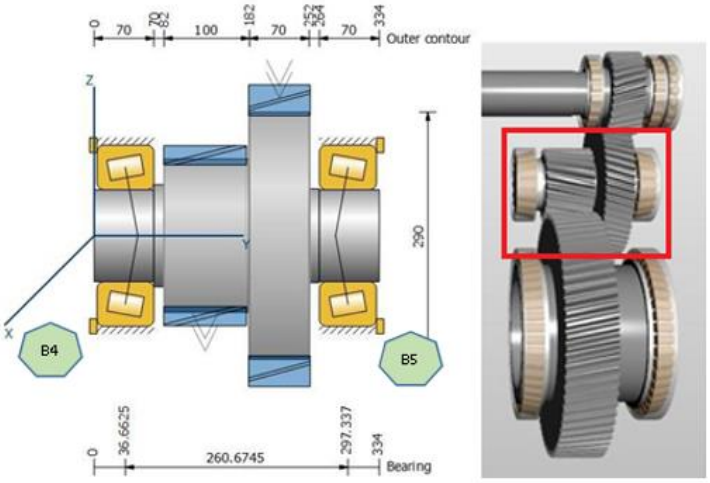

Fig. 3.13. Bearings scheme. Jack shaft.

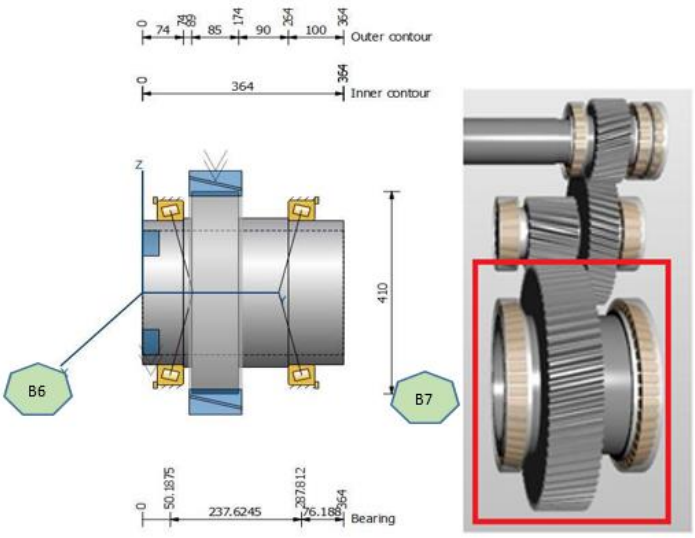

Fig. 3.14. Bearings scheme. Output shaft.

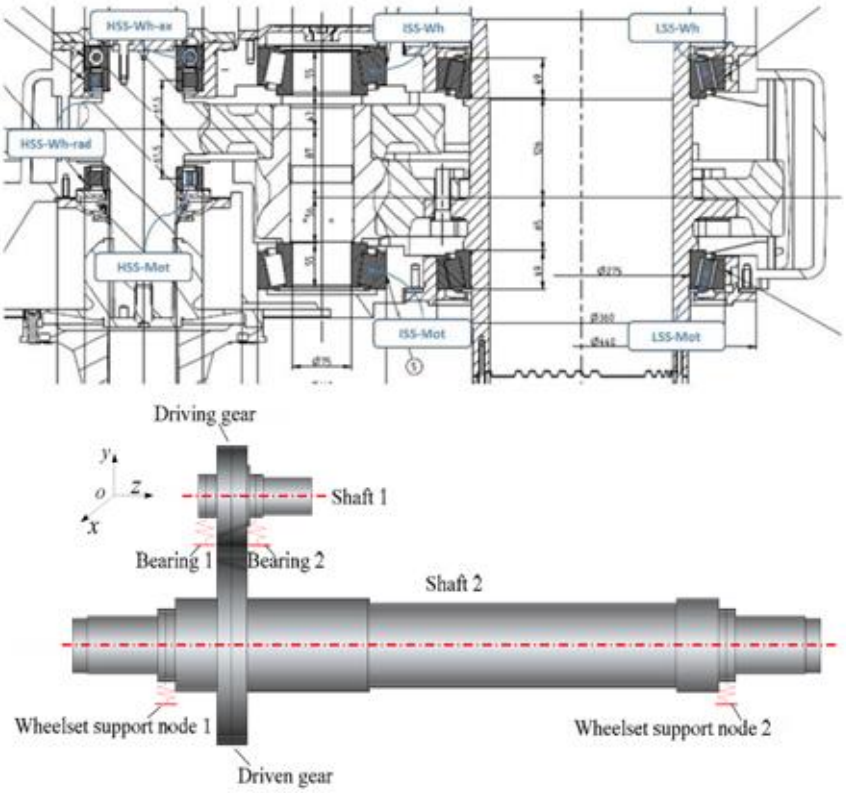

Fig. 3.15. Positions of bearings.

3.8.2. Conditions for Strength Analysis. Data of Shock Loads and Short Circuit Torque

Contact stresses and static safety factor: The Hertzian contact stresses and static safety factors under maximum shock loads are acceptable for this application and given in Table 3.8 and Table 3.9.

Table 3.8

Static calculations for shock loads

Direction of rotation	Labelling	Bearing designation	Static safety		Max. contact stress		Misalignment [min]
			$S_{0,}$ ISO [-]	$S_{0,}$ STD [-]	Inner ring [N/mm^2]	Outer ring [N/mm^2]	
CW	HSS-Mot	NU 217 ECML/C4H	6.07	4.39	1908	1663	4.0
	HSS-Wh-rad	NU 217 ECML/C4H	6.00	4.40	1907	1661	3.5
	HSS-Wh-ax	QJ 217 N2M4/C4H	5.68	4.00	2322	2290	3.4
	ISS-Wh	32315/VE141	7.55	6.02	1630	1303	0.2
	ISS-Wh	32315/VE141	7.71	7.76	1436	1130	1.2
	LSS-Mot	BT1-1125	14.10	10.54	1329	214	0.9
	LSS-Wh	BT1-1125	13.76	10.54	1232	140	0.9

CCW	HSS-Mot	NU 217 ECML/C4H	3.79	3.70	1959	0	3.9
	HSS-Wh-rad	NU 217 ECML/C4H	6.61	4.89	1809	1571	3.5
	HSS-Wh-ax	QJ 217 N2M4/C4H	5.78	4.71	2325	2292	3.5
	ISS-Mot	32315/VE141	10.14	8.60	1364	1094	3.5
	ISS-Wh	32315/VE141	12.85	9.36	1032	1032	0.9
	LSS-Mot	BT1-1125	11.46	8.51	1046	1275	0.9
	LSS-Wh	BT1-1125	21.43	14.92	1035	979	0.9

Table 3.9

Static calculation for short circuit torque

Direction of rotation	Labelling	Bearing designation	Static safety		Max. contact stress		Misalignment [min]
			$S_{0,}$ ISO [-]	$S_{0,}$ STD [-]	Inner ring [N/mm^2]	Outer ring [N/mm^2]	
CW	HSS-Mot	NU 217 ECML/C4H	1.41	1.53	3220	2827	1.5
	HSS-Wh-rad	NU 217 ECML/C4H	1.60	1.71	3057	2682	1.8
	HSS-Wh-ax	QJ 217 N2M4/C4H	4.45	5.01	2454	2426	1.8
	ISS-Wh	32315/VE141	1.04	1.04	3704	3112	5.5
	ISS-Wh	32315/VE141	1.17	1.08	3693	3046	3.0
	LSS-Mot	BT1-1125	3.41	2.12	2366	2165	2.3
	LSS-Wh	BT1-1125	3.57	3.01	2156	1952	2.3
CCW	HSS-Mot	NU 217 ECML/C4H	1.60	1.71	3061	2685	1.8
	HSS-Wh-rad	NU 217 ECML/C4H	1.37	1.42	3284	2885	1.7
	HSS-Wh-ax	QJ 217 N2M4/C4H	4.46	5.03	2451	2424	1.7
	ISS-Mot	32315/VE141	1.39	1.18	3381	2907	0.6
	ISS-Wh	32315/VE141	1.63	1.49	3124	2586	5.1
	LSS-Mot	BT1-1125	2.60	2.39	2312	2112	1.8
	LSS-Wh	BT1-1125	6.24	4.47	1834	1653	1.8

3.8.2.1. Conditions for Strength Analysis. Shrink fit Calculation

For the minimum fit calculation (representing the least torque that can be transmitted), the surface roughness flattening is considered.

For the maximum fit calculation (representing the highest Von Mises stresses), the flattening of surface roughness is not considered.

All computations are carried out in accordance with DIN7190–1:2017–02.

3.8.2.2. Conditions for Strength Analysis. Connection Between Intermediate Shaft and Gear

Maximum short-circuit torque on the shrink–fitted output wheel shaft: 21.3 kNm;

Gearwheel reference bore diameter: 125 H6 (0.025/0,000) mm;

Wheel shaft reference diameter: 125 v6 (0.227/0,202) mm.

Minimum transmittable torque, assuming a friction coefficient of 0.18: 23.2 kNm;
Safety factor for slipping: 1.09 > 1,00;
Maximum Von Mises stresses hub: 330.9 MPa
Safety factor to yield stress: 1.28 > 1.2
Maximum Von Mises stresses shaft: 239.3 MPa
Safety factor to yield stress: 1.78 > 1.2

3.8.2.3. Conditions for Strength Analysis. Output Coupling–axle Connection

Maximum short circuit torque on shrinks output wheel shaft: 72.6 kNm
Gearwheel reference bore diameter: 230 IT6 (– 0.285/– 0.315) mm
Wheel shaft reference diameter: 230 h6(0.000/ – 0.029) mm

Minimum transmittable torque, assuming a friction coefficient of 0.18: 80.6 kNm,
Safety factor for slipping: 1.11 > 1.00
Maximum Von Mises stresses hub: 226.8 MPa
Safety factor to yield stress: 1.85 > 1.2
Maximum Von Mises stresses shaft: 103.0 MPa
Safety factor to yield stress: 3.26 > 1.2

3.9. Structural Strength Calculation of the Gearbox Housing

It is evident from the design of the MGU adopted for the dissertation research that the main load falls on the bearing shield of the traction motor and the support bearing of the gearbox. From the point of view of the requirements for the quality of manufacture and further durability during operation, the bearing seats are one of the most vulnerable points of the MGU design [125, 126]. Any deviations from those required in the drawing lead to unevenness of the air gap between the rotor and the stator of the traction motor, which inevitably entails a change in the energy parameters of the drive - the power factor and the efficiency. Due to the complex geometry of the bearing shields, see Fig. 3.16., providing additional strength to the structure by thickening the wall is not the best solution, due to the increase in the overall dimensions of the MGU [125].

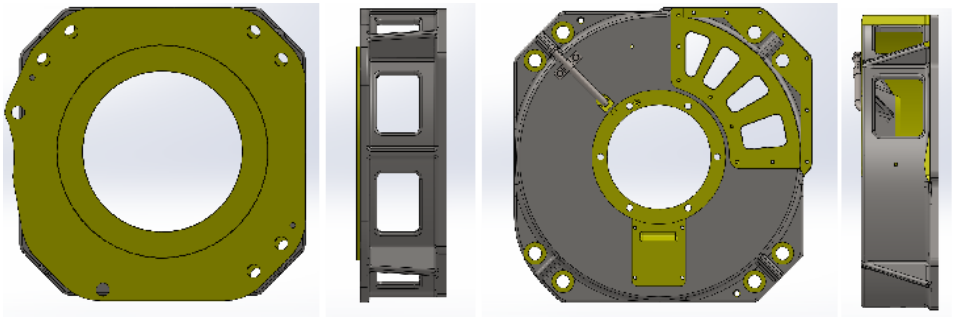

Fig. 3.16. Bearing shields of electric motors.

From the design point of view, special requirements are imposed on the bearing shields:

1. The locking mechanism and the hole for the bearing must be located concentrically, on the same axis.;

2. For flanged bearing shields, the mounting surface (the flange surface connecting the motor to the gearbox) must also be concentric with these surfaces.

A rotating magnetic field is created only if the currents flowing through the stator windings are symmetrical and the air gap between the stator and rotor is symmetrical [126].

The EMF in the coils of each phase is generated when the coils are symmetrically located in space and the phase currents are shifted in time in accordance with the spatial arrangement of the windings.

Typically, wear of the bearing assemblies' results in axial non-uniformity within 90° in both the x- and y-axis [127]. This wear changes the spatial position of the motor rotor, and as the rotor position changes, the shape of the magnetic flux (Φ) changes from cylindrical to elliptical.

If any of these conditions are not met, a non-circular elliptical rotating magnetic field is created. In such a field, the peak value of the resulting magnetic induction (B) at different moments of time (t) does not remain constant, unlike a circular cylindrical magnetic field [125]. In such a field, the spatial vector of the MMF (F_m) or the magnetic induction vector ($\overline{B}_m$) describes an ellipse (Fig. 3.17). This elliptical magnetic field can be divided into two equivalent circular fields rotating in opposite directions (Fig. 3.17). The division of the elliptical field into circular fields rotating in the forward and reverse directions is achieved using the method of symmetric components, which identifies the MMF of the positive and reverse sequence.

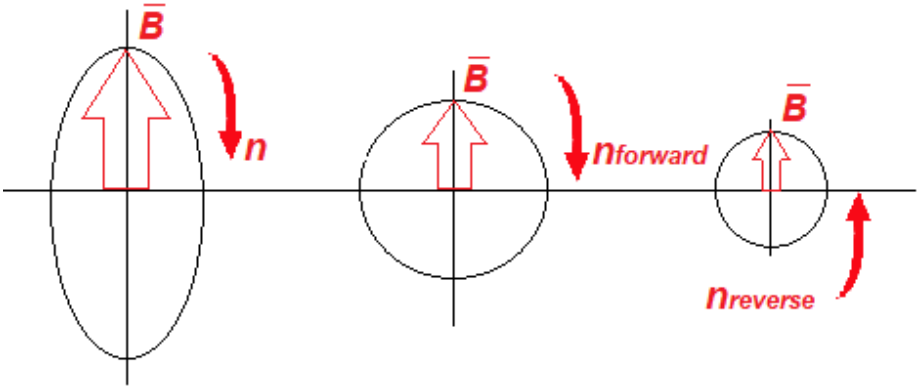

Fig.3.17. Elliptical magnetic field in the machine's working air gap and its decomposition into two component circular fields: forward and reverse.

Therefore, in a two–phase winding supplied with sinusoidal current, and when an asymmetrical air gap arises due to wear on the bearing shields, the MMF of phase $\overline{F}_B$ (B–Y) lags behind the MMF of phase $\overline{F}_A$ (A–X) by an angle $\alpha = -120° = -\frac{2}{3}\pi$, following these equations:

$$\overline{F}_A = \overline{F}_{mi}\, sin\, \omega t, \tag{3.61}$$

$$\overline{F}_B = \overline{F}_{mi}\, sin(\omega t - \tfrac{2\pi}{3}). \tag{3.62}$$

In this situation, the vectors of the direct and reverse sequence MMFs $\overline{F}_{m1}$; $\overline{F}_{m2}$ are unequal $\overline{F}_{m1} \neq \overline{F}_{m2}$. When expressing the MMF vectors for each phase $\overline{F}_A$ and $\overline{F}_B$ are expressed considering direct and reverse sequences, they can be written as:

$$\overline{F}_A = \overline{F}_{A1} + \overline{F}_{A2}, \tag{3.63}$$

$$\overline{F}_B = \overline{F}_{B1} + \overline{F}_{B2}. \tag{3.64}$$

Here, it's assumed that the corresponding MMF components satisfy:

$$\overline{F}_{A1} = -j\overline{F}_{B1}, \tag{3.65}$$

$$\overline{F}_{A2} = +j\overline{F}_{B2}. \tag{3.66}$$

The MMF vectors $\overline{F}_{A1}$ and $\overline{F}_{B1}$ for each phase form a direct-sequence MMF system (Fig. 3.18 a), where vector $\overline{F}_{A1}$ leads vector $\overline{F}_{B1}$ by an angle 120 °, while the reverse-sequence MMF vectors $\overline{F}_{A2}$ and $\overline{F}_{B2}$ form a reverse-sequence MMF system (Fig. 3.18 b), with vector $\overline{F}_{A2}$ lagging behind vector $\overline{F}_{B2}$ by 120 °.

The diagram depicting the decomposition of the stator winding's MMF vectors into a system of forward (a) and reverse (b) sequence vectors, is illustrated in Fig. 3.18 a, b [125].

The magnitudes of the direct and reverse sequence vectors are found by into the expressions for ($\overline{F}_A$) and ($\overline{F}_B$) as described in equations (3.67, 3.68):

$$j\overline{F}_A = \overline{F}_{Ad} - \overline{F}_{Ar}, \tag{3.67}$$

$$\overline{jF}_B = \overline{F}_{Bd} - \overline{F}_{Br}. \tag{3.68}$$

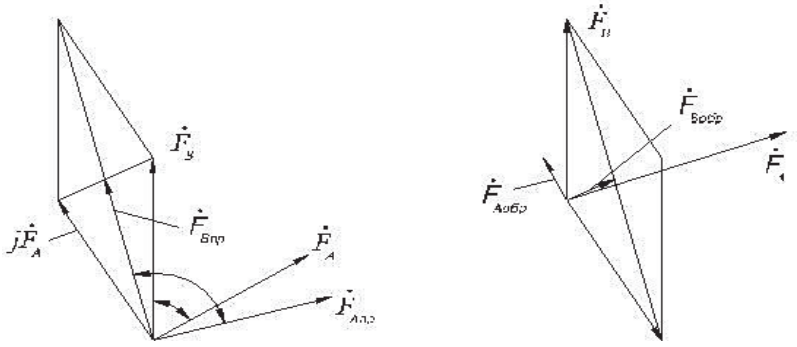

Fig. 3.18. Diagram of the decomposition of the stator winding MMF vectors into forward (a) and reverse (b) sequence vectors systems.

Under the conditions of equations (3.69, 3.70) are satisfied, the equations for the traveling waves of the forward and reverse rotating fields become (3.71, 3.72):

$$F_{Bd} = F_{Ad} = F_d, \tag{3.69}$$

$$F_{Br} = F_{Ar} = F_r, \tag{3.70}$$

$$F_{Xd} = F_d \sin(\omega t - \frac{\pi x}{\tau}), \tag{3.71}$$

$$F_{Xr} = F_r \sin(\omega t + \frac{\pi x}{\tau}). \tag{3.72}$$

In analyzing the performance of multiphase electric motors and drives, the input voltages and phase resistances are generally known, while the outcome of interest is the overall magnitude and configuration of the magnetic flux (Φ) within the motor's air gap.

Any change in the shape of the magnetic flux (Φ) within the air gap between the stator and rotor, from cylindrical to elliptical, directly impacts the power factor ($cos\,\varphi$) of electric motors, regardless of whether they are AC or DC motors, leading to its reduction (Fig. 3.19).

Reducing the power factor ($cos\,\varphi$) in electric motors leads to several adverse effects, including diminished shaft output power (P_2), mechanical torque (M), and efficiency (η).

According to *ISO 10816*, the strength assessment of the gearbox housing is divided into the evaluation of strength based on permissible stresses and the assessing of strength based on the fatigue limit safety factor. For each operational mode, a minimum required safety factor is specified, and the calculated safety factors must not fall below these minimum values .

The evaluation of strength concerning the fatigue resistance factor for load-bearing components is conducted following the guidelines set forth in *ISO 10816* [128].

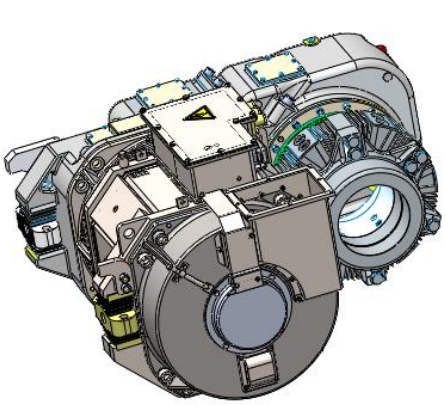

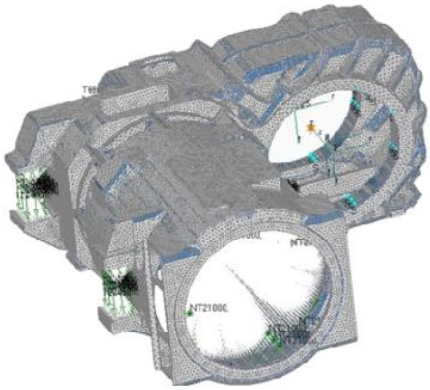

Parameter	Designation	Value
Power of traction motor shaft in continuous mode (kW)	P_N	300
Maximum power at the traction motor shaft in continuous mode (kW)	P_{Max}	446
Maximum starting torque of the traction motor (Nm)	M_{max}	2702
Nominal starting torque of the drive motor (Nm)	M_N	1211
Maximum rotor speed of the traction motor (min^{-1})	n	4774
Location of acceleration application	Direction of acceleration	Acceleration values, g
Acceleration on gear housing and traction motor for strength (g)	Vertical transverse longitudinal	15 15 15
Acceleration on gearbox housing and traction motor for fatigue (g)	Vertical transverse longitudinal	2.5 4.7 5.4

Finite elements	
TETRA 10	Springs

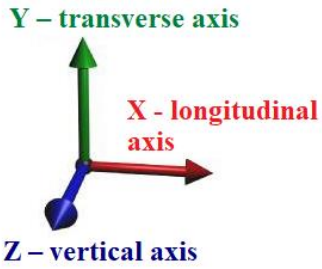

Fig. 3.19. Finite element model.

The finite elements range in size from 6 to 10 mm. The computational model is depicted in Fig. 3.20 and includes 766 977 elements and 1 201 581 nodes.

Material: EN-GJS-400-18-LT according to *ISO 10816* (for high strength cast iron):

- Elastic modulus E = 169 000 MPa;
- Poisson's ratio μ = 0.275;
- Yield strength σ_y = 220 MPa.

The model includes both the gearbox housing and the traction motor housing. The stator's electrical part is represented mass at the center of gravity, as illustrated in Fig. 3.20 and 3.21.

In accordance with the technical specifications 805046 – “Requirements for dynamic characteristics”, the equivalent stress, calculated using the von Mises criterion (σ_{eq}), must not exceed the permissible stress for the material in the specific area under analysis [128].

In Fig. 3.20 and 3.21 it is shown that at the point of suspension attachment represented by a rubber-cord shock absorber the rotational limitation is fixed. Rotational limits are also applied at the locations of bearings. The forces created by the acceleration of the rotor mass are transmitted through the reaction forces in the bearings. The forces created by the engagement of the gears create reaction forces in the bearings. The reactions of the supports are determined from the equilibrium equation: the sum of the moments of the external forces relative to the support in question and the moment of reaction in the other support is equal to zero.

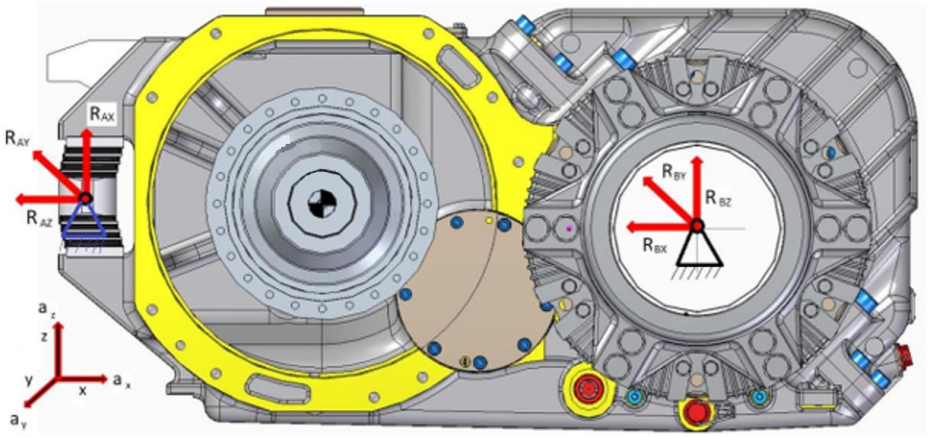

Fig. 3.20. Mounting configuration for design modes I and II. Stiffness: Horizontal: 1000 N/mm; Vertical: 35 000 N/mm; Axial: 1900 N/mm.

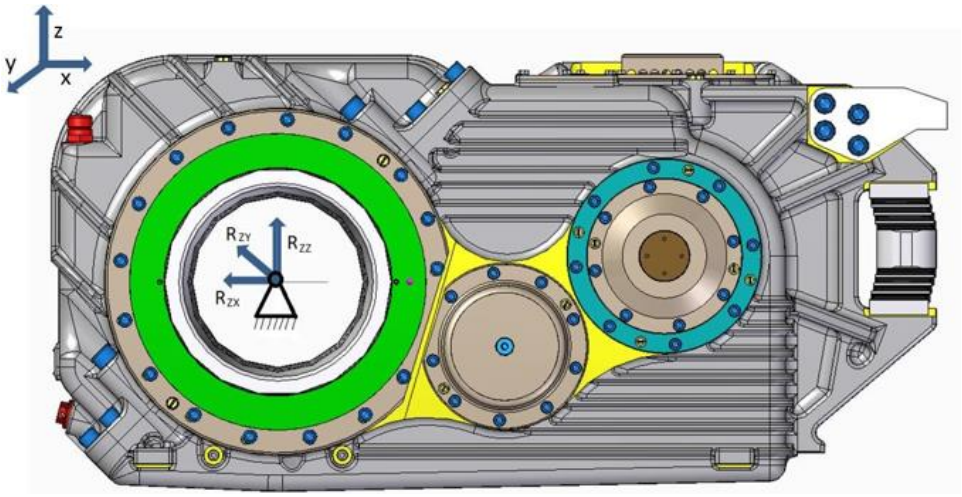

Fig. 3.21. Mounting configuration for design modes I, II, and III. Stiffness: Horizontal: 1000 N/mm; Vertical: 35 000 N/mm; Axial: 1900 N/mm.

To assess the mechanical stress of the structure, three test modes are provided, taking into account the specified direction of rotation of the rotor. The traction forces created by the MGU in all three modes are presented in Table 3.10.

Table 3.10

The traction forces created by the MGU in all three modes

	Mode I	Mode II	Mode III
	Maximal MGU torque Startup from stationary position 2 702 Nm	Maximal MGU torque Startup from stationary position 11 000 Nm	MGU torque 1 211 Nm Additional impacts
			$a_x = \pm 2{,}5$ g (impact in the longitudinal direction); $a_y = \pm 4{,}7$ g (impact in the axial direction); $a_z = \pm 5{,}4$ g (impact in the vertical direction)
	Forward / Reverse rotation	Forward / Reverse rotation	Forward / Reverse rotation
tangential force, N $F_t = 2M_{rot}/D_0$	39 004	158 845	17 487
radial force, N $F_r = F_t \cdot tg\alpha / cos\beta$, $\alpha = 20°$, $\beta = 13°$	14 570	59 336	6 532
axial force, N $F_a = F_t \cdot tg\beta$	9005	36 672	4 037

3.9.1. Mode I (Forward rotation)

Fig. 3.22 illustrates a schematic of the bearings in the first gear stage, and Table 3.11 provides the load values on these bearings within the coordinate system.

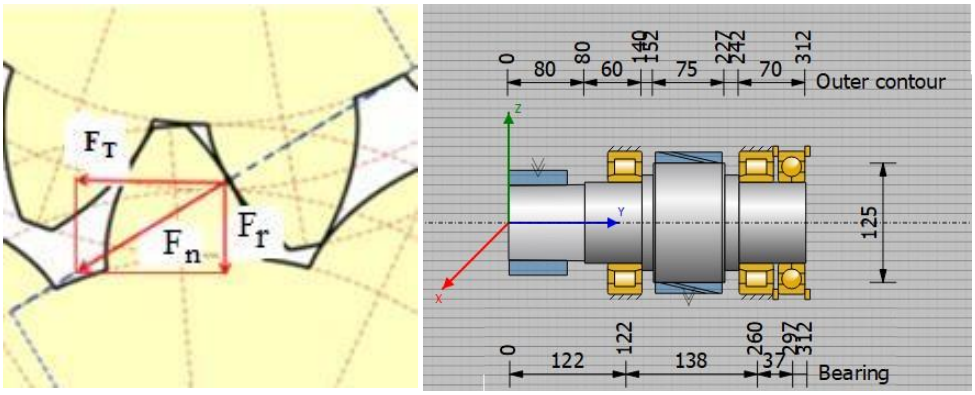

Fig. 3.22. Distance between gear bearings.

Table 3.11

Load on transmission bearings in the coordinate system

Bearing	Force [H]						
	x´		*y´*	*z´*		*xz´*	
Direction	Forward	Reverse	Forward / reverse	Forward	Reverse	Forward	Reverse
P1	- 19 652	6 824	0	- 14 584	16 403	24 472	17 766
P2	- 11 912	101	0	- 14 326	22 896	18 632	22 896
P3	0	0	- 9005 / 9005	0	0	0	0

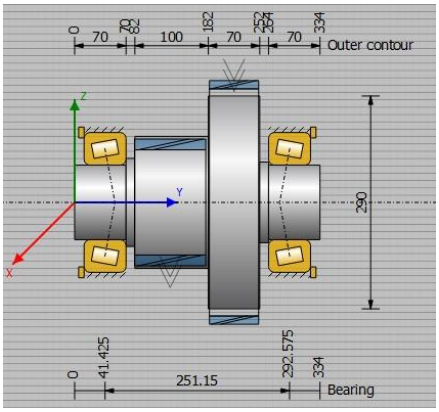

Fig. 3.23. Distance between the bearings of the second gear.

In this mode, the system experiences impact in all coordinate directions, with the following accelerations:

$$ax = \pm 15g$$
$$ay = \pm 15g$$
$$az = \pm 15g$$

The resultant force acting on the gearbox housing at the first gear bearing within the x-z plane is applied over a load angle of 60 degrees. Additionally, an axial force is applied to the gearbox housing from the third bearing's side.

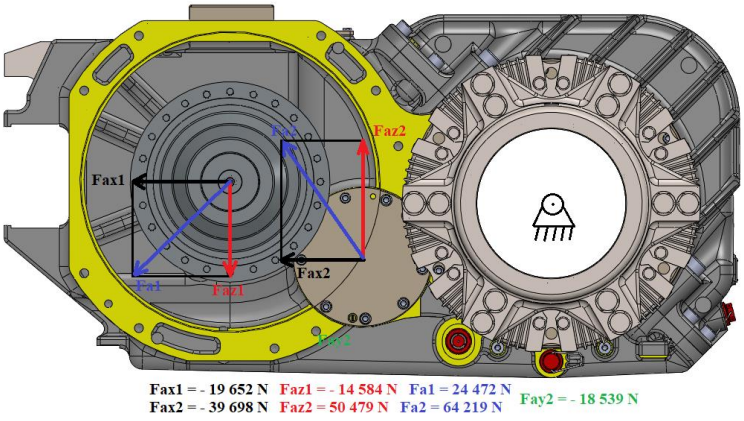

Fig. 3.24. Loads on the 1st and 4th bearings in operating Mode I.

The resulting force on the gearbox housing at the second gear bearing in the x-z plane is also distributed over a 60 ° load angle.

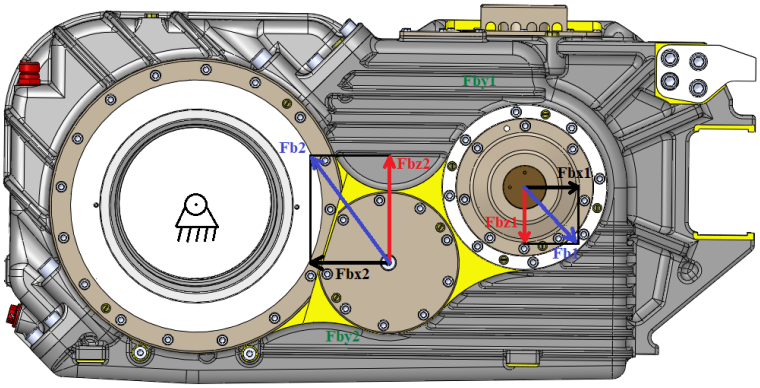

Fbx1 = - 11 912 N **Fbz1 = - 14 326 N** **Fb1 = 18 632 N** **Fby1 = - 9005 N**
Fbx2 = + 15 331 N **Fbz2 = + 39 089 N** **Fb2 = 41 988 N** **Fby2 = 10 738 N**

Fig. 3.25. Load on the 2nd, 3rd, and 5th bearings in operating Mode I.

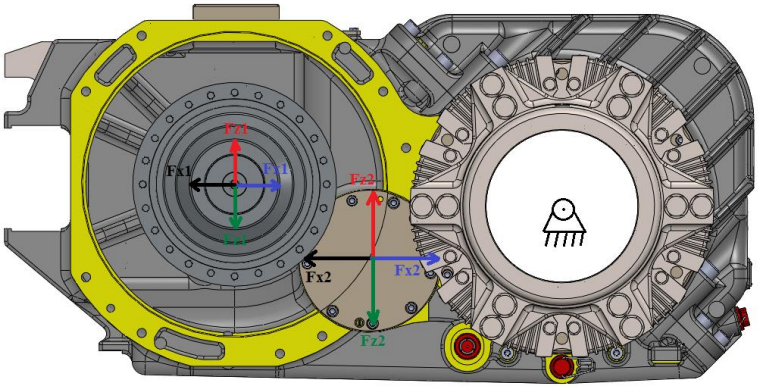

Fx1 = - 22 600 N **Fz1 = + 22 600 N** **Fx1 = + 22 600 N** **Fz1 = - 22 600 N**
Fx2 = - 3606 N **Fz2 = + 3606 N** **Fx2 = + 3606 N** **Fz2 = - 3606 N**

Fig. 3.26. Inertial load of the rotor on the 1st bearing.

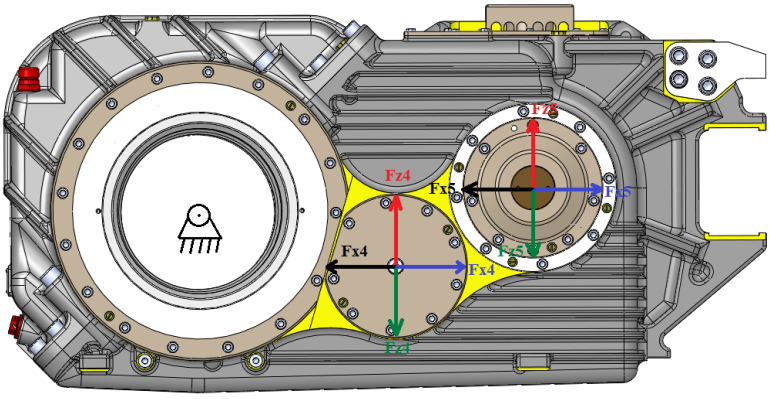

Fx4 = + 3324 N **Fz4 = + 3324 N** **Fx4 = - 3324 N** **Fz4 = - 3324 N**
Fx5 = + 2861 N **Fz5 = + 2861 N** **Fx5 = - 2861 N** **Fz5 = - 2861 N**

Fig. 3.27. Inertial load of the shafts on the 2nd bearing.

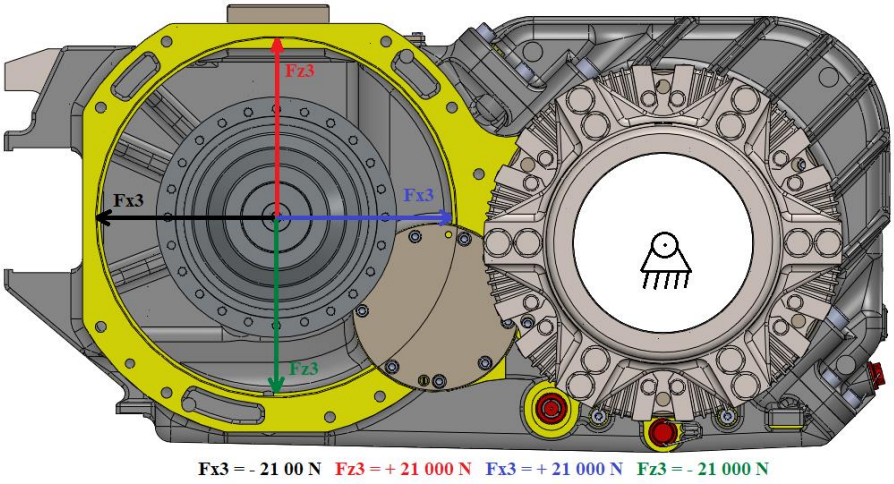

Fig. 3.28. Inertial load of the rotor on the motor bearing.

3.9.2. Mode I (Reverse rotation)

In reverse rotation, the combined force acting on the housing at the first bearing seat of the operating gear within the x–z plane is spread across a 60 ° load angle. Additionally, there is an axial load applied to the gearbox housing at the bearing seat, as depicted in Fig. 3.29.

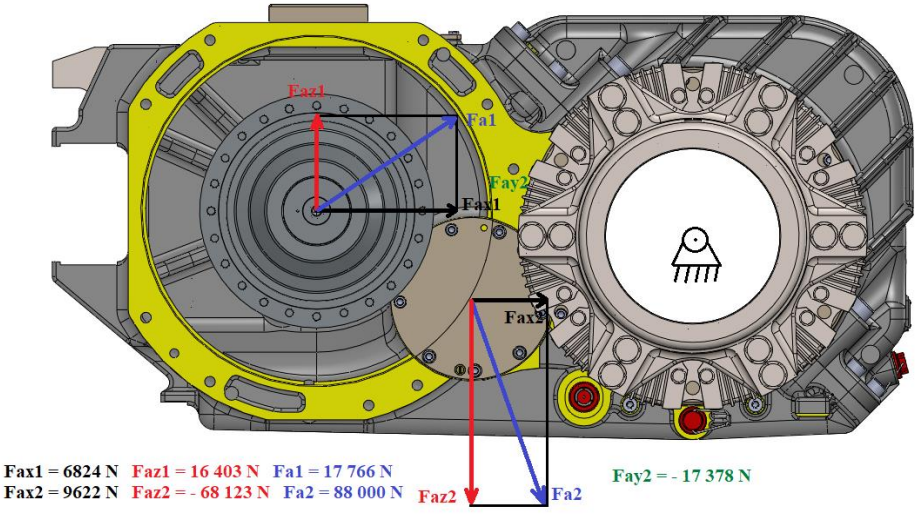

Fig. 3.29. Load on the 1st and 4th bearings in operating Mode I.

The combined force acting on the housing at the second bearing seat of the operating gear within the x–z plane is also distributed over a 60 ° load angle.

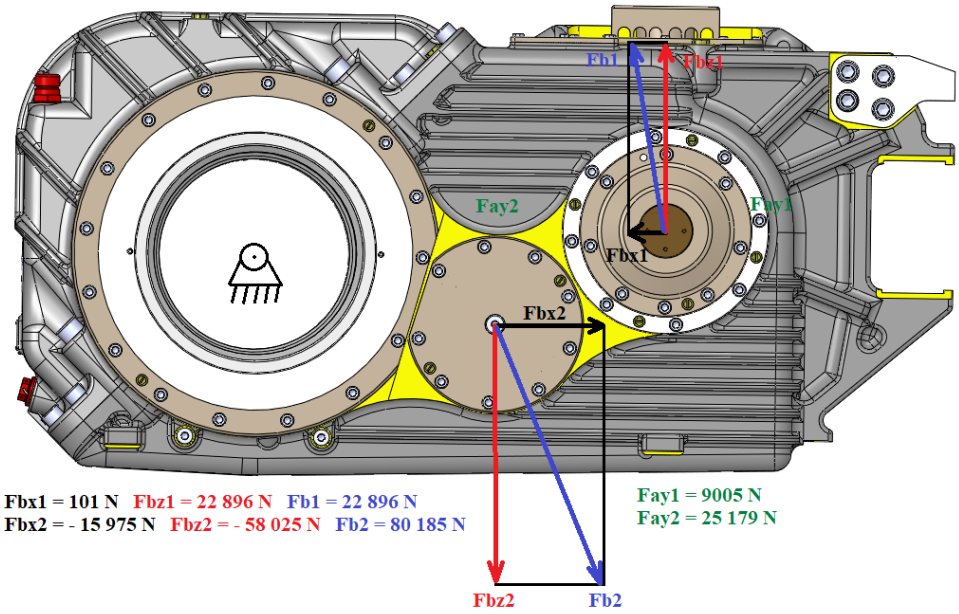

Fig. 3.30. Load on the 2nd, 3rd, and 5th Bearings in Operating Mode I.

3.9.3. Mode II (Forward rotation)

The load values for the bearings in the first stage are displayed in Table 3.12, while Table 3.13 contains the load values for the bearings in the second stage.

Table 3.12

Bearing load values in the first gear stage based on the coordinate system

Bearing	Force [H]						
	x′		*y′*	*z′*		*xz′*	
Direction	Forward	Reverse	Forward / reverse	Forward	Reverse	Forward	Reverse
P1	- 82 075	30 467	0	- 50 593	74 258	96 415	80 265
P2	- 46 424	- 2277	0	- 61 706	91 127	77 219	91 155
P3	0	0	- 36 659 / 36 659	0	0	0	0

Table 3.13

Bearing load values in the second gear stage based on the coordinate system

Bearing	Force [H]						
	x′		*y′*	*z′*		*xz′*	
Direction	Forward	Reverse	Forward / reverse	Forward	Reverse	Forward	Reverse
P4	- 161 508	39 460	- 80 084 / - 78 772	205 536	- 279 230	261 461	282 004
P5	82 409	- 65 324	48 328 / 110 529	161 365	- 232 071	173 013	241 089

In Figs. 3.31 – 3.32 the resulting radial and axial loads are shown, along with the inertial radial loads acting on the bearings and the reactions to the accelerating forces in the labyrinths for the calculated Mode II.

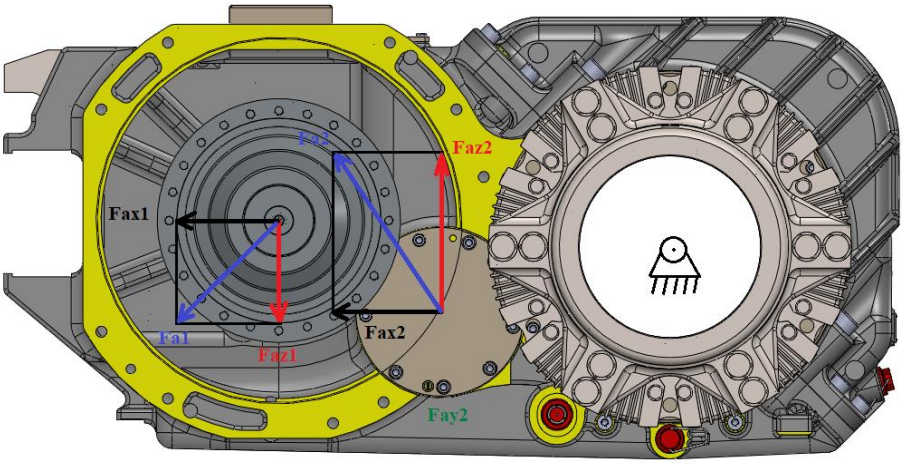

Fig. 3.31. Load on the 1st and 4th bearings in operating Mode II.

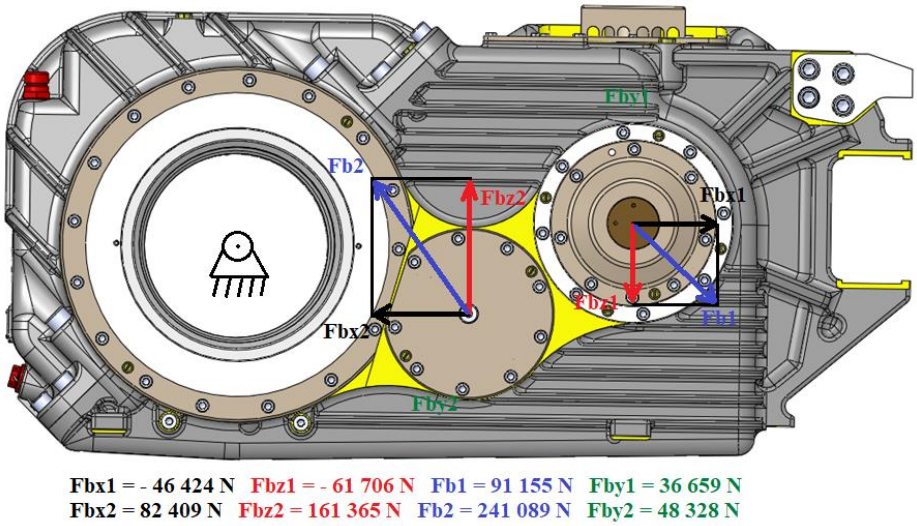

Fig. 3.32. Load on the 2nd, 3rd, and 5th bearings in operating Mode II.

3.9.4. Mode II (Reverse rotation)

Figs. 3.33 – 3.34 illustrate the resulting radial and axial loads, as well as the inertial radial forces acting on the bearings and the reactions to the accelerating forces in the labyrinths for Mode II in reverse rotation.

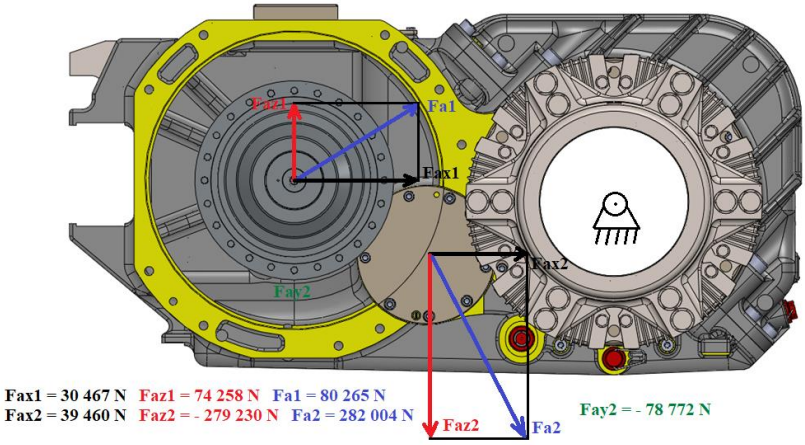

Fig. 3.33. Load on the 1st and 4th bearings in operating Mode II.

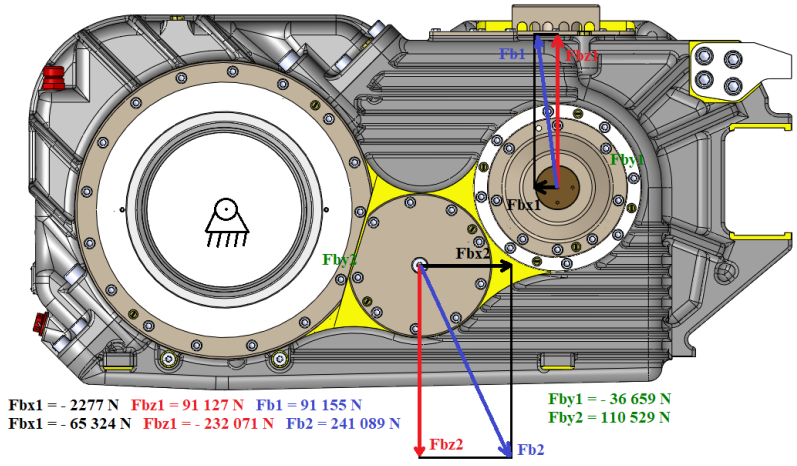

Fig. 3.34. Load on the 2nd, 3rd, and 5th bearings in operating Mode II.

3.9.5. Mode III (Forward rotation)

Tables 3.14 and 3.15 present the load values on the bearings of the first and second stages in the coordinate system. Figs. 3.35 – 3.36 shows the resulting radial and axial loads, along with the inertial radial forces acting on the bearings and the reaction of the accelerating forces in the labyrinths for Mode III during forward rotation.

Table 3.14

Bearing load values in the first gear stage based on the coordinate system

Bearing	Force [H]						
	x′		*y′*	*z′*		*xz′*	
Direction	Forward	Reverse	Forward / reverse	Forward	Reverse	Forward	Reverse
P1	2 904	- 8847	0	5963	- 7967	6623	11 906
P2	200	- 5299	0	10 691	- 5980	10 692	7975
P3	0	0	4036 / - 4036	0	0	0	0

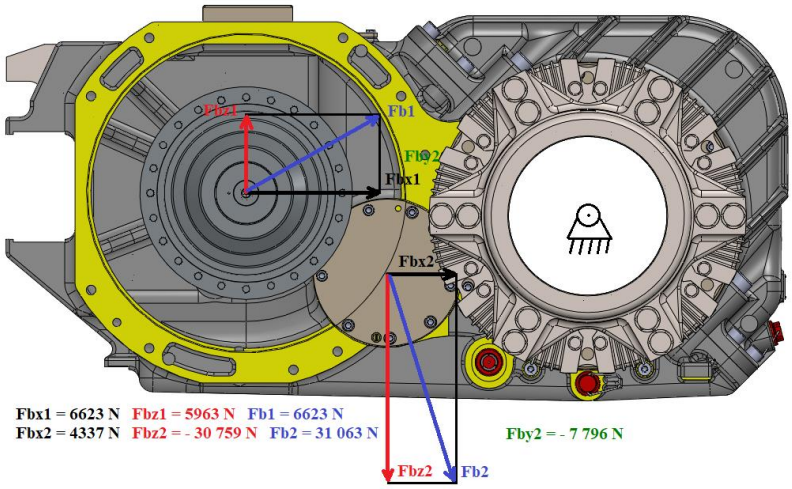

Fig. 3.35. Load on the 1st and 4th bearings in operating Mode III.

Table 3.15

Bearing load values in the second gear stage based on the coordinate system

Bearing	Force [H]						
	x´		*y´*	*z´*		*xz´*	
Direction	Forward	Reverse	Forward / reverse	Forward	Reverse	Forward	Reverse
P4	4337	- 17 825	- 7796 / - 8205	- 30 759	22 444	31 063	28 661
P5	- 7184	6905	11 292 / 4709	- 28 186	17 293	27 154	18 621

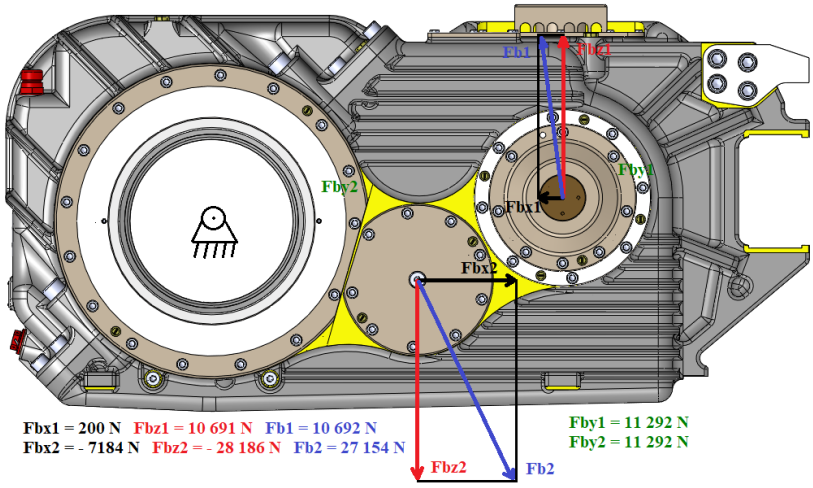

Fig. 3.36. Load on the 2nd, 3rd, and 5th bearings in operating Mode III.

3.9.6. Mode III (Reverse rotation)

Figs. 3.37 – 3.38 illustrate the resulting radial and axial loads, as well as the inertial radial forces acting on the bearings and the reactions to the accelerating forces in the labyrinths for Mode III in reverse rotation.

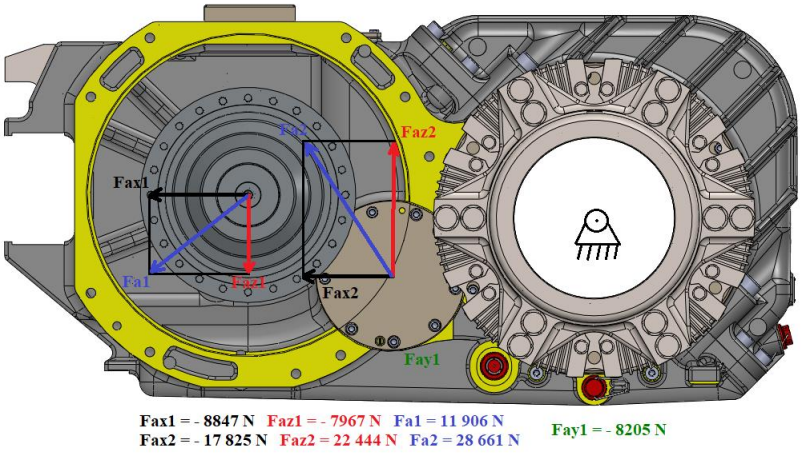

Fig. 3.37. Load on the 1st and 4th bearings in operating Mode III.

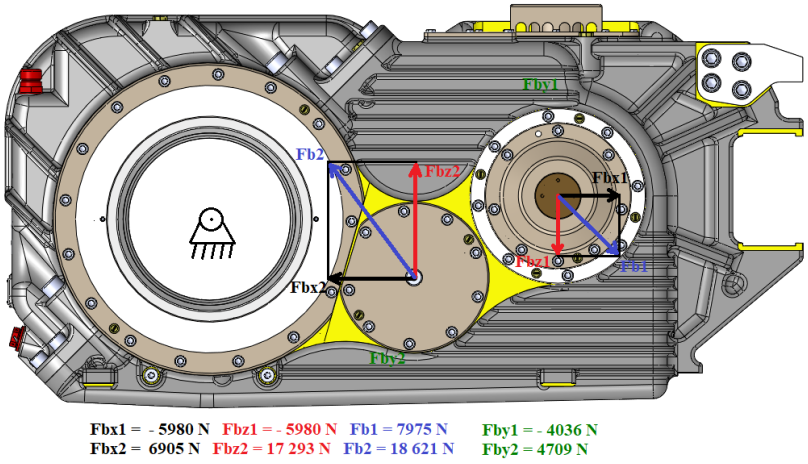

Fig. 3.38. Load on the 2nd, 3rd, and 5th bearings in operating Mode III.

3.10. Third Chapter Conclusions

In this chapter, a comprehensive analysis of wear in traction gear systems of electric rail transport is presented. The research is focused on the operational conditions, dynamics, and durability of electric train traction drives, considering various factors that influence the wear and performance of gear systems. Key factors such as environmental conditions, dynamic forces, and the challenges associated with gear wear are analyzed in detail. Furthermore, methods to evaluate and mitigate gear wear and the associated impact on the longevity of traction systems are explored. This analysis serves as a critical step in improving maintenance procedures and enhancing the overall reliability and efficiency of electric rail systems.

1. Traction drives in electric rail systems operate under extremely challenging conditions, including wide temperature ranges, exposure to abrasive particles, and mechanical stress from

vibrations and dynamic loads. These factors significantly accelerate the wear of gearbox components.

2. The dynamic forces acting on the traction systems, such as oscillations due to track irregularities, lateral swaying, and hunting motions, cause considerable stress on the gearbox. This results in significant wear and fatigue over time, reducing the lifespan of the components.

3. Gear wear, especially when new gears are paired with worn-out wheels, increases the dynamic loads significantly. This heightened stress negatively affects the performance of the drive system. Periodic restoration of the gear teeth profiles is recommended to maintain the efficiency of the gear mesh and reduce high-frequency dynamic loads.

4. The chapter utilizes finite element analysis to identify critical areas in the gearbox where stress concentrations occur, particularly at sharp transitions in geometry and surface imperfections. This analysis helps in identifying potential failure points and designing improvements to enhance durability.

5. The research emphasizes the need for improved maintenance strategies, including regular inspections and timely restoration of worn gear profiles, to prolong the operational life of traction systems. Additionally, design enhancements such as better material selection and structural modifications are necessary to handle the stresses more effectively.

6. The implementation of more advanced and validated diagnostic tools is crucial for early detection of wear-related issues. This would improve the reliability of the gear systems and reduce unscheduled downtimes in rail transport operations.

These conclusions highlight the importance of ongoing monitoring, maintenance improvements, and design optimizations to ensure the reliability and longevity of traction systems in electric rail transport.

CHAPTER 4. INFLUENCE OF DYNAMIC LOADS ON STRESS AND FATIGUE OF STRUCTURES

4.1. Stress of Metal Structure Under the Influence of Driving Forces

From the study using the finite element method presented in the previous chapter, an analysis of the presence and concentration of points of maximum mechanical stress on the MGU housing, as the most loaded and exposed to vibration forces unit of the traction drive of the electric train, will be presented below [113].

Calculations of stresses on the gear shaft showed that their values vary from 6686 N to 41,411 N depending on the operating modes of the mechanism. In order to assess the effect of loads on the service life of the housing, it is extremely important to determine the resistance of the part to fatigue failure at various levels of the mechanism.

To identify the stress levels that reduce a part's lifespan, calculating the average endurance limit is essential [116], [119]. The average fatigue limit of the part $\sigma_{-1\text{dyn}}$ (MPa), corresponding to a 50 % probability of failure, is determined by considering the fatigue limit reduction coefficient K_{end}:

$$\sigma_{-1\text{dyn}} = \frac{\sigma_{-1}}{K_{end}}, \tag{4.1}$$

The coefficient K encompasses technological and design factors that contribute to a reduction in the endurance limit and is calculated using the formula:

$$K_{end} = \left(\frac{K_\sigma}{K_{dyn\_\sigma}} + \frac{1}{K_{F\sigma}} - 1\right)\frac{1}{K_V K_A}, \tag{4.2}$$

where: $\frac{K_\sigma}{K_{dyn\_\sigma}}$, $K_{F\sigma}$ – effective stress concentration factor and surface roughness influence factor; K_V, K_A – coefficients accounting for hardening and anisotropy of metal properties.

The effective stress concentration factor $\frac{K_\sigma}{K_{dyn\_\sigma}}$ is determined by the following equation:

$$\frac{K_\sigma}{K_{dyn\_\sigma}} = a_\sigma F(\theta, v_\sigma), \tag{4.3}$$

where: a_σ is identified according to *ISO 10816* using the nomogram $F(\theta, v_\sigma)$, where: F – represents a function of the fatigue fracture similarity criterion θ based on the value v_σ. The values for calculating the coefficient from the nomogram were determined as follows. Based on the geometric dimensions (see Fig. 3.11), the coefficient a_σ is calculated.

The design of the transition flange connection of the motor and traction gearbox is shown in Fig. 4.1.

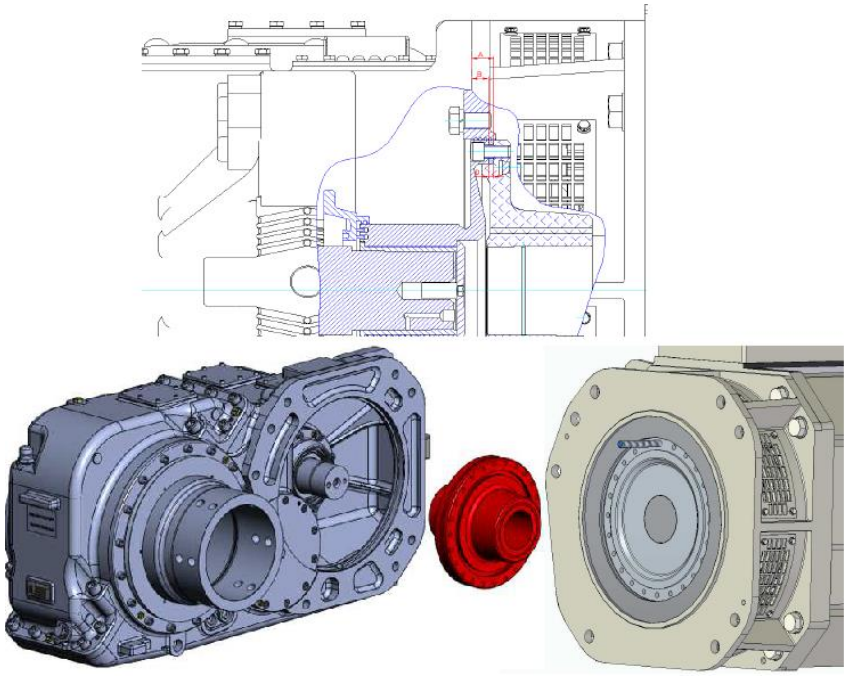

Fig. 4.1. MGU internal flange connection.

4.2. Assessment of the Service Life of Structural Elements of MGU by Means of Hypothesis

Due to the fact that cyclic loads caused by seasonal and daily traffic schedules are the most typical for railway transport, the processes associated with the development of fatigue and the structure are accelerated. The results of studies [121], [122], [129], [130], that nevertheless the number of cycles, whether vibration load or single impacts, remains significant, and for the distribution of the probability of failure (destruction or its onset) a normal distribution is used, less often the Pearson or Weibull distribution.

If the load is random or stochastic in nature, then the sample of cases r will contain stress amplitudes σ with repetition up to the limit value k (see Fig. 4.2).

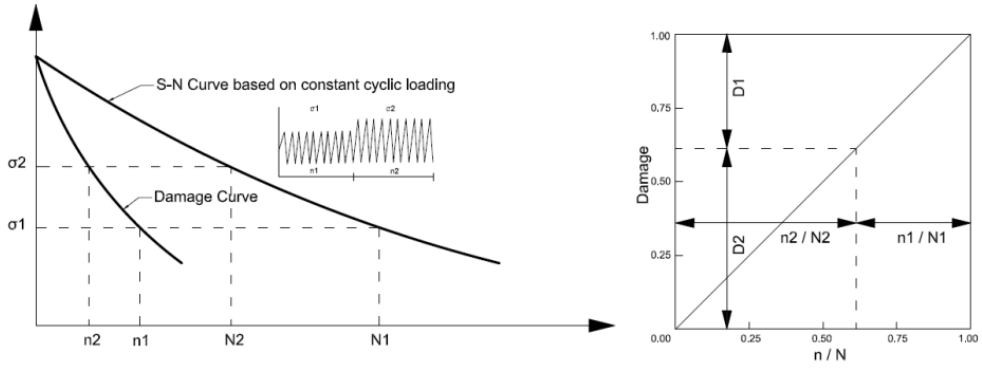

Fig. 4.2. Linear cumulative progression of the defect.

The calculation considers the total number of cycles before failure of the part λ, over the entire time. The number of realized load cycles at the amplitude σ_{ai} can be defined as $n_{i} = \lambda \cdot v_{ib}$. In the case where the number of cycles of impact before the occurrence of the fact of destruction, according to the fatigue characteristic at σ_{ai}, is equal to N_i, then with such an amplitude of stresses the product will be safely in the working condition for a certain fraction of its resource n_i / N_i.

The value a_p is the limiting value that the sum of the specified durability reaches for the case of cyclic loading [131], [132].

The safety margin calculation was performed at stress levels σ_i, factoring in the determined value of the average fatigue limit σ_{-1d}. Probabilistic fatigue diagrams for ductile iron EN–GJS–350–22–LT [117], were used, where the number of cycles N before failure with a probability pN = 50 % is is described by the equation: $\ln (N \times 10^{-3}) = 6.28 - 10.4 \times \ln(\sigma/\sigma^{-1}) + 0.65 \ln \times pN$. Consequently, an exponential dependence was obtained for the hull's lifespan in cycles based on the magnitude of the applied loads $N_{case} = (-3.02 + Kd)/-0.1614$. To assess the risk associated with overloads, the relative durability values n_i / N_i were calculated for each amplitude level σ_i as well as their contribution to the total sum a_p using a traction drive load sequence diagram containing of v_b = 100 000 cycles [117].

4.3. Calculation of Strength Depending on the Stress of the Structure

To obtain the most reliable and closest to real conditions data on the stress of the MGU body, using the finite element method, it is important to consider the combination of simultaneously acting loads. The loads are determined by the design modes at the stage of designing the EMU. The maximum values determined by the calculations cannot be exceeded for each of the design modes: $0.9\sigma_y$ for Mode I and Mode II and $0.6\sigma_y$ for Mode III [119].

The values of equivalent stresses in the gearbox housing during Mode I under forward rotation are illustrated in Figs. 4.3, 4.4, and 4.5. The data and the computed safety factor for Mode I are provided in Table 4.1.

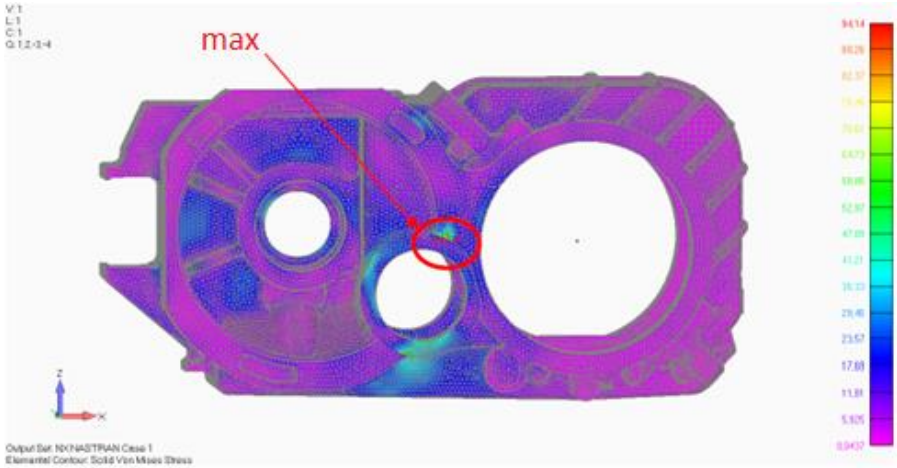

Fig. 4.3. Equivalent stresses on gearbox housing in Mode I (15,15,15)g.

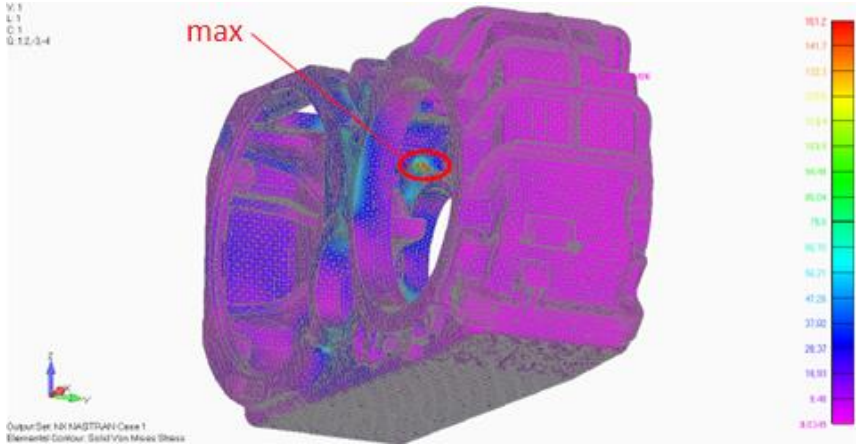

Fig. 4.4. Equivalent stresses on gearbox housing in Mode I (-15,15,15)g.

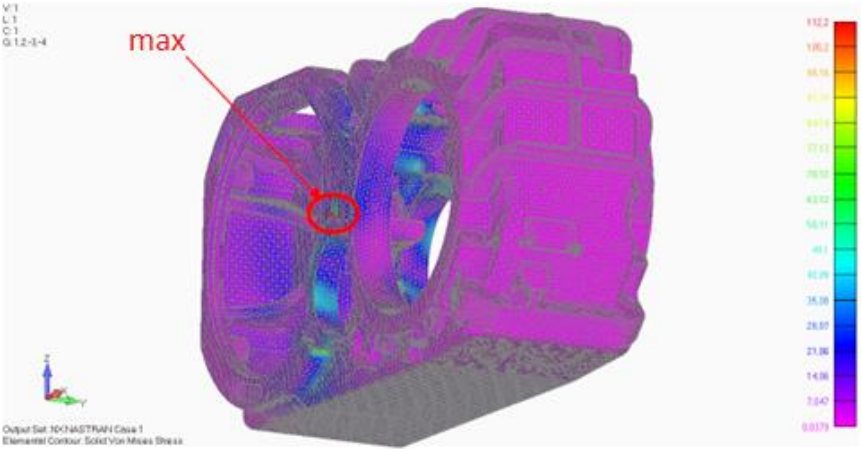

Fig. 4.5. Equivalent stresses on gearbox housing in Mode I (15,15,-15)g.

Table 4.1

Equivalent stresses and safety margin for Mode I – Forward rotation direction

σ_{eq}		σ_y	0,9 σ_y	Safety Margin $0.9\ \sigma_y / \sigma_{eq}$
(15,15,15)g	94.14	240	216	2.29
(-15,-15,-15)g	81.35	240	216	2.65
(-15,-15,15)g	91.61	240	216	2.38
(-15,15,15)g	151.2	240	216	1.42
(15,-15,15)g	112.8	240	216	1.91
(15,15,-15)g	112.2	240	216	1.92
(15,-15,-15)g	132.2	240	216	1.63
(-15,15,-15)g	136.1	240	216	1.58

The minimal safety margin value n = 1.0 for Mode I.

The gearbox housing equivalent stress values in Mode I for reverse rotation are shown in Figs. 4.6., 4.7. and 4.8. Data and calculated safety factor for Mode I are presented in Table 4.2.

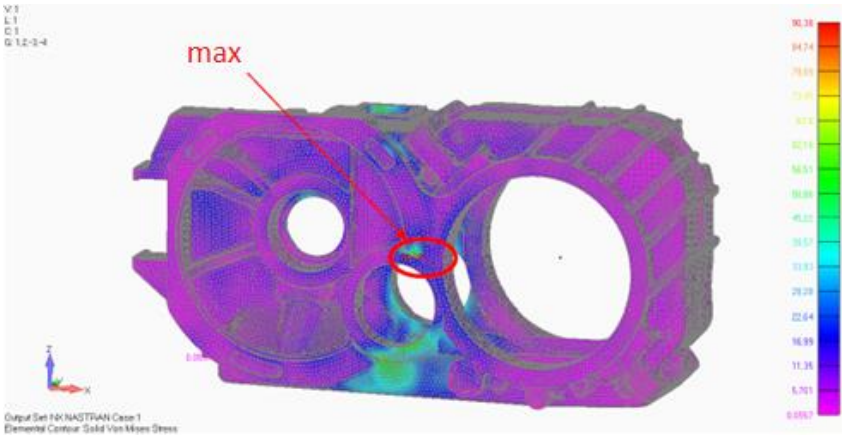

Fig. 4.6. Equivalent stresses on gearbox housing in Mode I (-15,-15,-15)g.

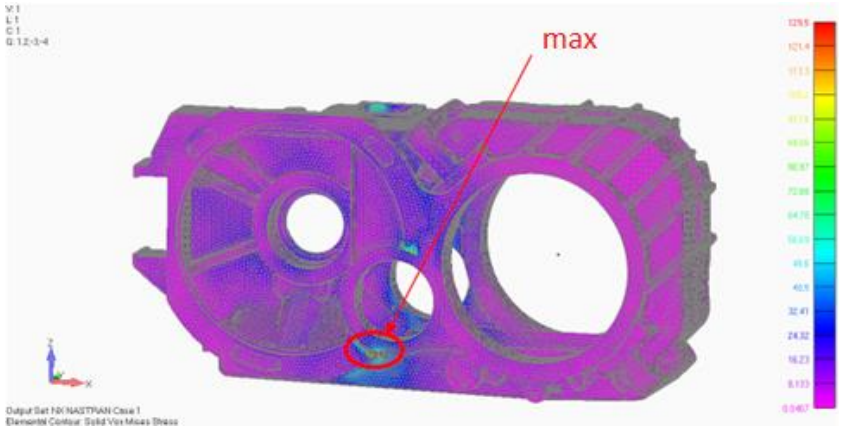

Fig. 4.7. Equivalent stresses on gearbox housing in Mode I (-15,-15,15)g.

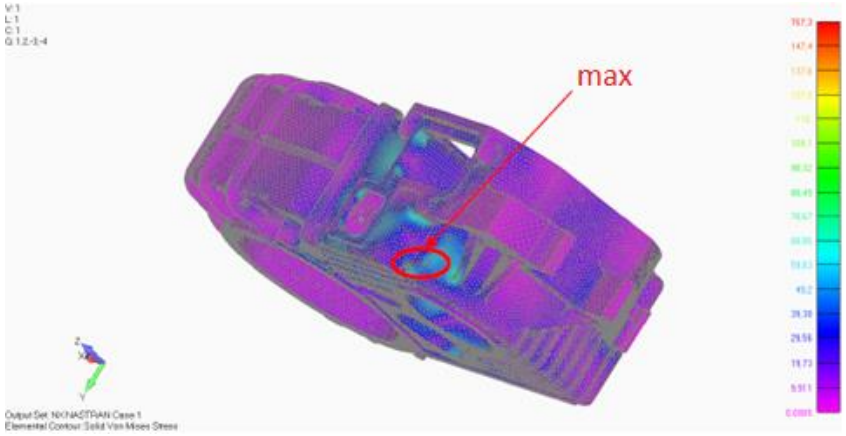

Fig. 4.8. Equivalent stresses on gearbox housing in Mode I (-15,15,15)g.

Table 4.2

Equivalent stresses and safety factor for Mode I – Reverse rotation direction

σ_{eq}		σ_y	0,9 σ_y	Safety Margin 0.9 σ_y / σ_{eq}
(15,15,15)g	88.12	240	216	2.45
(-15,-15,-15)g	90.38	240	216	2.38
(-15,-15,15)g	129.5	240	216	1.66
(-15,15,15)g	157.3	240	216	1.37
(15,-15,15)g	106.5	240	216	2.02
(15,15,-15)g	143.7	240	216	1.50
(15,-15,-15)g	125.7	240	216	1.71
(-15,15,-15)g	142.1	240	216	1.52

The minimal safety margin value n = 1.0 for Mode I.

The gearbox housing equivalent stress values in Mode II for forward reverse rotation are shown in Figs. 4.9. and 4.10. Data and calculated safety factor for Mode II are presented in Table 4.3.

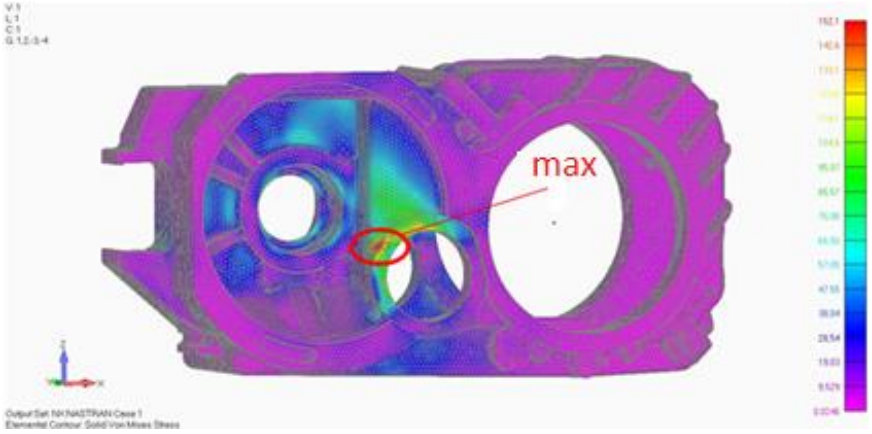

Fig. 4.9. Equivalent stresses on gearbox housing in Mode II for forward rotation.

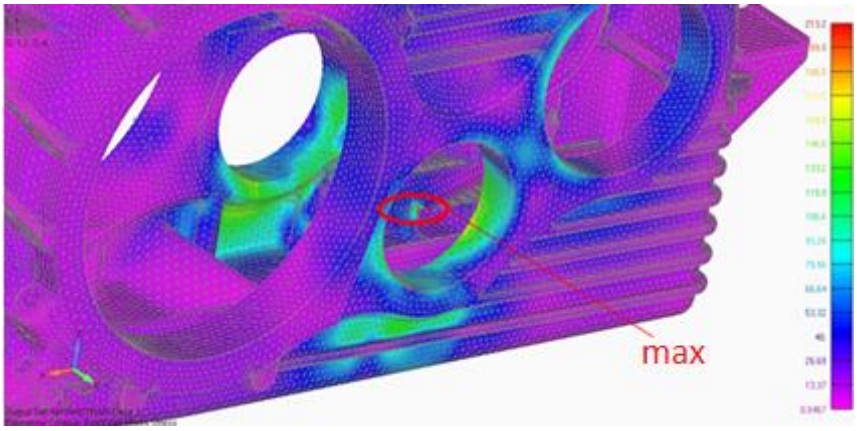

Fig. 4.10. Equivalent stresses on gearbox housing in Mode II for reverse rotation.

Table 4.3

Equivalent stresses and safety factor for Mode II

σ_{eq}		σ_y	0.9 σ_y	Safety factor 0.9 σ_y /σ_{eq}
Forward Rotation	152.1	240	216	1.42
Reverse Rotation	213.2	240	216	1.013

The minimum safety factor n = 1.0 for Mode II.

4.3.1. Assessment of the Safety Factor of Load-bearing Metal Structures of MGU

In the presence of a histogram representing the distribution of stress amplitude values characterizing the stress state of the part during the expected service life and the absence of parameters of the material fatigue curve, the fatigue strength assessment should be performed using the following data presented in Fig. 4.11.

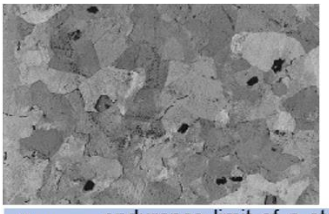

Fatigue resistance:

$$n = \frac{\sigma_{-1p}}{K_\sigma \sigma_a + \Psi_\sigma \frac{\sigma_m}{\alpha_\sigma}}$$

Endurance limit:

$$K_\sigma = \frac{K_1 K_2}{\gamma K_m} K_3$$

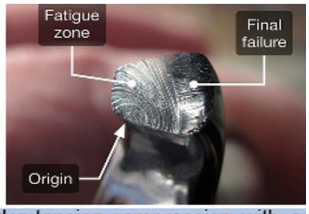

σ_{-1p} — endurance limit of a standard specimen under tension-compression with a symmetric loading cycle, for ISO 10816, $\sigma_{-1p} = 182$ MPa;

K_σ — coefficient accounting for the reduction in endurance limit of the structure compared to the endurance limit of a standard specimen (stress concentration coefficient);

σ_a — stress amplitude (maximum in the concentration zone) of the cycle, MPa;

σ_m — mean stress of the cycle, MPa;

Ψ_σ — coefficient accounting for the effect of cycle asymmetry, taken as $\Psi_\sigma = 0.3$ when $\sigma_m > 0$, and $\Psi_\sigma = 0$ when $\sigma_m < 0$;

α_σ — theoretical stress concentration factor, assumed to be 1.0.

K_1 — coefficient accounting for the influence of material heterogeneity. For rolled, forged, and stamped parts $K_1 = 1.1$, and for cast parts, $K_1 = 1.25$; .

K_2 — coefficient accounting for the influence of internal stresses in the part, dependent on the largest transverse dimension of the part. For dimensions from 250 to 1000 mm, the coefficient ranges from 1.0 to 1.2;

K_m — coefficient accounting for the surface condition of the part and depends on the machining method:

- 1.0 — for polished surfaces;
- 0.9 — for surfaces after fine machining;
- 0.8 — for surfaces after rough machining, surfaces with scale, and steel cast surfaces after sandblasting;

γ — coefficient accounting for the dimensional factor, selected depending on the largest cross-sectional size h:

- 0.8 — for section heights up to 100 mm inclusive;
- 0.75 — for section heights from 100 to 250 mm inclusive;
- 0.7 — for section heights over 250 mm;

K_3 — correction factor used for welded joint zones.

Fig. 4.11. Fatigue resistance evaluation.

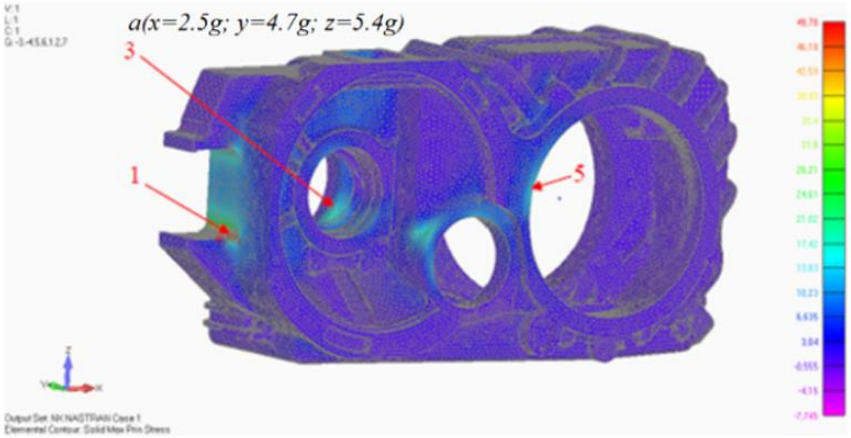

Fig. 4.12. Max Principal Stress [MPa] of Mode III, rotation in forward direction.

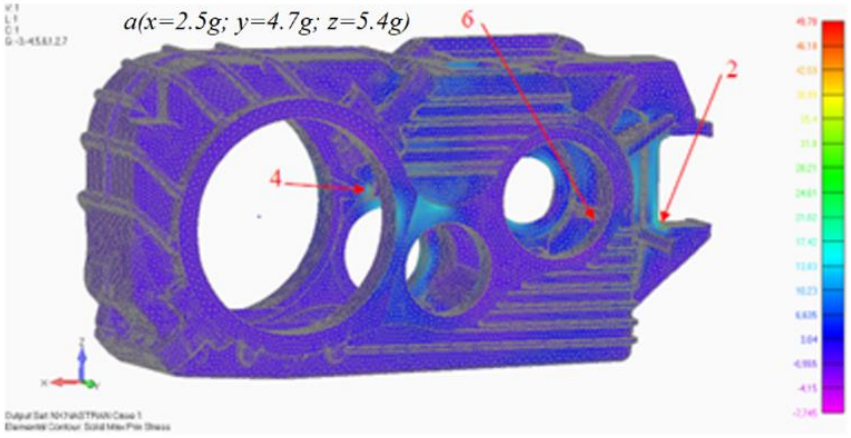

Fig. 4.13. Max Principal Stress [MPa] of Mode III, rotation in forward direction.

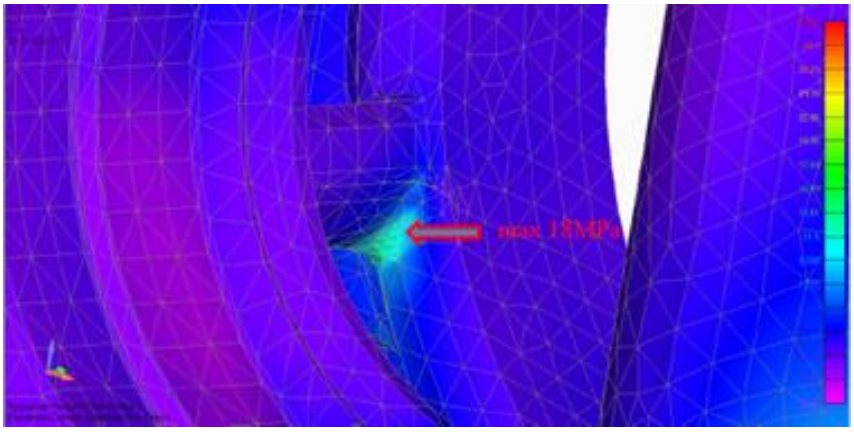

Fig. 4.14. Max Principal Stress [MPa] at point 6 of Mode III, rotation in forward direction.

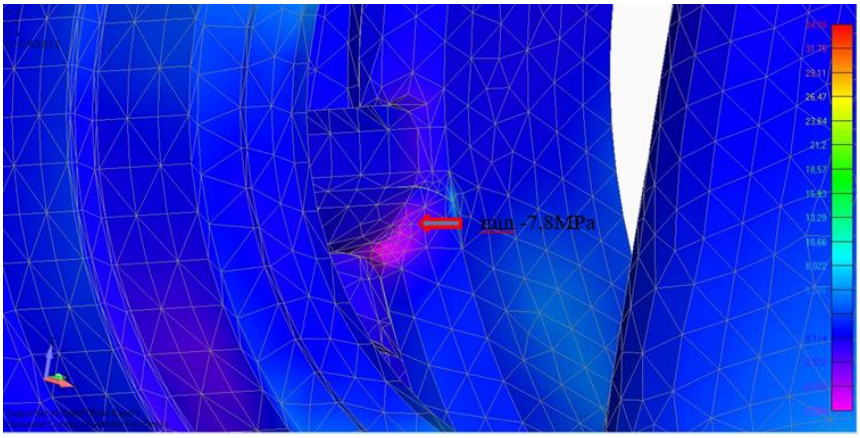

Fig. 4.15. Max Principal Stress [MPa] at point 6 of Mode III, rotation in forward direction.

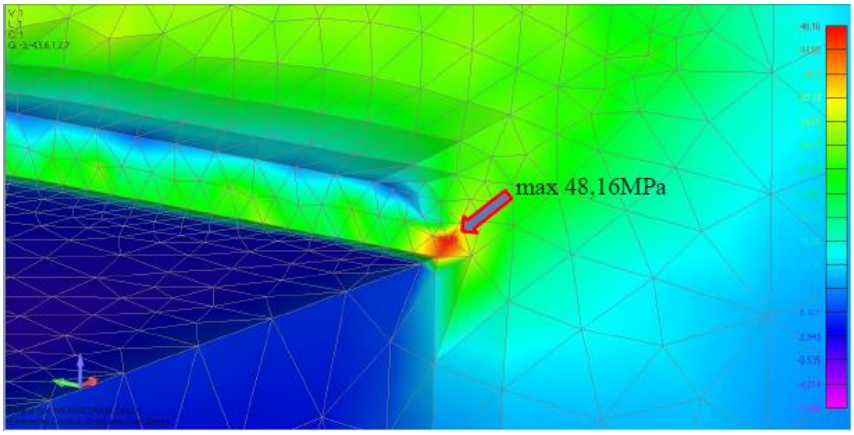

Fig. 4.16. Max Principal Stress [MPa] at point 1 of Mode III, rotation in forward direction.

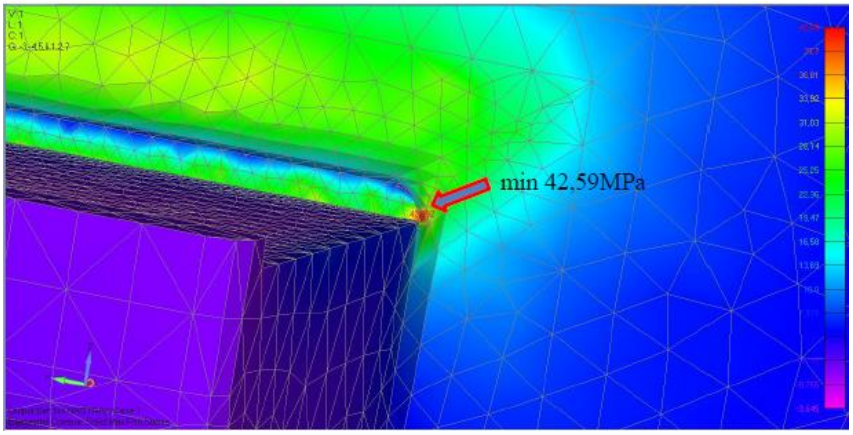

Fig. 4.17. Min Principal Stress [MPa] at point 1 of Mode III, rotation in forward direction.

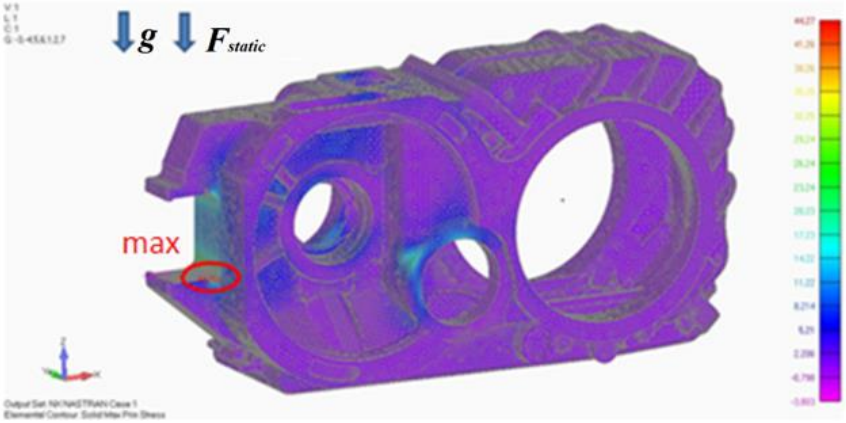

Fig 4.18. Max Principal Stress [MPa] of Mode III, rotation in forward direction.

Table 4.4

Reverse ratation mode. Safety factor of fatigue strength.

Indicator Name (Designation)	Values					
Stress Point Number (max)	1	2	3	4	5	6
σ_{max}(12.5; 4; 13.5) g	49.78	21.20	26.36	33.35	11.32	17.1
σ_{min} (-12.5; -4; -13.5) g	40.98	- 3.64	4.04	22.42	- 3.65	- 15.8
$\sigma_m = (\sigma_{max} + \sigma_{min})/2$	45.38	8.78	15.2	27.88	3.84	0.65
$\sigma_a = \sigma_{max} - \sigma_m$	4.4	12.42	11.16	5.47	7.48	16.45
Ψ_σ	0.3	0.3	0.3	0.3	0.3	0.3
α_σ	1	1	1	1	1	1
K_σ	1.82	1.82	1.82	1.82	1.82	1.82
n	8.42	7.21	10.37	9.93	12.34	6.04

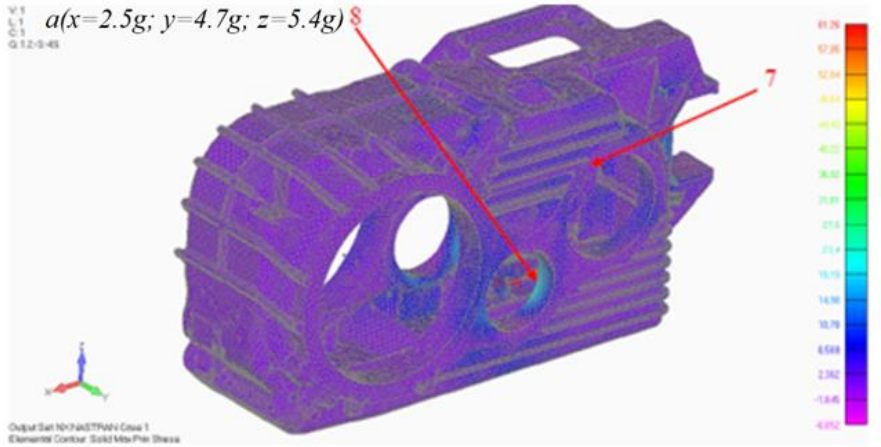

Fig. 4.19. Max Principal Stress [MPa] of Mode III, rotation in reverse direction.

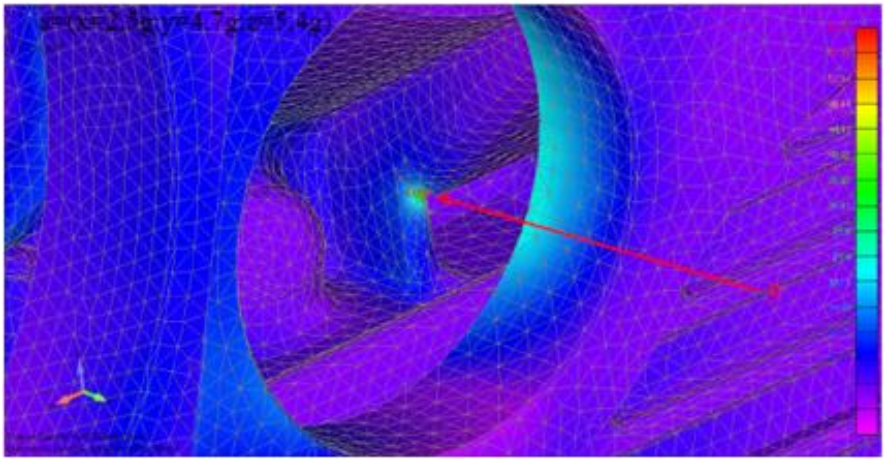

Fig. 4.20. Max Principal Stress [MPa] of Mode III, rotation in reverse direction.

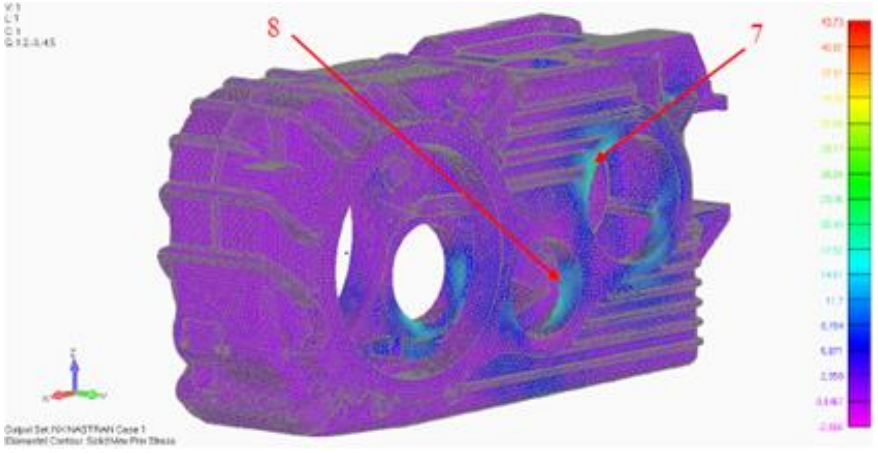

Fig. 4.21. Max Principal Stress [MPa] of Mode III, rotation in reverse direction.

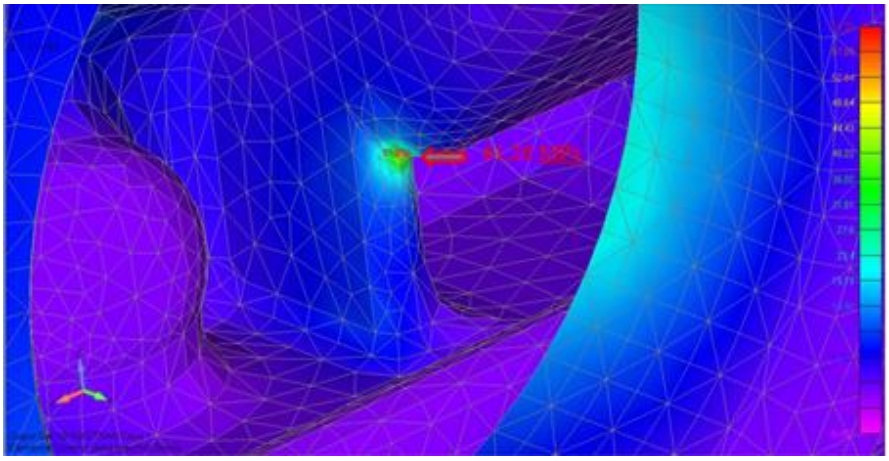

Fig. 4.22. Max Principal Stress [MPa] of Mode III, rotation in reverse direction.

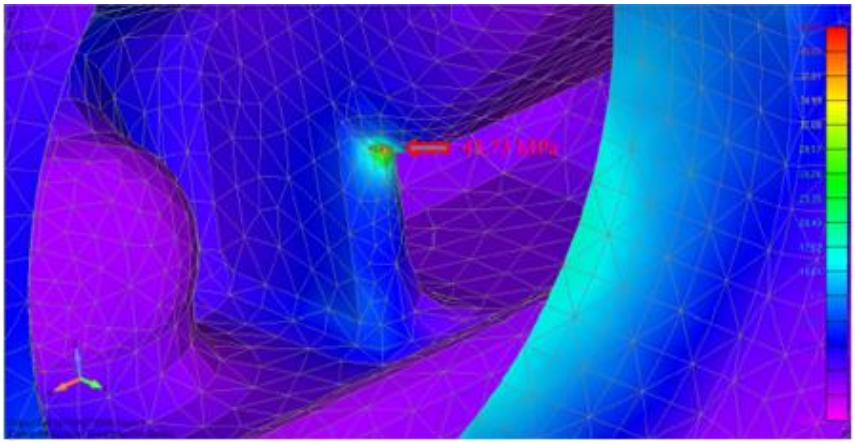

Fig. 4.23. Max Principal Stress [MPa] of Mode III, rotation in reverse direction.

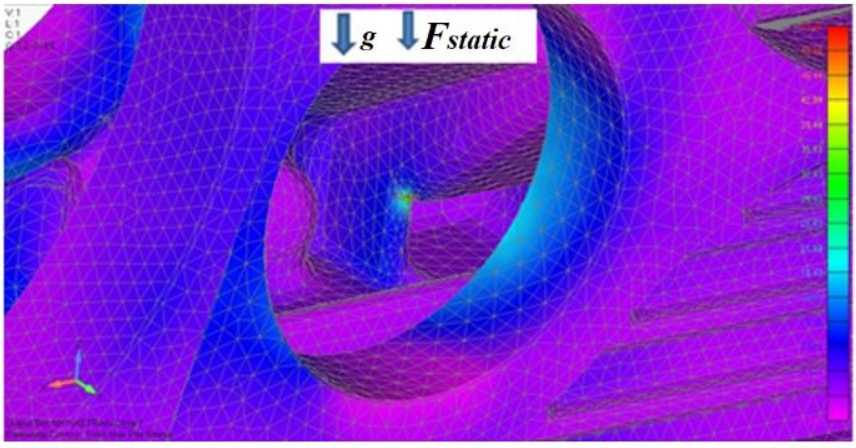

Fig. 4.24 Max Principal Stress [MPa] of Mode III, rotation in reverse direction.

Table 4.5

Reverse ratation mode. Safety factor of fatigue strength.

Indicator Name (Designation)	Values		
Stress Point Number (max)	7	8	9
(12.5; 4; 13.5) g	26.4	23.4	61.26
(–12.5; –4; –13.5) g	-2	11.7	43.73
$\sigma_m = (\sigma_{max} + \sigma_{min})/2$	12.2	17.55	52.49
$\sigma_a = \sigma_{max} - \sigma_m$	14.2	5.85	8.76
Ψ_σ	0.3	0.3	0.3
α_σ	1	1	1
K_σ	1.82	1.82	1.82
n	6.16	11.44	5.75

For the calculated Mode I, the minimum allowable safety margin when calculating the strength based on allowable stresses is $[n]>1.0$.

Table 4.6

Acceptable stresses values.

Calculation Mode	n_{min} (calculated)	$[n]$	Safety margin for the selected design
Mode I (direct rotation direction)			
15g,15g,15g	1	2.31	acceptable
-15g,-15g,-15g	1	2.60	acceptable
-15g,-15g,15g	1	2.45	acceptable
-15g,15g,15g	1	1.47	acceptable
15g,-15g,15g	1	1.85	acceptable
15g,15g,-15g	1	1.87	acceptable
15g,-15g,-15g	1	1.56	acceptable
-15g,15g,-15g	1	1.52	acceptable
11 000 Nm	1	1.39	acceptable
Mode I (reverse rotation direction)			
15g,15g,15g	1	2.41	acceptable
-15g,-15g,-15g	1	2.32	acceptable
-15g,-15g,15g	1	1.63	acceptable
-15g,15g,15g	1	1.30	acceptable
15g,-15g,15g	1	2.07	acceptable
15g,15g,-15g	1	1.54	acceptable
15g,-15g,-15g	1	1.67	acceptable
-15g,15g,-15g	1	1.49	acceptable
11 000 Nm	1	1.05	acceptable

The minimum permissible stresses in accordance with *ISO 10816* allow the safety factors given in the Table 4.6.

For the calculated Mode III, the minimum allowable safety margin when assessing the fatigue resistance of load-bearing elements is $[n]>2.0$.

Table 4.7

Acceptable stresses values.

Calculation Mode	n_{min} (calculated)	$[n]$	Safety margin for the selected design
Mode III (direct rotation direction)			
1	2	8.47	acceptable
2	2	7.23	acceptable
3	2	10.6	acceptable
4	2	9.87	acceptable
5	2	12.40	acceptable
6	2	6.11	acceptable
Mode III (reverse rotation direction)			
7	2	6.19	acceptable
8	2	11.39	acceptable
9	2	5.68	acceptable

The minimum permissible stresses in accordance with *ISO 10816* allow the safety factors given in the Table 4.7.

4.4. Determination of Loads in Elastic Connecting Elements

The gearbox is attached to the motor with a bolted connection. The wheel is attached with a coupling to the output shaft. The gearbox hangs on two elastic bearings on the pinion side and on rubber wedge coupling on the output shaft side. The single cardanic coupling accepts axial, radial and angular misalignments. The structural setup is shown in Fig. 4.25.

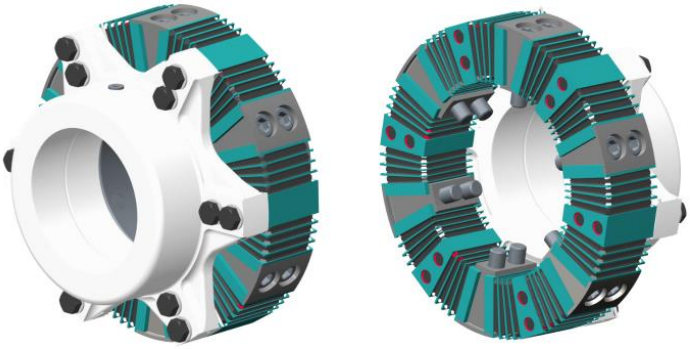

Fig. 4.25. The structural setup of rubber wedge coupling.

Forces from shocks acting on gearbox in calculation of shock forces are considered only vertical acceleration, forces from transverse and longitudinal accelerations are negligible. The general calculation scheme of the acting forces is presented in Fig. 4.26.

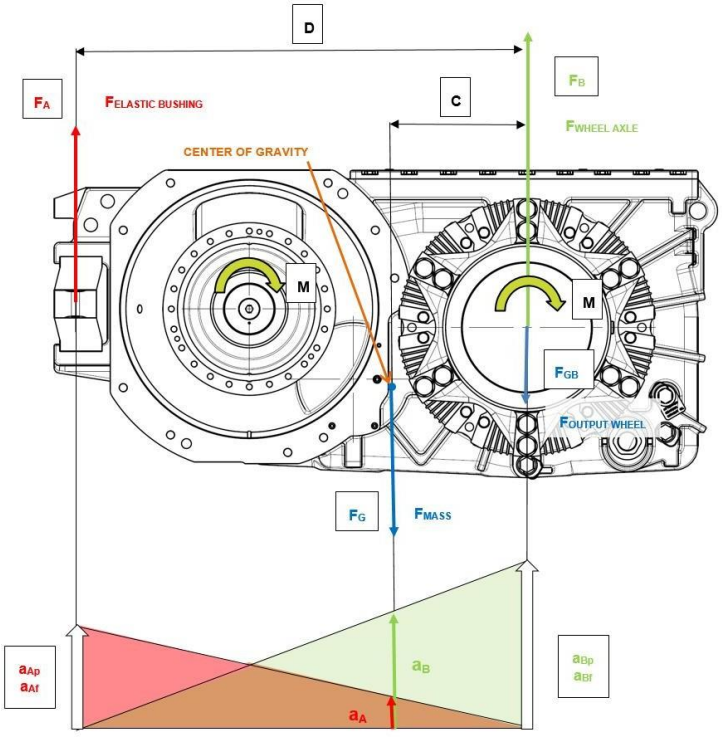

Fig. 4.26. Diagram of load distribution, where F_A is the force in elastic bushings; F_B is the force in wheel axle; and F_G is the force of gravity.

A radial displacement of 0.1575 mm is applied on hub bore diameter nodes. The corresponding total load is applied on holes for bolts in arms. The coupling assembly has to transmit an output torque of 72 580.6 Nm (input short circuit torque of 11 000 Nm). Motor tractive torque is 2 702 Nm, which corresponds to 17 828 Nm on coupling, as shown in Table 4.8.

Table 4.8

Load parameters of rubber wedge coupling

Input torque [Nm]	Ratio *i* [1]	Output Ttrque [Nm]	Diameter [mm]	Tangential force from 1 rubber wedge [N]
11 000	6.598	72 580.6	383.7	63 053
2702	6.598	17 828	383.7	15 488

Maximal overlap is used for analyses. In reality, this value is decreased by the influence of shaft and roughness.

Load case 1: Maximum von Mises stress 333 Mpa. Safety factor to yield point: 1.26.

Load case 2: Maximum von Mises stress 345 Mpa. Safety factor to yield point: 1.22.

Load case 3: Maximum von Mises stress 330 Mpa. Safety factor to yield point: 1.27.

Tractive torque has negligible influence on stress, as shown in Table 4.9 and Figs. 4.27, 4.28 and 4.29.

Table 4.9

Definition of the Safety Factor Index relative to the criteria

Load case	Type of analysis	Stress [MPa]	Safety [1]	Safety criteria
LC1	static	333	To yield point: $k = \frac{420}{333} = 1.26$ To strength limit: $333\ MPa < 700\ MPa$ Strain: $\varepsilon = 0.161\ \%$	$\sigma < R_m$ $\varepsilon < 4\ \%$
LC12	static	345	To yield point: $k = \frac{420}{345} = 1.22$ To strength limit: $333\ MPa < 700\ MPa$ Strain: $\varepsilon = 0.161\ \%$	$\sigma < R_m$ $\varepsilon < 4\ \%$
LC3	fatigue	330	To yield point: $k = \frac{420}{330} = 1.27$ To strength limit: $333\ MPa < 700\ MPa$ Strain: $\varepsilon = 0.161\ \%$	Min 1.0

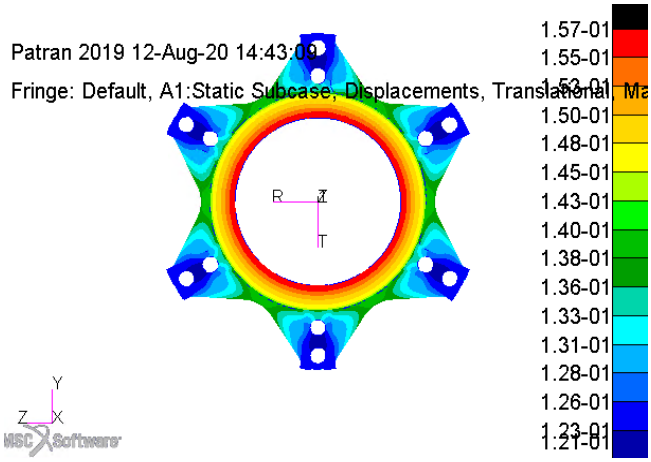

Fig. 4.27. Load case 1 - maximal fit S_{max}; displacement [mm].

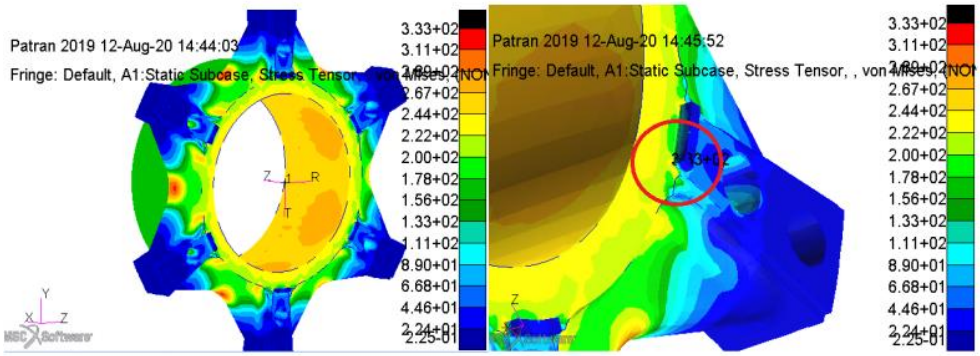

Fig. 4.28. Load case 1 - maximal fit S_{max}; von Mises stress [MPa].

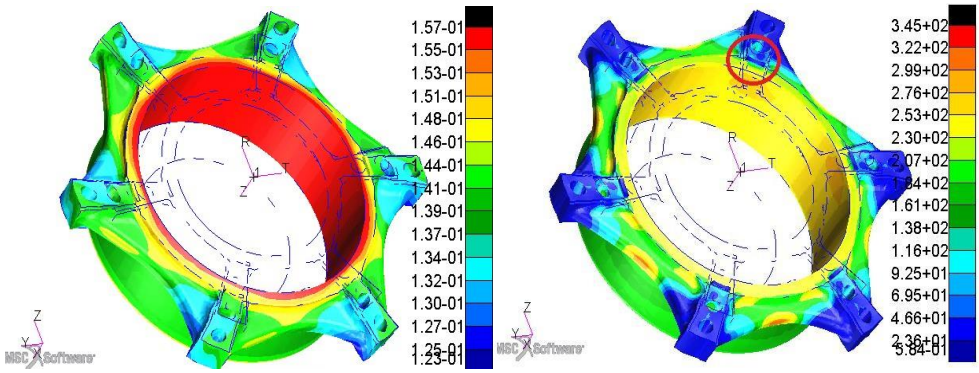

Fig. 4.29. Load case 2 - maximal fit S_{max} + Short circuit torque; (left) displacement [mm], (right) von Mises stress [MPa].

For model of the housing are TET10 elements used. The connection nodes are restrained in T_x, T_y, T_z, R_x, R_y, R_z. Load is applied on surfaces. See on Figs. 4.30, 4.31, 4.32, 4.33 and Table 4.10.

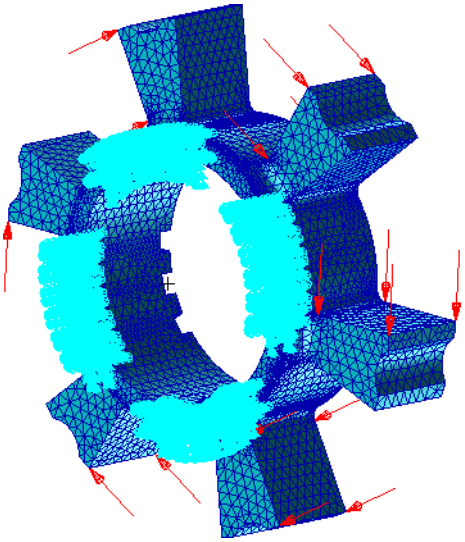

Fig. 4.30. TET 10 Fenite Element model.

Table 4.10

Load cases

Load case 1 (LC1)	Short circuit torque	static calculation	72 580 Nm
Load case 2 (LC2)	Tractive torque	fatigue calculation	17 828 Nm

Load case 1 - Short circuit torque is used for static calculation. In this extreme load case is stress compared to the strength limit. Small plastic deformation can occur, but without influence on the safety and reliability. Maximal total strain is 0.28 %.

Load case 2 – Tractive torque value is used for fatigue calculation. Safety to fatigue limit 1.79 is sufficient for safe operation.

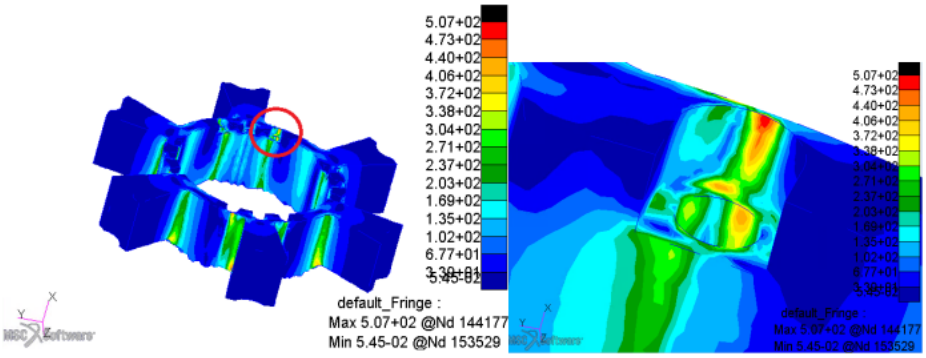

Fig. 4.31. LC 1 – Short circuit torque – static - Von Mises Stress [MPa].

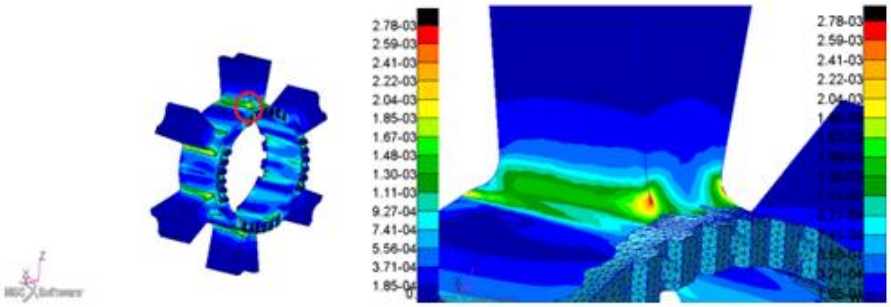

Fig. 4.32. LC 1 – Short circuit torque – static - Strain tensor.

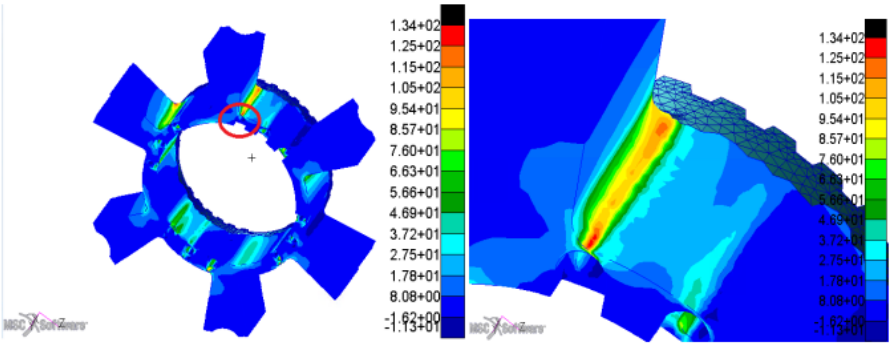

Fig. 4.33. LC 2 – Tractive torque – fatigue - Max Principal Stress [MPa].

Load case 1 – Extreme load, short circuit torque. Acting force is used. The max. von Mises stress in critical area is 163 MPa. Safety to yield point is 1.53.

Load case 2 – Tractive torque and fatigue shocks loading is assumed as fatigue load, alternating type (number of cycles minimum 1.10^7). Safety to fatigue failure is 1.31.

All safeties are in the limit and structure will withstand the designed load.

4.5. Conclusions and Results

The chapter presents an analysis of the compliance of the MGU design with the minimum permissible stresses in accordance with *ISO 10816* for permissible values of the safety factor. The determined places of maximum stress concentration are decisive for further analysis of the vibration state of the MGU with changing design and energy parameters.

It should be noted that the technology for manufacturing traction motors provides for the possibility of manufacturing frames not in the form of cast parts but in the form of charge-welded structures. This fact does not affect the applicability of the calculation method due to the use of a three-dimensional design software for both cases.

CHAPTER 5. INFLUENCE OF THE TECHNICAL CONDITION OF THE MGU ON THE VIBRATION STABILITY AND TRACTION-ENERGY CHARACTERISTICS OF THE MOTOR

5.1. Dynamic Traction Indicators

There are two main types of asynchronous motor control – scalar and vector. To improve the precision, dynamic and energy characteristics of the electric drive, as well as for a wider range of rotor speed control and the ability to maintain a constant speed with a changing load torque, the vector method of asynchronous motor control is used. However, an electric motor with this control method has a complex mathematical description, which is simplified by using various coordinate systems.

To simplify the mathematical description, a transition is made from a three-phase asynchronous motor (AM) circuit in the axes *a, b, c* to a two-phase AM circuit in the *u, v* axes. When switching to a two-phase coordinate system, three coordinate axes are transformed into two orthogonal *u, v* axes. The rotor axis u coincides with the original a axis, and the v axis is orthogonal to the u axis. The resulting rotor current vector $\vec{i_2}$ uniquely characterizes the instantaneous values of the rotor currents i_{2i}, i_{2u}, i_{2v} along the *u, v* axes flowing under the influence of the voltages u_{2u}, u_{2v} applied to the windings u_2, v_2. The stator axis α coincides with the initial axis a_1, and the β axis is orthogonal to the α axis. The resulting stator flux linkage vector ψ_1 uniquely characterizes the instantaneous values of the flux linkages ψ_{1a}, $\psi_{1\beta}$ as its shown on Fig. 5.1 [133].

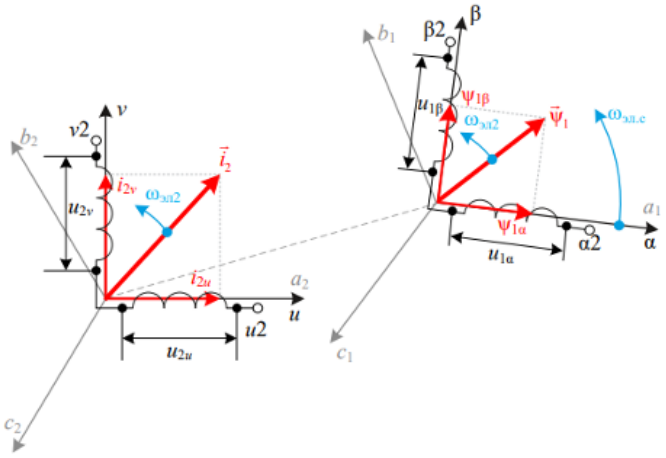

Fig. 5.1. AM diagram in a two-phase fixed coordinate system in the axes *u, v* and *α, β*.

To perform the transformations described above, the direct Clarke and Park transformation is used. The Clarke transformation carries out the transition of phase voltages from the natural three-phase coordinate system *A, B, C* to the orthogonal synchronous coordinate system *α, β* (5.1-5.2). The direct Park transformation is used to transform from a two-phase stationary coordinate system to a rotating coordinate system oriented along the rotor flux linkage vector (5.2-5.3). It is worth considering the condition of combining the real axis of the rotating

coordinate system with the rotor flux linkage vector. Then the projection of the rotor flux linkage on the u axis will be equal to the modulus of this flux linkage, and the projection on the v axis will be zero.

$$\begin{cases} \vec{u}_1 = R_1\vec{i}_1 + \frac{d\vec{\psi}_1}{dt} + jw_k\vec{\psi}_1 \\ 0 = R_2\vec{i}_2 + \frac{d\vec{\psi}_2}{dt} + j(w_k - Z_p w_2)\vec{\psi}_2 \\ \vec{\psi}_1 = \vec{i}_1 L_1 + \vec{i}_2 L_m \\ \vec{\psi}_2 = \vec{i}_1 L_m + \vec{i}_2 L_2 \\ M_{\partial в} = \frac{3}{2} Z_p \cdot k_2 \cdot \mathrm{mod}(\vec{\psi}_2 \times \vec{i}_1) \\ J_{\partial в}\frac{dw_2}{dt} = M_{\partial в} - M_н \end{cases} \quad (5.1)$$

$$\begin{cases} u_{1\alpha} = r_1 i_{1\alpha} + L_1^{пр}\frac{di_{1\alpha}}{dt} - \frac{k_2}{T_2}\psi_{2\alpha} - k_2 Z_p w_2 \psi_{2\beta} \\ u_{1\beta} = r_1 i_{1\beta} + L_1^{пр}\frac{di_{1\beta}}{dt} - \frac{k_2}{T_2}\psi_{2\beta} + k_2 Z_p w_2 \psi_{2\alpha} \\ 0 = -k_2 R_2 i_{1\alpha} + \frac{\bar{\psi}_{2\alpha}}{T_2} + \frac{d\bar{\psi}_{2\alpha}}{dt} + Z_p w_2 \psi_{2\beta} \\ 0 = -k_2 R_2 i_{1\beta} + \frac{\psi_{2\beta}}{T_2} + \frac{d\psi_{2\alpha}}{dt} - Z_p w_2 \psi_{2\alpha} \\ M_{\partial в} = \frac{3}{2} Z_p \cdot k_2 \cdot (\psi_{2\alpha} i_{1\beta} - \psi_{2\beta} i_{1\alpha}) \\ J_{\partial в}\frac{dw_2}{dt} = M_{\partial в} - M_н \end{cases} \quad (5.2)$$

$$\begin{cases} \frac{di_{1u}}{dt} = -\frac{i_{1u}}{T_1} - j\omega_к i_{1u} + \frac{k_2}{T_2 L_1^{пр}}\psi_{2u} + Z_p\omega\frac{k_2}{L_1^{пр}}\psi_{2v} + \frac{u_{1u}}{L_1^{пр}} \\ \frac{di_{1v}}{dt} = -\frac{i_{1v}}{T_1} - j\omega_к i_{1v} + \frac{k_2}{T_2 L_1^{пр}}\psi_{2v} + Z_p\omega\frac{k_2}{L_1^{пр}}\psi_{2u} + \frac{u_{1v}}{L_1^{пр}} \\ \frac{d\psi_{2u}}{dt} = -\frac{\psi_{2u}}{T_2} + \frac{k_2 L_2}{T_2} i_1 + (\omega_к - Z_p\omega)\psi_{2v} \\ \frac{d\psi_{2v}}{dt} = \frac{\psi_{2v}}{T_2} + \frac{k_2 L_2}{T_2} i_1 - (\omega_к - Z_p\omega)\psi_{2u} \\ \frac{d\omega}{dt} = \frac{1}{J_{\partial в}}(M_{\partial в} - M_c) \\ M_{\partial в} = \frac{3}{2} Z_p k_2 (\psi_{2u} i_{1v} - \psi_{2v} i_{1u}) \end{cases} \quad (5.3)$$

In the resulting system of equations (5.3), the expressions for currents contain cross-linkages for rotor flux linkage. To implement vector control, it is necessary to eliminate these cross-linkages. By modifying the expressions for the stator voltage components, it is possible to obtain a system of equations with decoupled control channels. Then the equivalent circuit of vector control will have the form shown in Fig. 5.2.

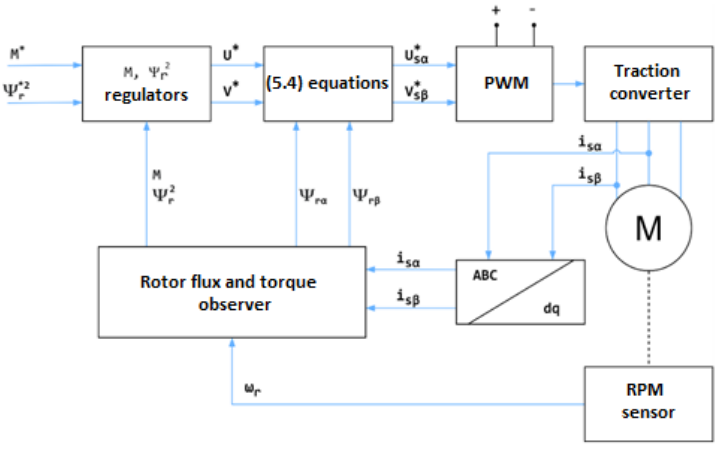

Fig. 5.2. Functional diagram of the asynchronous motor direct torque control system [134].

In accordance with the functional diagram, Fig. 5.2, control signals U^* and V^*, are generated at the outputs of the torque controllers, in accordance with which the voltage values on the converter are determined:

$$u_{s\alpha}^* = \frac{V^*\Psi_{r\alpha} - U^*\Psi_{r\beta}}{\Psi_r^2}$$
$$u_{s\beta}^* = \frac{U^*\Psi_{r\alpha} - V^*\Psi_{r\beta}}{\Psi_r^2} \quad . \tag{5.4}$$

The characteristics of the traction motor, obtained experimentally, to test its own vibration in the frequency range correspond to those presented in Fig. 5.3, Fig. 5.4, Fig. 5.5, Fig. 5.6, Fig. 5.7, Fig. 5.8, Fig. 5.9, Fig. 5.10, Fig. 5.11, Fig. 5.12, Fig. 5.13.

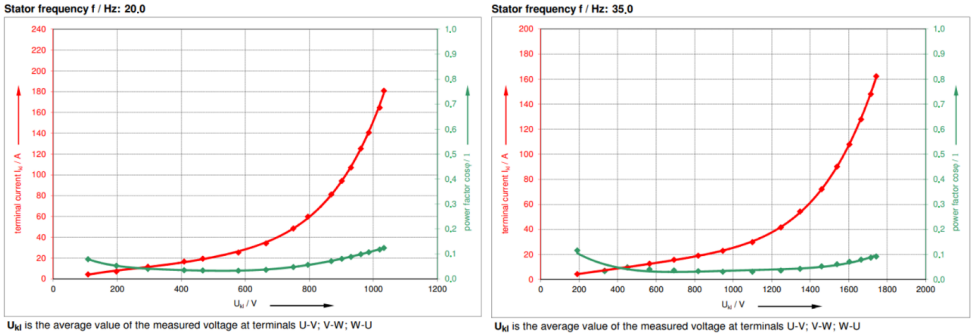

Fig. 5.3. No load test. Current and power factor versus voltage at 20 Hz and 35 Hz (*f* is the calculated average of the measured frequency values).

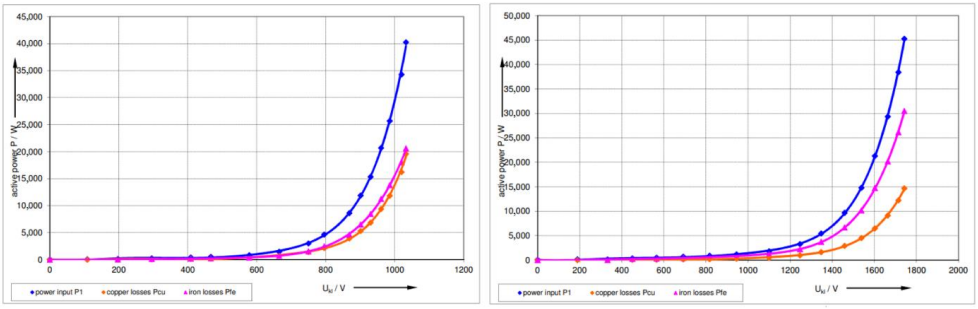

Fig. 5.4. Overview power versus voltage at 20 Hz and 35 Hz.

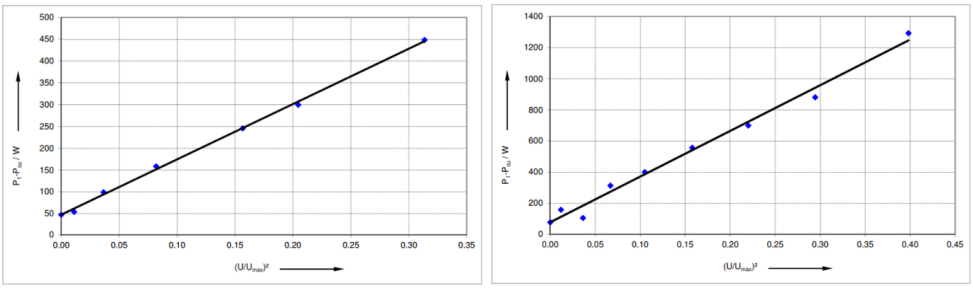

Fig. 5.5. Mechanical losses at 20 Hz and 35 Hz. The mechanical losses were determined by extrapolation of P_1-P_{Cu} at no load to 0 V. P_{mech} / *W*: 47 at 20 Hz point and P_{mech} / *W*: 77 at 35 Hz point

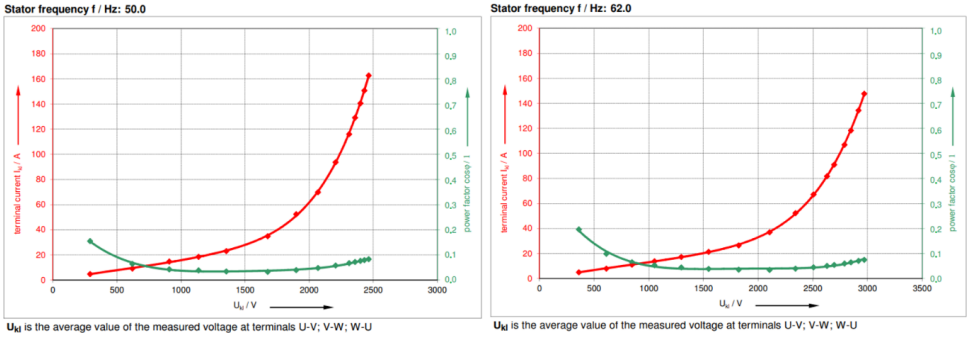

Fig. 5.6. No load test. Current and power factor versus voltage at 50 Hz and 62 Hz(*f* is the calculated average of the measured frequency values).

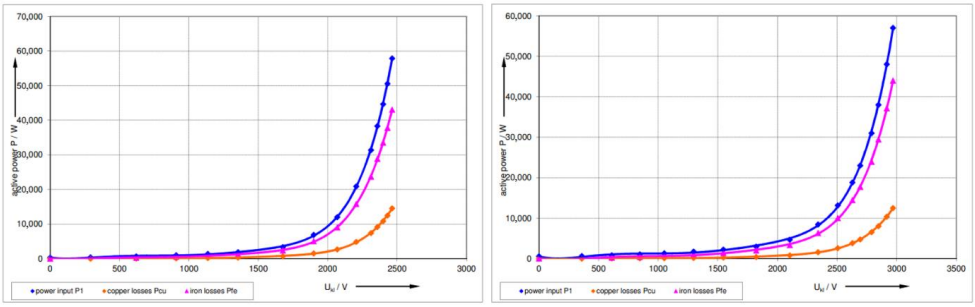

Fig. 5.7. Overview power versus voltage at 50 Hz and 62 Hz.

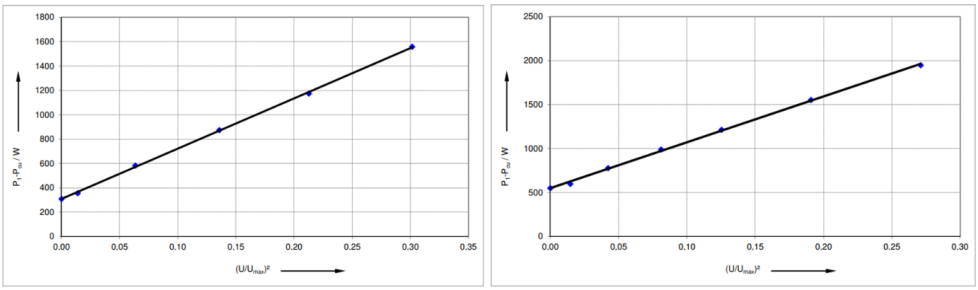

Fig. 5.8. Mechanical losses at 50 Hz and at 62 Hz. The mechanical losses were determined by extrapolation of P_1-P_{Cu} at no load to 0 V. P_{mech} / *W*: 308 at 50 Hz point and P_{mech} / *W*: 548 at 62 Hz point.

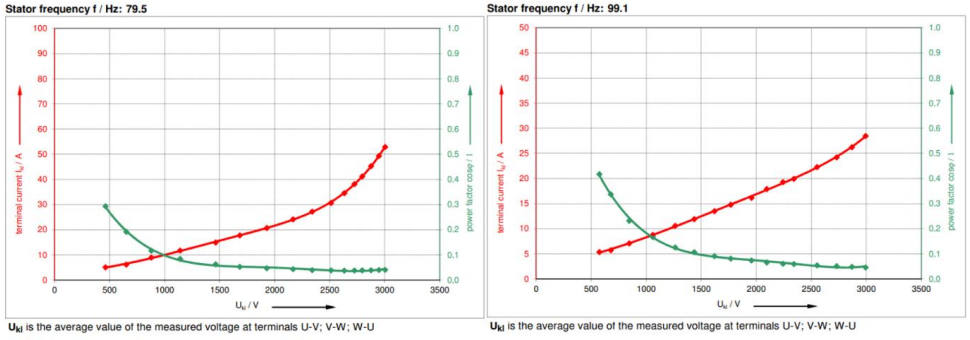

Fig. 5.9. No load test. Current and power factor versus voltage at 79.5 Hz and 99.1 Hz (*f* is the calculated average of the measured frequency values)

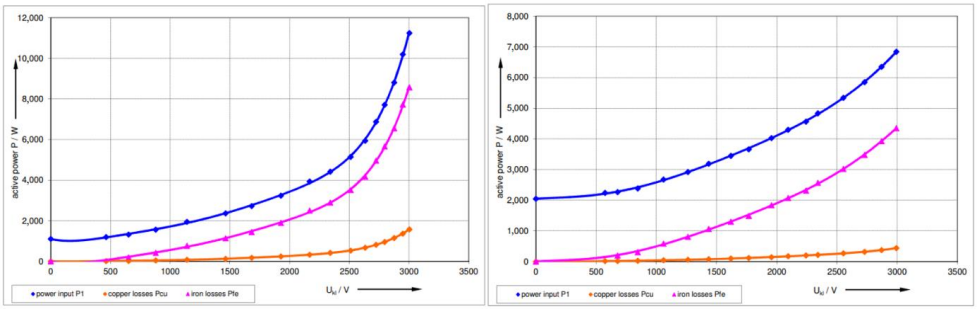

Fig. 5.10. Overview power versus voltage at 79.5 Hz and 99.1 Hz.

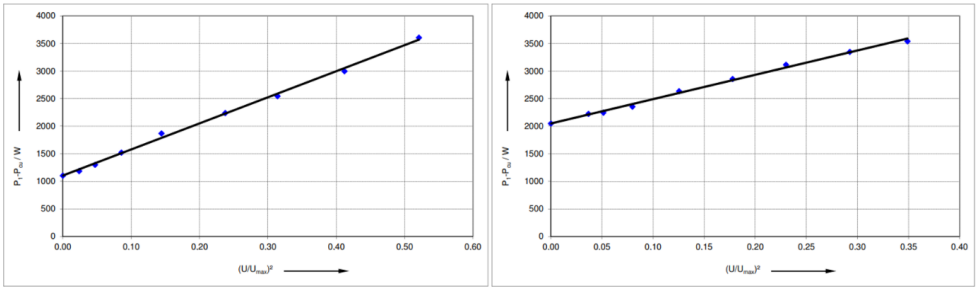

Fig. 5.11. Mechanical losses at 79.5 Hz and 99.1 Hz. The mechanical losses were determined by extrapolation of P_1-P_{Cu} at no load to 0 V. P_{mech} / W: 1101 at 79.5 Hz point and Pmech / W: 2049 and 99.1 Hz point.

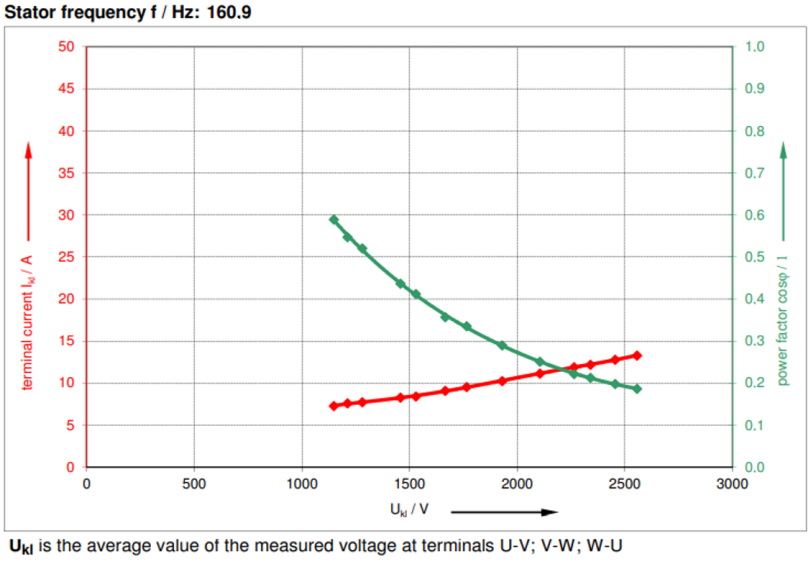

Fig. 5.12. No load test. Current and power factor versus voltage at 160.9 Hz (f is the calculated average of the measured frequency values).

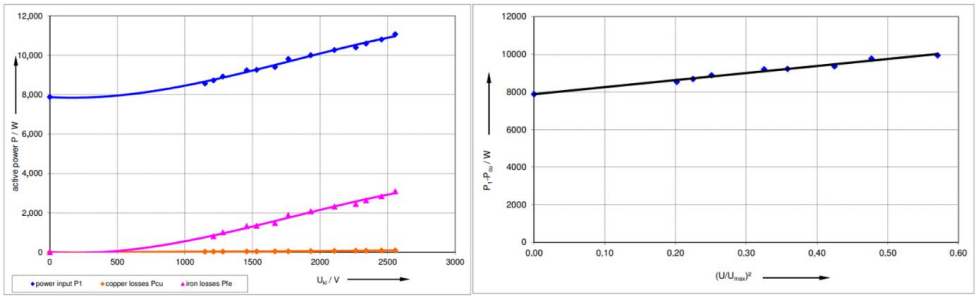

Fig. 5.13. Overview power versus voltage at 160.9 Hz and Mechanical losses at 160.9 Hz. The mechanical losses were determined by extrapolation of P_1-P_{Cu} at no load to 0 V. P_{mech} / W: 7881.

The characteristics of the traction motor, obtained experimentally to test its vibration activity and possible changes in energy characteristics under the load in the frequency range, are presented in Fig. 5.14, Fig. 5.15, Fig. 5.16, Fig. 5.17, Fig. 5.18, Fig. 5.19, Fig. 5.20, Fig. 5.21, Fig. 5.22, Fig. 5.23.

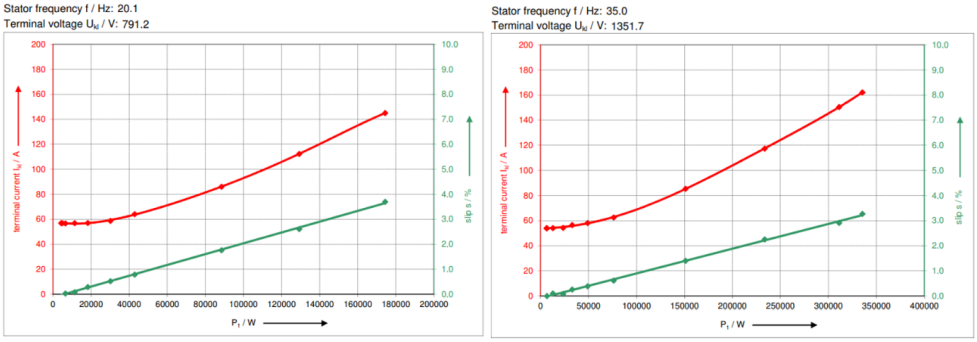

Fig. 5.14. Load characteristics. Terminal current and slip versus power at 20 Hz and 35 Hz.

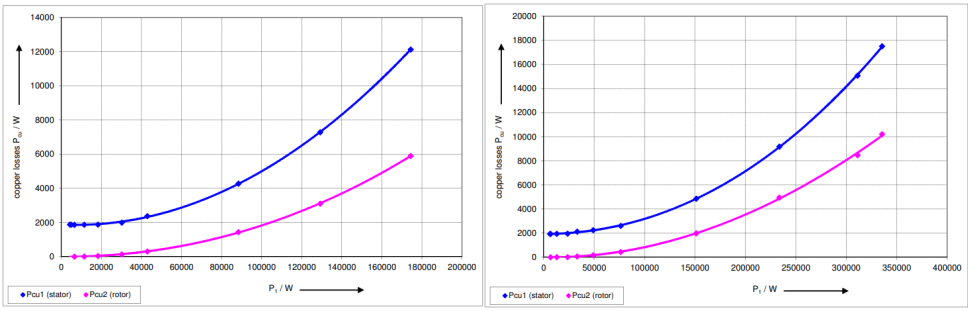

Fig. 5.15. Copper losses versus power at 20 Hz and 35 Hz.

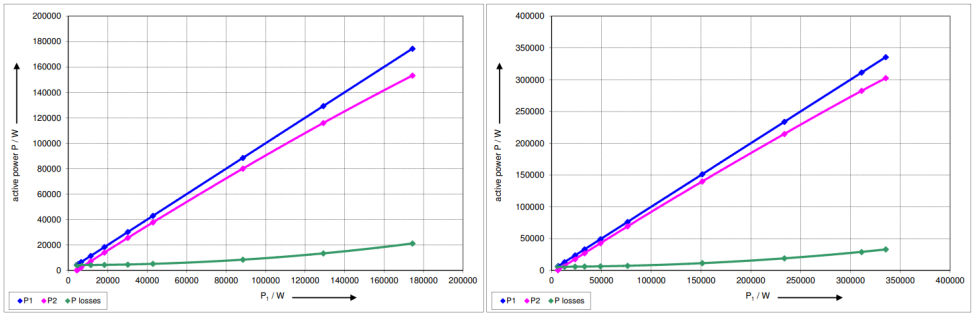

Fig. 5.16. Overview power at 20 Hz and 35 Hz.

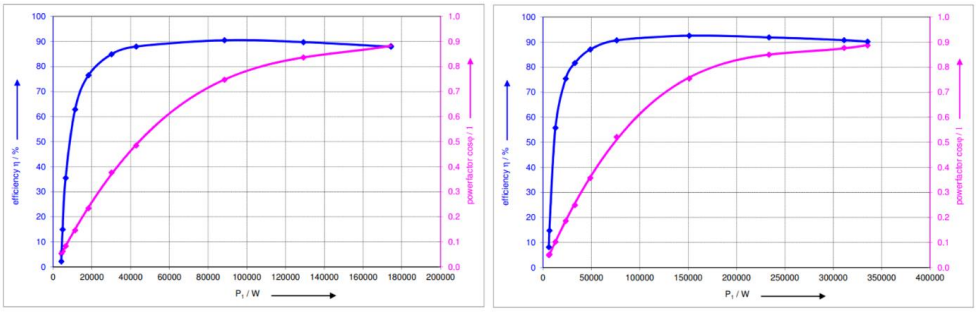

Fig. 5.17. Efficiency and power factor versus power at 20 Hz and 35 Hz.

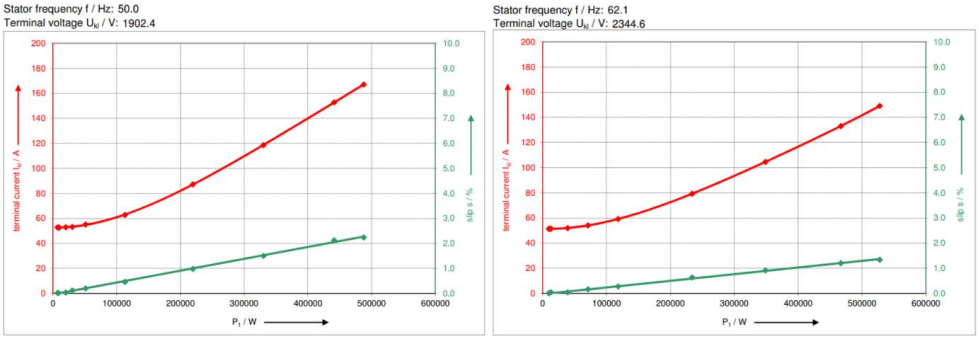

Fig. 5.18. Load characteristics. Terminal current and slip versus power at 50 and 62 Hz

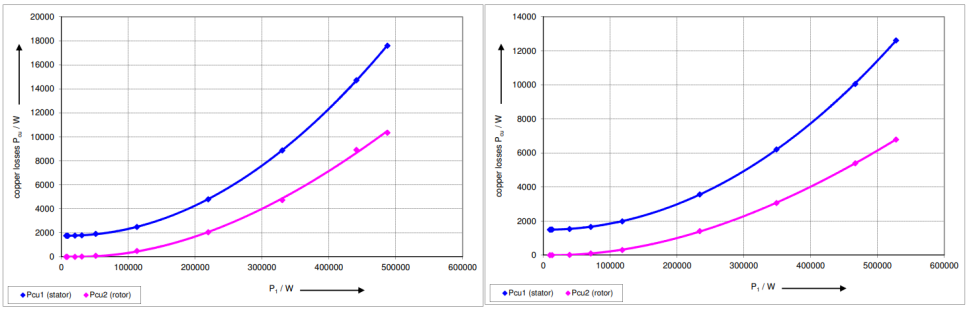

Fig. 5.19. Copper losses versus power at 50 Hz and 62 Hz.

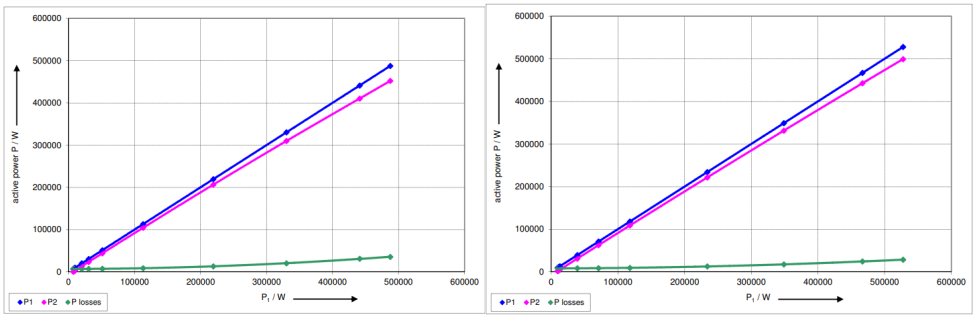

Fig. 5.20. Overview power at 50 Hz and 62 Hz.

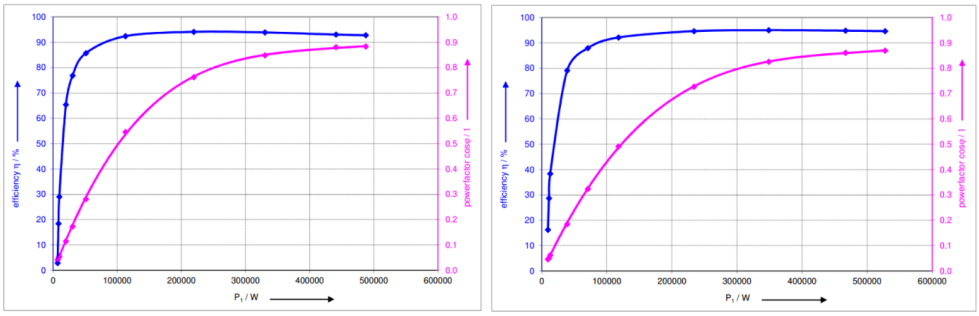

Fig. 5.21. Efficiency and power factor versus power at 50 Hz and 62 Hz.

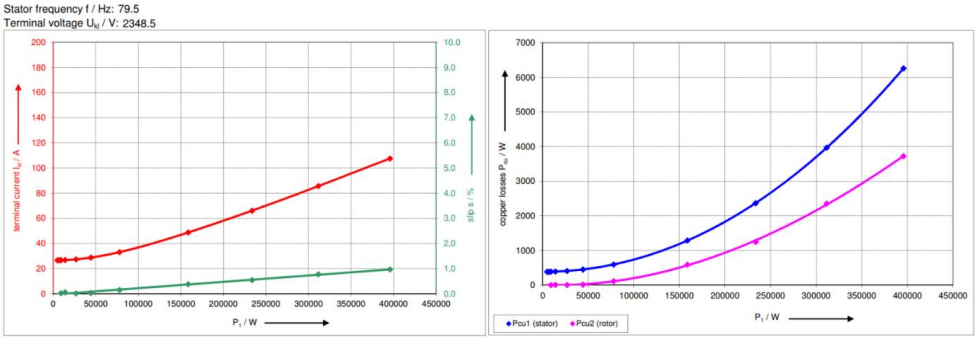

Fig. 5.22. Load characteristics. Terminal current and slip versus power and Copper losses versus power at 79.5 Hz.

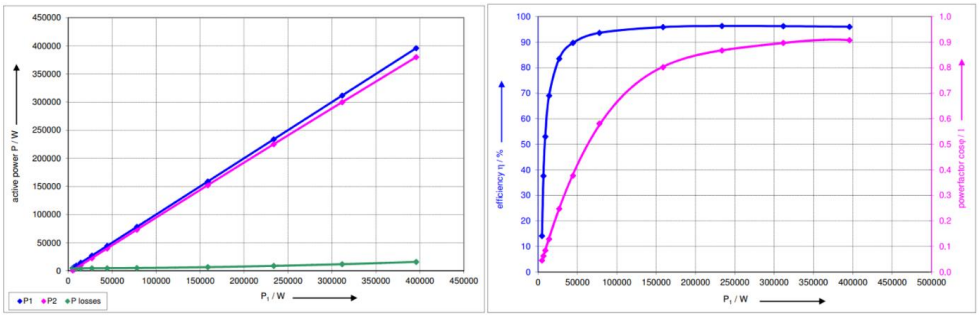

Fig. 5.23. Overview power and Efficiency and power factor versus power at 79.5 Hz.

For the 50 Hz point in unload and load for a serviceable (reference) traction MGU, the graphic data is presented in the Table 5.1 and 5.2.

Table 5.1

No load test data at 50 Hz

U_{kl}, V	I_{kl}, A	P_1, W	$Cos\ \varphi$	P_{Cu}	P_{Fe}
290.6	4.8	396	0.155	13	48
620.4	9.2	630	0.064	47	274
908.0	14.7	993	0.043	119	566
1136.6	18.6	1362	0.039	189	865
1353.2	23.1	1851	0.034	293	1249
1676.4	34.9	3323	0.033	669	2345
1898.6	52.4	6858	0.040	1507	5042
2068.8	70.0	12 026	0.048	2688	9030
2205.5	93.7	10 908	0.058	4825	15 774
2311.4	116.0	31 377	0.068	7389	23 679
2357.6	129.2	38 313	0.072	9164	28 841
2399.3	140.5	44 661	0.077	10 845	33 507
2430.4	150.7	50 553	0.080	12 477	37 768
2664.0	162.7	57 891	0.083	14 533	43 050

Table 5.2

Load characteristics data at 50 Hz (reference rotor)

P_1, W	I_{kl}, A	$Cos\ \varphi$	P_{Cu_1}, W	P_{Cu_2}, W	P_{losses}, W
7077	52.8	0.041	1760	0	6874
8432	52.8	0.048	1760	0	6878
9675	52.6	0.055	1747	0	6870
20 054	52.9	0.115	1768	5	6949
30 396	53.3	0.173	1792	27	7046
51 234	55.1	0.281	1918	90	7339
112 890	62.8	0.546	2488	484	8612
219 388	87.2	0.762	4798	2047	13 018
330 238	118.6	0.848	8872	4732	20 331
441 159	152.7	0.880	14 716	8910	30 907
487 482	167.0	0.883	17 600	10 346	35 459

P_1, W	η, %	s, %	M_{calc}, Nm
204	2.9	0.01	1.3
1555	18.4	0.02	9.9
2805	29.0	0.02	17.9
13 105	65.3	0.04	83.4
23 349	76.8	0.12	148.8
43 895	85.7	0.20	280.0
104 278	92.4	0.46	667.0
206 370	94.1	0.98	1326.6
309 907	93.8	1.50	2003.3
410 252	93.0	2.12	2666.6
452 023	92.7	2.24	2940.7

5.2 The Relationship Between the Causes of Vibration and the Diagnosed Parameters

The running traction and energy parameters of the motor for determining the vibration activity of the MGU in the long-term mutual loading mode were determined using MATLAB/Simulink. The aim of the study is to determine the dependence of the vibration characteristics of the MGU simultaneously with the change in the energy characteristics of the motor to identify the causes of its non-compliance with the required parameters at the stage of acceptance tests.

The developed test method uses two frequency converters that perform double energy conversion. First, the voltage supplied from the network is rectified, smoothed, and then inverted to power the motors. The rectifiers are uncontrolled (diode bridge), and the inverters are controlled (IGBT transistors). Between the rectifiers and inverters there are DC links that are combined into one system. The implementation of the mutual load mode is carried out by setting different frequencies of the supply voltage on the tested electrical machines. In this case, one of the electrical machines operates in the motor mode and the other in the generator mode. The electrical energy generated by the generator is transmitted via the DC link to the motor. In this case, the energy required to compensate for losses in both machines is consumed from the network.

Two identical MGUs are used simultaneously during testing. Frequency converters are used as a control link instead of additional electric machines. Electric energy is transferred directly to the MGU under test and compared to circuits that provide electric energy transfer to the network, which reduces the impact of higher harmonics of currents and voltages on the network.

Reciprocal load implementation is possible at any difference in the supply voltage frequencies set on the frequency converters, in contrast to testing at industrial voltage frequency.

In accordance with *ISO 10816*, as part of the mechanical stability check of the product, it is advisable to conduct an autonomous check of the traction motor to determine its own vibration activity for at least one of the quantities specified in the standard [135]:

- vibration displacement, in micrometers (μm);
- vibration velocity, in millimeters per second (mm/s);
- vibration acceleration, in meters per second squared (m/s^2).

According to *ISO 10816*, the maximum measurable vibration level is up to 5 mm/s in the direction transverse to the output shaft and 2.5 mm/s in the direction along the output shaft.

All components must withstand vibration and impacts, sinusoidal vibration with a maximum acceleration amplitude of 150 m/s^2 in the frequency range of 0.5–100 Hz without damage.

It is assumed that the specified impact is exerted from the wheelset on the wedge clutch [136].

The test cycle and the completeness of the laboratory equipment are shown in Fig. 5.24.

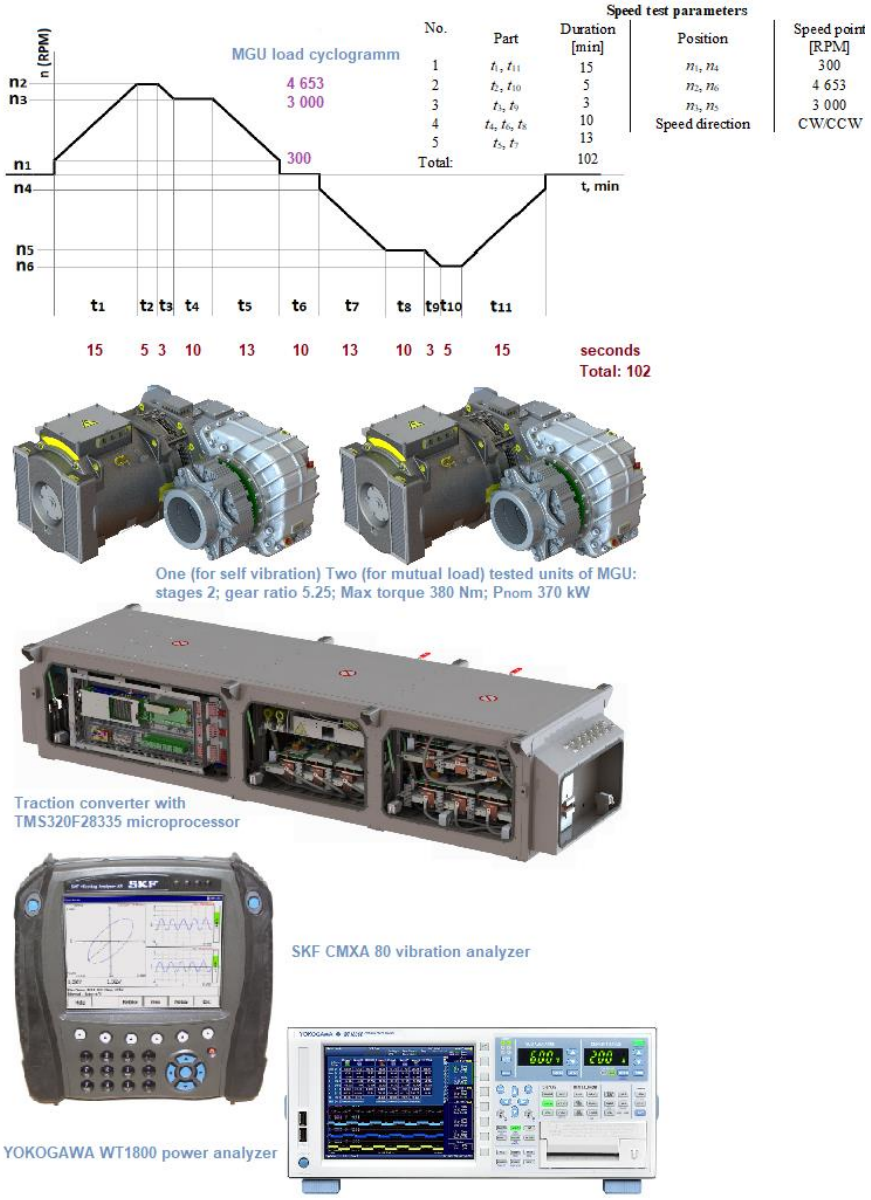

Fig. 5.24. The test cycle and the completeness of the laboratory equipment [115].

Based on the design assignment of the MGU, it corresponds to the S1 operating mode with a variable load value.

Using mathematical transformations, it is possible to obtain a linearized model equivalent to the traction asynchronous motor model for its further integration into the test rig control model, see Fig. 5.25. This makes it possible to use classical correction methods: the deep feedback method and subordinate control. Using these methods, it is possible to achieve an improvement in the static and dynamic characteristics of the system.

Undoubtedly, the rectangular step shape of the supply voltage can lead to a significant expansion of the spectrum of forces causing magnetic vibrations, which can significantly affect

the vibration activity of low-quality MGUs. Due to the precise debugging of the converter at the stage of setup work and further testing with a standard MGU, the negative effect of PWM can be excluded. The voltage and current readings of the oscilloscope are shown in Fig. 5.26.

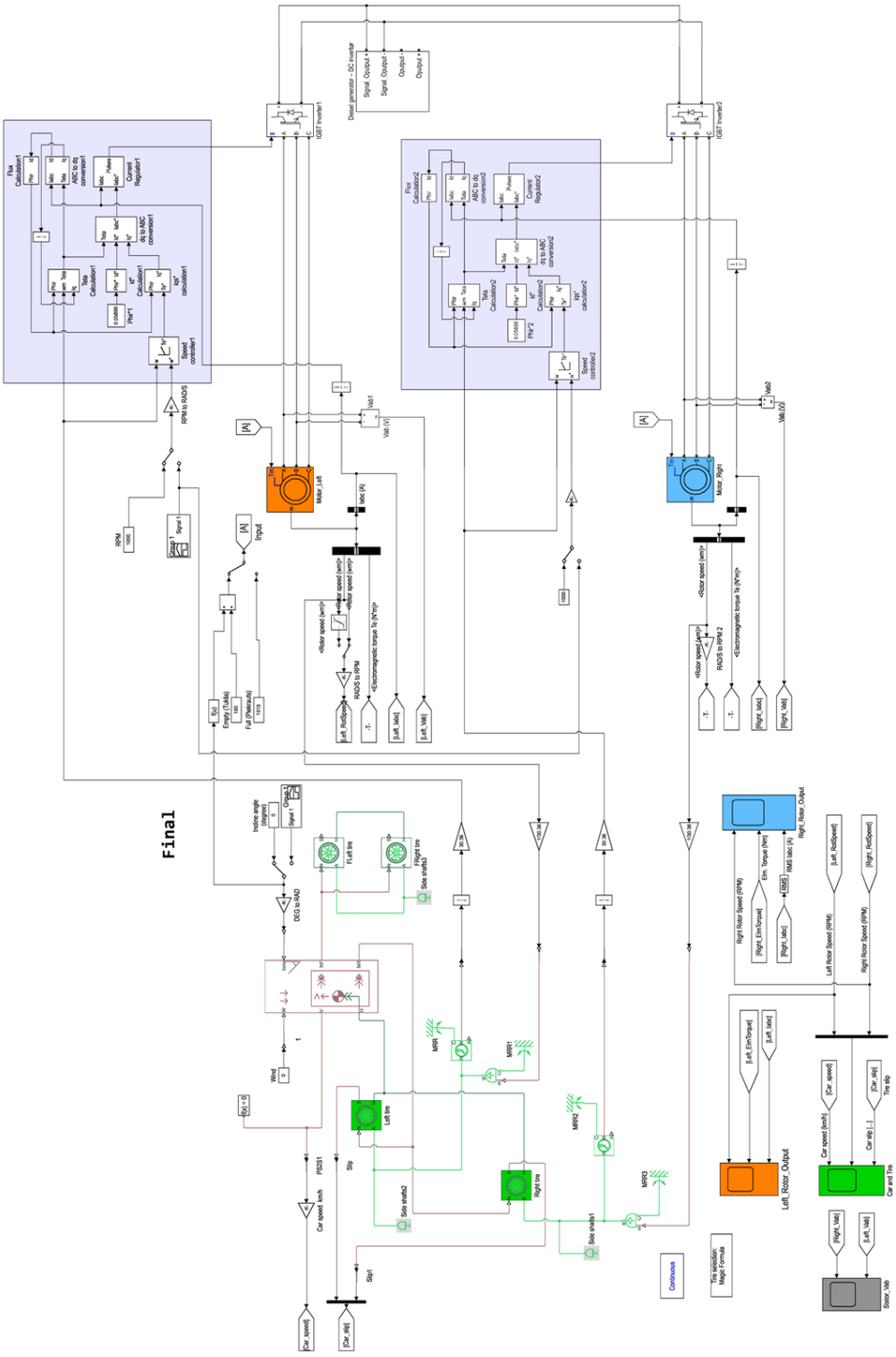

Fig. 5.25. Simulation bench model in the MATLAB Simulink system.

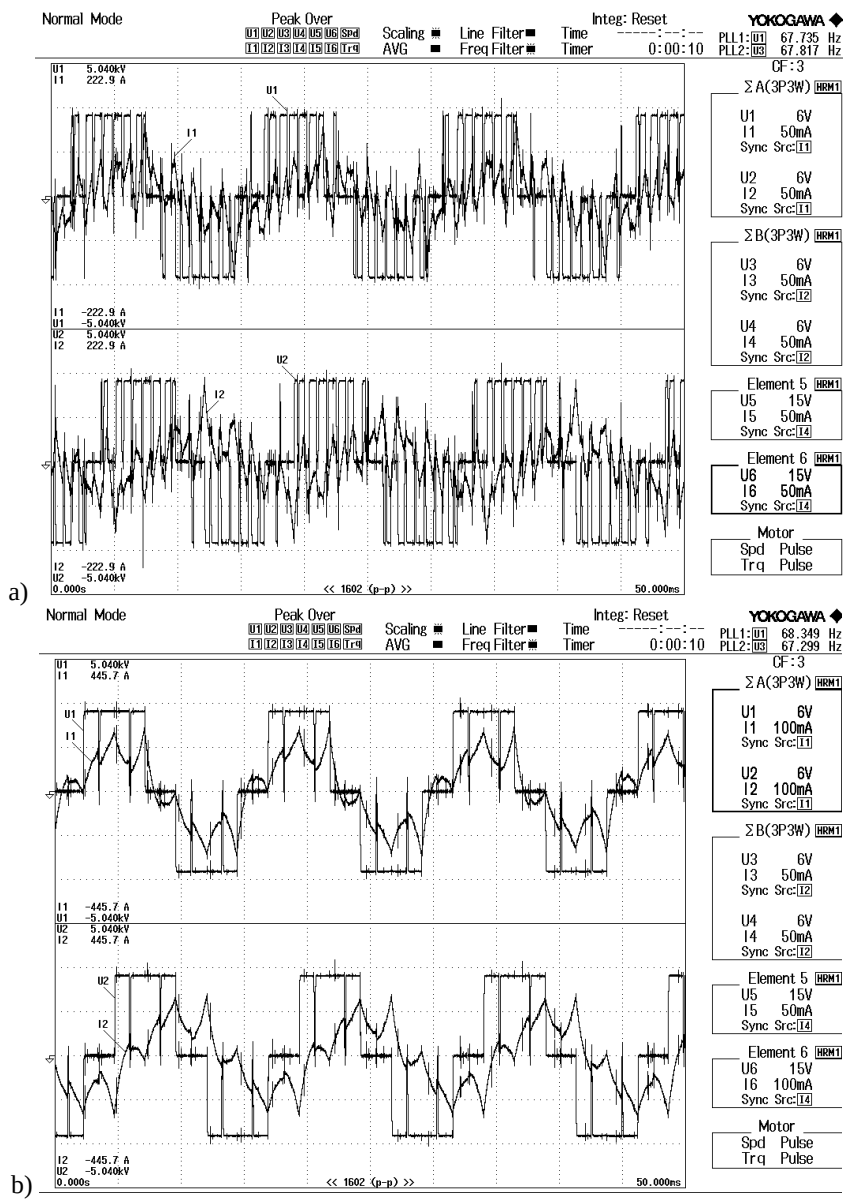

Fig. 5.26. Output signals of Voltage and Current from converter DC link a) unloaded motor b) nominal load mode.

The variable composition of the input and output data of the motor model is determined by its traction and energy characteristics obtained during the design calculation of the motor.

The motor torque is controlled by regulating the stator current components. In turn, the *d* and *q* components of the current are controlled using the stator voltage components (and, accordingly, also *d* and *q*) generated by the current controllers.

The measured and converted into the *dq* system signals from the phase current sensors are used as currents for calculating the compensation components. To eliminate (compensate) for cross-connections, the compensation components are summed with the components of the stator voltage vectors obtained at the output of the current controllers.

Further, Fig. 5.27 and Fig. 5.28 show the vibration acceleration spectra for the nominal rotation speed of the MGU equal to 3000 min^{-1} in the idle mode with the MGU mechanically disconnected and in the mutual load mode. It is evident that the vibration disturbance characteristic clearly repeats the MGU loading cyclogram in modulus shown in Fig. 5.24.

When operating at nominal voltage, with increasing frequency, the amplitude of the stator current is limited by the growth of the inductive resistance of the motor. Consequently, with increasing frequency, the maximum torque achievable by the motor is also limited. The maximum torque that the motor is capable of providing depends on the frequency.

At frequencies below the nominal, the maximum torque increases. Its increase is limited by the overload torque, which is selected based on the required drive dynamics and the permissible current of the power converter.

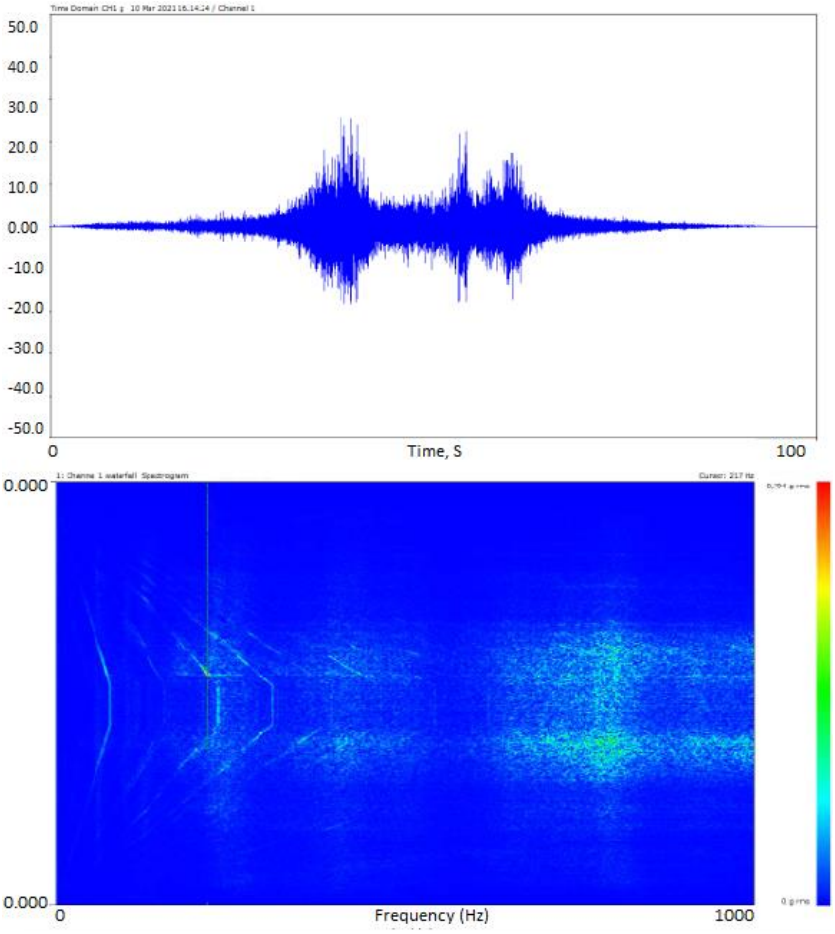

Fig. 5.27. The waveform and waterfall spectrogram at the rotor speed of nominal velocity 3 000 min^{-1} in Y–axis direction in unloaded mode.

The spectral analysis results were obtained using the fast Fourier transform. The decomposition of the vibration signature leads to motor speed-dependent orders, speed-independent components, and speed-related non-zero harmonics. The last two components are due to the inverter [115].

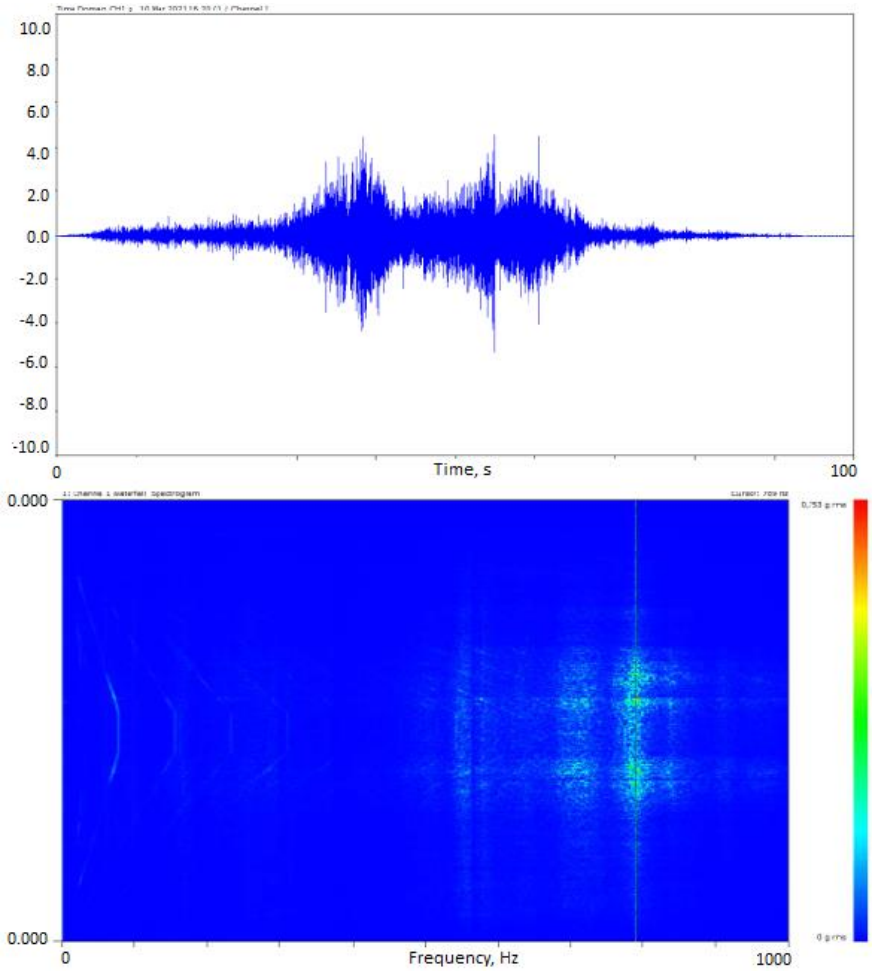

Fig. 5.28. The waveform and waterfall spectrogram at the rotor speed of nominal velocity 3 000 min^{-1} in Y–axis direction in mutual load mode.

Any mechanical structure has its own frequencies of mechanical resonances, at which the vibration amplitudes of both the entire structure and its components increase sharply when the frequency of external influences coincides with its own resonance frequencies.

The example presented below considers a case of deviation from the production technology, identified using the methodology presented in the dissertation research. Fig. 5.29 shows a clear resonance of the MGU.

The graph clearly shows two zones of resonance occurrence. The first zone has a very high amplitude of mechanical vibrations associated with vibrations of the entire mechanical structure. After turning off the power supply, sharp vibrations occur when the motor shaft speed decreases. In this range, when the motor speed coincides with the mechanical resonance frequency, the structure may be destroyed. The second resonance zone is associated with vibrations of individual mechanical elements.

When the rotor speed decreases in the coasting mode, the vibration cannot depend on the PWM of the traction converter control system and is not associated with the load on the MGU. At the same time, in the coasting mode, the possible presence of resonance can be determined.

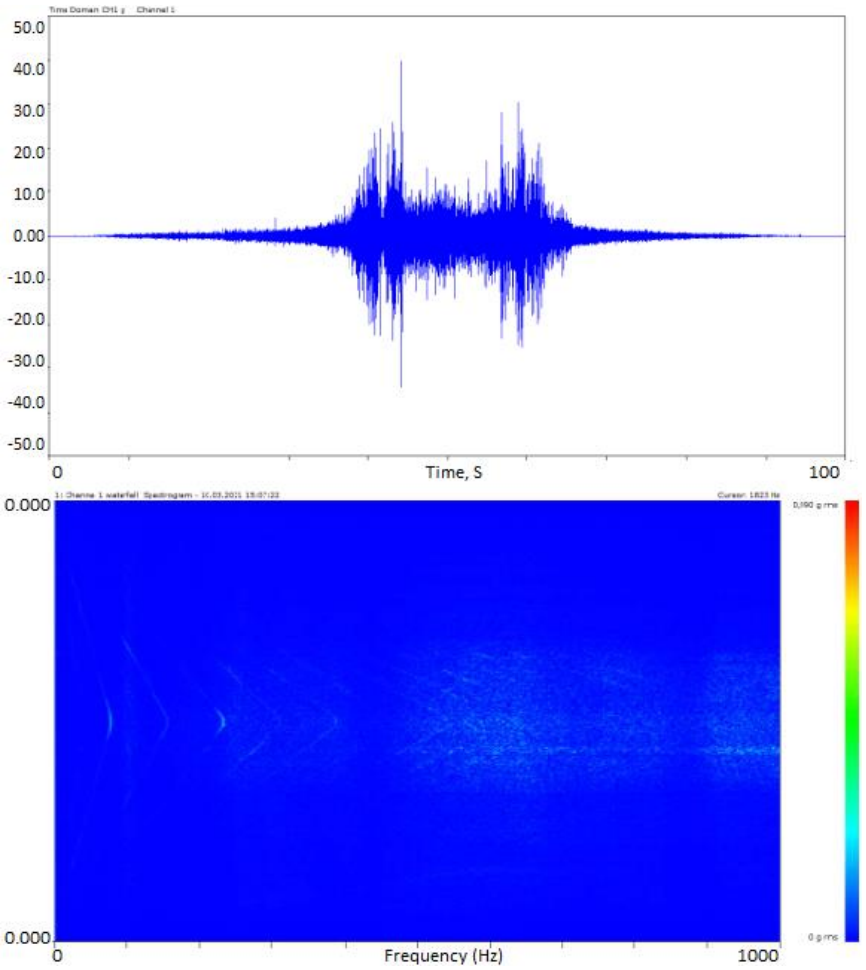

Fig. 5.29. The waveform of the vibration velocity at continuous speed of 3 000 min^{-1}.

For the assumptions put forward in the previous chapters about the role of the geometry of the bearing mounting holes in the shield and the coaxiality of the intermediate flange of the MGU and the bearing cite, the MGU was disassembled. As a result of determining the possible causes of increased vibration, a violation of the technology for processing the bearing shield and the flange of the MGU was revealed in terms of the displacement of the centers of the centers of both elements [120].

At the same time, the energy parameters were recalculated relative to the oscillograms recorded by the converter; they can be seen in Figs. 5.30 and 5.31. The presented example is given for one point equal to 50 Hz from the entire sample of the MGU test speed range.

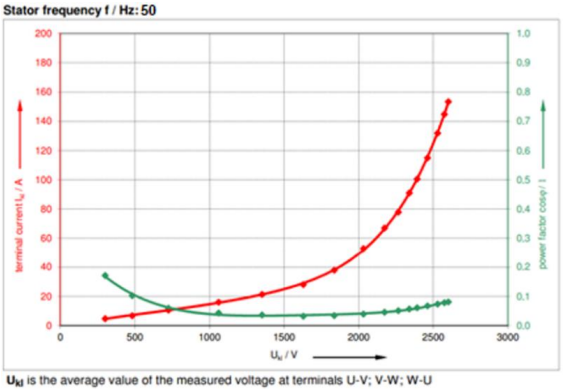

Fig. 5.30. No load test. Current and power factor versus voltage at 50 Hz.

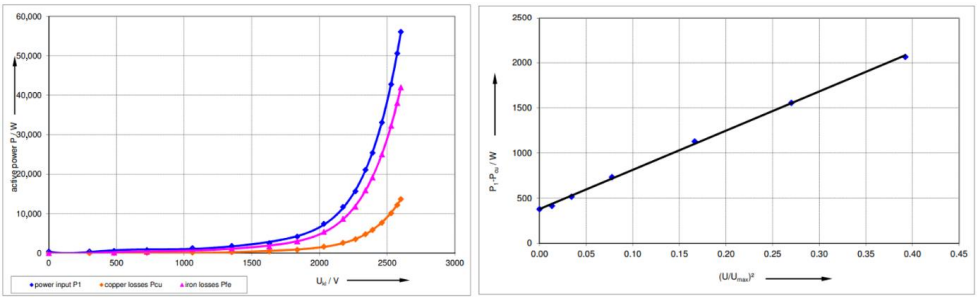

Fig. 5.31. Overview power versus voltage and Mechanical losses at 50 Hz. The mechanical losses were determined by extrapolation of P_1-P_{Cu} at no load to 0 V. P_{mech} / W: 378.

The vibration velocity values recorded during the experiment in the direction of the Y-axis, i.e., along the shaft axis, are several times higher than the values, the limit of which is specified in *ISO 10816* at 2.8 mm/s, both for the nominal and maximum value of rotor rotation. In addition to the given values, the vibration activity level of the MGU was recorded at 21 points and in three planes, both from the side of the motor support shield and from the side of the 1st stage bearing of the traction gearbox.

In an asynchronous motor, the speed is inversely proportional to the load, but when it is transmitted through a gearbox, a certain speed fluctuation is observed. When the rotational speed of the MGU rotor-shaft system increases from 3000 min^{-1} to 4653 min^{-1}, the vibration velocity values at the control points increase.

Vibration activity of the middle gears of the gear is less informative due to the fact that it can be caused by an obvious defect of the gear mechanism of the gear, such as misalignment or defects of the contact surface. In turn, the consequence of most defects is impacts of surfaces against each other or pulsed jumps in the load on the elements transmitting the torque to the driven shaft (rotor). Then, the load jumps are transmitted to the bearings of the mechanical transmission and excitation of pulse vibration in them [117].

The description of the load and possible wear options for the bearing mounting holes given in Chapters 3 and 4, and the resulting changes in the energy parameters of the motor, can be better represented by the misalignment of the motor bearing shield and the flange connecting the motor and gearbox. The level of vibration activity is fixed on the Y axis, so it is reasonable to assume the action of tangential forces arising in the MMF [119], [120].

A feature of the action of oscillatory forces of both electromagnetic and electrodynamic nature is their spatial wave character. In defect-free motors, the oscillatory forces (radial and tangential) acting on the rotor are zero. The tangential electrodynamic forces acting on the stator are also zero. Low-order electromagnetic radial oscillatory forces bend the stator, creating a wave of radial oscillations of double frequency and double spatial order.

The reliability of the electromagnetic system of the motor depends on the symmetry of the magnetic field, determined by the symmetry of the windings, the symmetry of the air gaps between the rotor and the stator, the equality of the magnetomotive forces of the windings, as well as on the state of fastening of the machine elements and the insulation of the electrical windings. Asymmetry of air gaps in the motor leads to the appearance of electromagnetic forces between the rotor and stator in the area of reduced gap, overloading the bearings and reducing their service life, and in the same area, magnetic saturation of the magnetic circuit teeth occurs, along which the magnetic flux bypasses the turns of the electric motor winding. The vibration level is manifested at the frequency of electromagnetic forces and at the frequency of rotation of the magnetic field in the gap. Figs. 5.32 and 5.33 show the general appearance of the MGU device on a platform with a spring suspension.

Fig. 5.32. MGU placement on the test platform to determine its own vibration.

Fig. 5.33. MGU placement on the test platform under mutual load.

The magnitude of the components of the vibrations of the MGU depends on the magnitude of the oscillatory forces and on the rigidity of the oscillatory system. Large oscillatory forces are electromagnetic, which act between the rotor and the stator in the radial direction, i.e., bend the machine body in accordance with the complex spatial shape of the magnetic field. The shape of the magnetic field and the deformation of the stator have angular symmetry and are characterized by the order of oscillations, which is equal to the number of spatial waves that fit on the length of the circumference of the motor stator.

When the electromagnetic system is defective, an asymmetry of the magnetic field in the air gap occurs, and first-order magnetic forces begin to act, shifting the rotor relative to the stator. Such a shift leads to the fact that the axial forces, trying to return the rotor to the neutral position, cause significant axial vibration at the frequency of the power supply network or at the frequency of rotation of the rotor, depending on the type of friction in the obstacle to axial displacement.

For the case of mutual loading, the resulting power, losses, power factor and efficiency of the drive were also obtained by oscillography, which can be seen in Figs. 5.34 and 5.35.

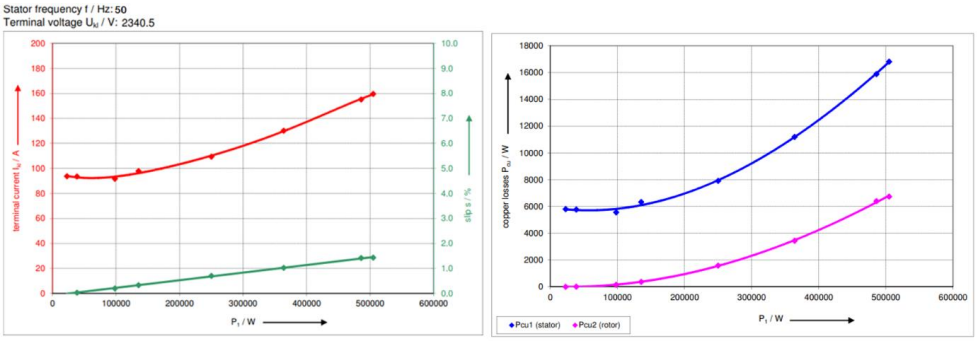

Fig. 5.34. Load characteristics. Terminal current and slip versus power and Copper losses versus power at 50 Hz.

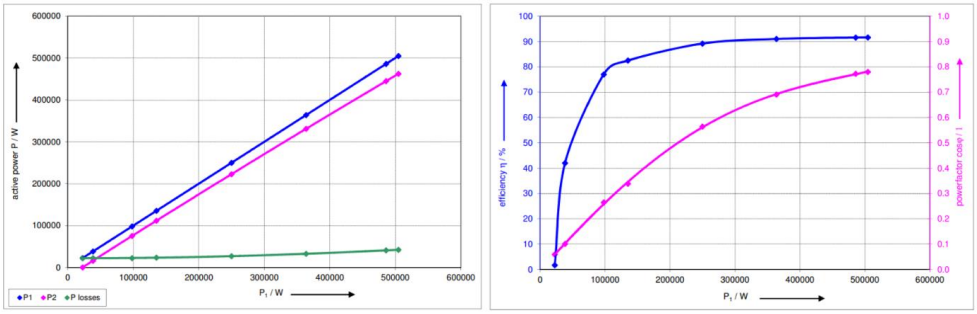

Fig. 5.35. Overview and Efficiency and power factor versus power at 50 Hz.

It is evident that with the increase of the vibration velocity value in the vertical direction Y, when measuring it on the bearing shield and the flange of the MGU in the idle mode, under load, and also, which is most informative, in the rotor run-out mode, the influence of the misalignment of the MGU support structures, the shaft displacement relative to the axis and, as a consequence, there is the change of the air gap. From the conducted study, it is evident that the change of the air gap uniformity is most negatively expressed in the increase of mechanical losses and the decrease of slip, more than 10 % decrease in the power factor of the drive, and together with it the efficiency of the drive as a whole. The purpose of the study was to determine the possibility of using the MGU vibration activity indicator, which is a mandatory parameter when conducting acceptance tests of traction MGUs, as the main rejection feature, and taking into account the nature of the manifestation of vibration activity and its value – then as a determinant of poor quality of the MGU parts or its assembly.

RESULTS AND CONCLUSIONS

The Doctoral Thesis examines the possibilities of assessing the technical condition and readiness for the release of serially produced MGUs based on vibration strength tests and traction and energy indicators. When setting the tasks of the Thesis research, there was a requirement to implement the methodology in the flow production of the manufacturing enterprise and the adaptability of the methodology to the product line, and not to one specific product.

During the implementation of the methodology in production, about a hundred motor-gear units for rail transport were produced, which simultaneously increased its reliability during acceptance tests.

The developed methodology is based on the real features of the technological process of production, as well as on the real operating conditions of the equipment, considering the mechanical loads of the traction drive.

To determine the possible influence of electromagnetic phenomena from the traction drive on the vibration strength characteristics of the MGU with a subsequent change in the traction and energy parameters of the motor, a strength calculation of the structure was carried out with the definition of critical areas of maximum stresses, the safety margin of the structure was determined. The experiment determined the level of vibration activity of the MGU in a loaded mode.

The methodology was tested both on a reference MGU sample and on a sample that does not meet the requirements of the Technical Specifications of the product.

Thus, for MGUs, in which the geometry of the electric motor flange and the bearing shield ensures both the average position of the motor roller bearing, which is most favourable in terms of reducing vibration activity and the average position of the rotor and its symmetrical arrangement, a number of patterns have been established.

The determining factor in monitoring the traction-energy and vibration-resistant parameters of the MGU is the dynamics of the change in the vibration velocity level, and as a consequence, deterioration of slip, increase in mechanical losses, and a significant decrease in the power factor and efficiency. It has been established that vibration is continuous in time and corresponds to the spectrum of the broadband region.

A number of key regulatory documents prescribe monitoring of the overall vibration level in a standard frequency band – from 10 Hz to 1000 Hz. However, in most cases, one or more fault frequencies (frequencies at which vibration growth indicates the presence or development of a particular defect) are outside the monitored frequency range. Thus, even a significant increase in the amplitudes of the components at these frequencies does not lead to a change in the overall vibration level in the standard frequency band monitored in accordance with the requirements of regulatory documents. Faults that occur at frequencies outside the frequency range under consideration include a number of electromagnetic defects, such as air gap eccentricity, gear defects, etc.

The value of the overall vibration level is quite informative but characterizes the combined vibration activity of all the main components of the monitored unit – the degree of "balance" of the rotors, the quality of the alignment, the state of the support system, etc. Some defects do not always lead to a noticeable increase in the overall vibration level. To prevent emergency failures and timely detection of these types of faults, along with monitoring the general level, it is

necessary to analyze the vibration velocity spectrum measured in the transverse direction and in the vertical direction.

This study is a continuation of the study of the vibration activity of rotating electric machines and traction units, as the most information-intensive characteristic throughout the entire service life of the product during routine inspections and repair and restoration work of the rolling stock.

From the point of view of economic feasibility, it can be highlighted that the end customer of the drive is most often a wagon-building company, much less often a repair company, interested in receiving an already tested and ready-to-install product, preferably from one manufacturer, which significantly reduces the time, and accordingly, the cost of commissioning and running tests of electric trains. The proposed method for determining the causes of a malfunction of the MGU is focused specifically on the complete supply of an electric traction drive.

LIST OF REFERENCES

1. Holopainen T., Niiranen J., Jörg P., Andreo D. “Electric Motors and Drives in Torsional Vibration Analysis and Design”, Proceedings of the Forty-Second Turbomachinery Symposium, Houston, Texas, 2013.
2. Zhang T., Jin T., Zhou Z., Chen Z., Wang K. “Dynamic modeling of a metro vehicle considering the motor–gearbox transmission system under traction conditions”, Mechanical Sciences, Volume 13, Issue 2, 2022.
3. Vos P. “Railway Induced Vibration - State of the Art Report”, International union of railways, 2017.
4. Villot, M., Augis E., Guidou-Carter, C., Jean, P., Ropars, P., Bailhache, S. and Gallais, C. “Vibration emission from railway lines in tunnels – characterization and prediction”, International Journal of Rail Transportation, Volume 4, 2016.
5. Küsel M., E Brommundt E. “Wavy Wear Pattern on the Tread of Railway Wheels”, In: Popp, K., Schiehlen, W. (eds) System Dynamics and Long-Term Behaviour of Railway Vehicles, Track and Subgrade. Lecture Notes in Applied Mechanics, vol 6. Springer, Berlin, Heidelberg. https://doi.org/10.1007/978-3-540-45476-2_8, 2003.
6. ISO 13373-1:2002 - Condition monitoring and diagnostics of machines —Vibration condition monitoring — Part 1: General procedures, Edition 1, 2002.
7. ISO 15242-1:2015 - Rolling bearings — Measuring methods for vibration — Part 1: Fundamentals, Edition 2, 2015.
8. GOST 24346-80 - Vibration Terms and definitions, Moscow Standartinform, 2010.
9. ISO 20816-3:2022 - Mechanical vibration — Measurement and evaluation of machine vibration. Part 3: Industrial machinery with a power rating above 15 kW and operating speeds between 120 r/min and 30 000 r/min, Edition 1, 2022.
10. GOST 32106-2013 - Condition monitoring and diagnostics of machines. Hazardous equipment monitoring. Vibration generated by rotodynamic pump and compressor units, Moscow Standartinform, 2019.
11. ISO 20958:2013 - Condition monitoring and diagnostics of machine systems — Electrical signature analysis of three-phase induction motors, Edition 1, 2013.
12. ISO 13379-1:2012 - Condition monitoring and diagnostics of machines — Data interpretation and diagnostics techniques. Part 1: General guidelines, Edition 1, 2012.
13. ISO 13379-2:2015 - Condition monitoring and diagnostics of machines — Data interpretation and diagnostics techniques. Part 2. Data driven approach, Edition 1, 2015.
14. Bellini A., Filippetti F., Tassoni C., Capolino G. A. “Advances in diagnostic techniques for induction machines”, IEEE Transactions on Industrial Electronics, Volume: 55, Issue: 12, 2008.
15. Морозов А. Л. “Метод моментов дробного порядка и прибор на его основе для решения задач контроля и диагностики технического состояния электродвигателей”, Казанский национальный исследовательский технический университет им. А.Н. Туполева - КАИ, Казань, 2022.
16. Nabhan A., Nouby M., Sami A.M., Mousa M.O. “Bearing fault detection techniques - a review”, Turkish Journal of Engineering, Sciences and Technology, 2015.

17. Bazan G. H., Scalassara P. R., Endo W., Goedtel A., Godoy W. F., Palácios R. H. C. “Stator fault analysis of three-phase induction motors using information measures and artificial neural networks”, Electric Power Systems Research, Volume 143, 2017.
18. Faiz J., Ebrahimi B. M., Akin B., Toliyat H. A. “Comprehensive Eccentricity Fault Diagnosis in Induction Motors Using Finite Element Method”, IEEE Transactions on Magnetics, Volume 45, Issue 3, 2009.
19. Zolfaghari S., Noor S., Mehrjou M. R., Marhaban M. H., Mariun N. “Broken Rotor Bar Fault Detection and Classification Using Wavelet Packet Signature Analysis Based on Fourier Transform and Multi-Layer Perceptron Neural Network”, Applied Sciences, 2018.
20. Riera-Guasp M., Antonino-Daviu J. A., Capolino G. A. “Advances in electrical machine, power electronic, and drive condition monitoring and fault detection: State of the art”, IEEE Transactions on Industrial Electronics, Volume 62, 2015.
21. Trachi Y. “On induction machine faults detection using advanced parametric signal processing techniques”, Université de Bretagne occidentale, Brest, 2017.
22. Grieger J., Supangat R., Ertugrul N., Soong W. L., Gray D. A., Hansen, C. “Estimation of Static Eccentricity Severity in Induction Motors for On-Line Condition Monitoring”, Conference Record of the 2006 IEEE Industry Applications Conference Forty-First IAS Annual Meeting, 2006.
23. Сидельников Л. Г., Афанасьев Д.О. “Обзор методов контроля технического состояния асинхронных двигателей в процессе эксплуатации”, ISSN 2224-9923, Вестник ПНИПУ. Геология. Нефтегазовое и горное дело, 2013.
24. Садовников М. Е. “Надежность и диагностика электрооборудования: Учебное пособие к практическим занятиям”, Екатеринбург, Уральский государственный горный университет, 2003.
25. Сафин Н. Р. “Совершенствование методики токовой диагностики асинхронных двигателей с короткозамкнутым ротором”, Екатеринбург, 2017.
26. Шиндор О. В. “Методика контроля критических режимов работы высокоэнергетических установок на основе Вейвлет-анализа их нестационарных флуктуационных и шумовых сигналов”, Казань, 2015.
27. Ebeoğlu M. A., Güçlü S., Ünsal A., “Vibration Analysis of Induction Motors with Unbalanced Loads”, 10th International Conference on Electrical and Electronics Engineering (ELECO), 2017.
28. Kalinov A.P., Bratash O.V. “Analysis of Vibration Diagnostics Methods for Induction Motors”. Energetika. Proceedings of CIS higher education institutions and power engineering associations. 2012. (In Russ.)
29. Dalvand F., Kalantar A., Bevrani H., Member S., Shokoohi S. “Time-Domain Bearing Condition Monitoring in Induction Motors Using Instantaneous Frequency of Motor Voltage”, Smart Grid Conference (SGC), 2014.
30. Кан Ш., Микулович В. И. “Применение методов EMD для удаления шумов в вибрационных сигналах”, Белорусский государственный университет, кафедра радиофизики, Минск, 2009.
31. Alicando M. A. R., Ramos G. M., Ostia C. F. “Bearing Fault Detection of a Single-phase Induction Motor Using Acoustic and Vibration Analysis Through Hilbert-Huang Transform”, IEEE 13th International Conference on Humanoid, Nanotechnology, Information Technology, Communication and Control, Environment, and Management (HNICEM), 2021.

32. Delgado-Arredondo P. A., Morinigo-Sotelo D., Osornio-Rios R. A., Avina-Cervantes J. G., Rostro-Gonzalez H., Romero-Troncoso R. J. “Methodology for fault detection in induction motors via sound and vibration signals”, Mechanical Systems and Signal Processing Volume 83, 2017.
33. Singh G. K., Sa’ad Ahmed S. A. K. “Vibration signal analysis using wavelet transform for isolation and identification of electrical faults in induction machine”, Electric Power Systems Research, Volume 68, Issue 2, 2004.
34. Wang X., Peng T. F., Wu P. B., Cui L. T. “Influence of electrical part of traction transmission on dynamic characteristics of railway vehicles based on electromechanical coupling model”, Scientific Reports, Volume 11, 2021.
35. Wang H., Núñez A., Liu Z., Zhang D., Dollevoet R. “A Bayesian network approach for condition monitoring of high-speed railway catenaries”, Transactions on Intelligent Transportation Systems, Volume 21, 2020.
36. Wang, B., Xie S., Jiang C., Song Q., Sun S., Wang X. “An investigation into the fatigue failure of metro vehicle bogie frame”, Engineering Failure Analysis, Volume 118, 2020.
37. Lei Y., Wang K., Zhao L., Ge Q., Li Z., Li Y. “An improved torque and current pulsation suppression method for railway traction drives under fluctuating DC-link voltage”, IEEE Transactions on Power Electronics, Volume 33, Issue 10, 2018.
38. Chen J., Ni R., Li T., Qiu R., Lui Z. “The Harmonic Characteristic of The Advanced Synchronous SVPWM Overmodulation Strategy”. IEEE Access, Volume 7, 2019.
39. Zhang G., Tian Z., Tricoli P., Hillman S., Wang Y., Liu Z. “Inverter Operating Characteristics Optimization for DC Traction Power Supply Systems”, IEEE Transactions on Vehicular Technology, Volume 68, Issue 4, 2019.
40. Li R., Wang J., Zhao X., Li X. “Segmented Power Supply Preset Control Method of High-Speed Rail Contactless Traction Power Supply System considering Regenerative Braking Energy Recovery”, Mathematical Problems in Engineering, 2020.
41. Hao F., Zhang G., Chen J., Liu Z., Dongsheng X., Wang Y. “Optimal Voltage Regulation and Power Sharing in Traction Power Systems with Reversible Converters”, IEEE Transactions on Power Systems, Volume 35, Issue 4, 2020.
42. Guo J., Shi H., Li F., Wu P. “Field Measurements of Vibration on the Car Body-Suspended Equipment for High-Speed Rail Vehicles”, Shock and Vibration, 2020.
43. Ye Y., Sun Y. “Reducing wheel wear from the perspective of rail track layout optimization”, Proceedings of the Institution of Mechanical Engineers Part K Journal of Multi-body Dynamics, Volume 235, Issue 2, 2020.
44. Bao K., Zhang Q., Liu Y., Dai J. “Fatigue life of the welding seam of a tracked vehicle body structure evaluated using the structural stress method”, Engineering Failure Analysis, Volume 120 , 2021.
45. Li F., Wu P., Zeng J., Liu C., Wu H. “Vibration fatigue dynamic stress simulation under multi-load input condition: Application to metro lifeguard”, Engineering Failure Analysis, Volume 99, 2019.
46. Li F., Wu H., Wu P. “Vibration fatigue dynamic stress simulation under non-stationary state”, Mechanical Systems and Signal Processing, Volume 146, 2021.
47. Bokaeian V., Rezvani M. A., Arcos, R. “Nonlinear impact of traction rod on the dynamics of a high-speed rail vehicle carbody”, Journal of Mechanical Science and Technology, Volume 34, 2020.

48. Shi Y., Dai H., Wang Q., Wei L., Shi H. “Research on Low-Frequency Swaying Mechanism of Metro Vehicles Based on Wheel-Rail Relationship”, Shock and Vibration, 2020.
49. Lei Z., Wang Z. “Contact and creep characteristics of wheel-rail system under harmonic corrugation excitation”, Journal of Vibration and Control, Volume 27, Issue 17-18, 2020.
50. Ma, H., Zhang J., Zhang J., Jin T.T., Song C.Y. “Influence of Full-Life Cycle Wheel Profile on the Contact Performance of Wheel and Standard Fixed Frog in Heavy Haul Railway”, Shock and Vibration, 2020.
51. Zeng Z., Huang X., Wang J., Liu F., Wang W., Shuaibu A. “Wheel-rail stochastic dynamics and rail wear analysis of small radius curved sections of a tram line based on generalized probability density evolution”, Proceedings of the Institution of Mechanical Engineers, Volume 235, Issue 5, 2020.
52. Liu Q., Liang T., Dinavahi V. “Real-Time Hierarchical Neural Network Based Fault Detection and Isolation for High-Speed Railway System Under Hybrid AC/DC Grid”, IEEE Power & Energy Society General Meeting, 2021.
53. Xu K., Feng Z., Wu H., Xu D., Li F., Shao C. “Optimal profile design for rail grinding based on wheel-rail contact, stability, and wear development in high-speed electric multiple units”, Proceedings of the Institution of Mechanical Engineers, Volume 234, Issue 6, 2020.
54. Liu B., Yue H., Lin J., Wu X., Shi Z. “Analysis and Optimization of Driving Attitude and Oscillation Characteristics of Suspension-Type Small Rail Vehicles”, Shock and Vibration, 2020.
55. Lu Z., Wang X., Yue K., Wei J., Yang Z. “Coupling model and vibration simulations of railway vehicles and running gear bearings with multitype defects”, Mechanism and Machine Theory, Volume 157, 2021.
56. Liu J., Du S. “Dynamic Analysis of a High-Speed Railway Train with the Defective Axle Bearing”, International Journal of Acoustics & Vibration, Volume 25, Issue 4, 2020.
57. Huang C., Zeng J. “Dynamic behaviour of a high-speed train hydraulic yaw damper”, International Journal of Vehicle Mechanics and Mobility, Volume 56, Issue 12, 2018.
58. Wang Q., Zeng J., Wei L., Zhu B. “Carbody vibrations of high-speed train caused by dynamic unbalance of underframe suspended equipment”, Advances in Mechanical Engineering, Volume 10, Issue 12, 2018.
59. Li M., Ma M., Cao Z., Xia Q., Lui W. “Dynamic response analysis of train-induced vibration impact on the Probhutaratna pagoda in Beijing”, Earthquake Engineering and Engineering Vibration, Volume 20, 2021.
60. Lei S., Ge Y., Li Q. “Effect and its mechanism of spatial coherence of track irregularity on dynamic responses of railway vehicles”, Mechanical Systems and Signal Processing, Volume 145, 2020.
61. Zhang, W., Peng L., Zheng S., Guo X. “Research on the Simulation of Wheelset Response Characteristic Identification of Railway Fastener Loosening”, Mathematical Problems in Engineering, 2020.
62. Wang Z., Yin Z., Wang R., Cheng Y., Allen P., Zhang W. “Coupled dynamic behaviour of a transmission system with gear eccentricities for a high-speed train”, International Journal of Vehicle Mechanics and Mobility, Volume 59, Issue 4, 2021.
63. Zhang T., Chen Z., Zhai W., Wang K. “Establishment and validation of a locomotive–track coupled spatial dynamics model considering dynamic effect of gear transmissions”, Mechanical Systems and Signal Processing, Volume 119, 2019.

64. Wu P., Song C., Wang X., Qu S., Wu H. “Vibration Analysis of Traction Drive System Components Based on the Field Test for High-Speed Train”, Journal of Advanced Transportation, 2023.
65. Wang J., Yang J., Zhao Y., Bai Y., He Y. “Nonsmooth Dynamics of a Gear–Wheelset System of Railway Vehicles Under Traction/Braking Conditions”, Journal of Computational and Nonlinear Dynamics, 2020.
66. Lin F, Li X, Zhao Y, Yang Z. “Control Strategies with Dynamic Threshold Adjustment for Supercapacitor Energy Storage System Considering the Train and Substation Characteristics in Urban Rail Transit”, Energies 9 (4), 2016.
67. Wu Q., Wang B., Spiryagin M., Cole C. “Curving resistance from wheel-rail interface”, Vehicle System Dynamics, Volume 60, Issue 3, 2020.
68. Xu K., Zeng J., Wei L. “An analysis of the self-excited torsional vibration of high-speed train drive system”. Journal of Mechanical Science and Technology, Volume 33, 2019.
69. Chen H., Jiang B. “A Review of Fault Detection and Diagnosis for the Traction System in High-Speed Trains”, IEEE Transactions on Intelligent Transportation Systems, Volume 21, Issue 2, 2020.
70. Li R., Wang J., Zhao X., Li X. “Segmented Power Supply Preset Control Method of High-Speed Rail Contactless Traction Power Supply System considering Regenerative Braking Energy Recovery”, Mathematical Problems in Engineering, 2020.
71. Wang X., Peng T., Wu P., Cui L. “Influence of electrical part of traction transmission on dynamic characteristics of railway vehicles based on electromechanical coupling model”, Scientific Reports, 2021.
72. Liu D., Li T., Meng S., Lu Z., Zhong M. “Investigating the car-body vibration of high-speed trains under different operating conditions with full-scale tests”, International Journal of Vehicle Mechanics and Mobility, Volume 60, Issue 2, 2022.
73. Huang G. H., Zhou N., Zhang W. “Effect of internal dynamic excitation of the traction system on the dynamic behavior of a high-speed train”, Proceedings of the Institution of Mechanical Engineers-Part F: Journal of Rail and Rapid Transit, Volume 230, Issue 8, 2015.
74. Chang C., Ling L., Han Z., Wang K., Zhai W. “High-Speed Train-Track-Bridge Dynamic Interaction considering Wheel-Rail Contact Nonlinearity due to Wheel Hollow Wear”, Shock and Vibration, 2019.
75. Chen Z., Zhang B., Chen B., Fu J. “Development and evaluation of torque distribution methods for four-wheel independent-drive electric vehicle based on parameter estimation” Advances in Mechanical Engineering, 2019.
76. Wang Z., Mei G., Xiong Q., Yin Z., Zhang W. “Motor car-track spatial coupled dynamics model of a high-speed train with traction transmission systems” Mechanism and Machine Theory, Volume 137, 2019.
77. Wu H., Wu P., Xu K., Li J., Li F. “Research on Vibration Characteristics and Stress Analysis of Gearbox Housing in High-Speed Trains”, IEEE Access, Volume 7, 2019.
78. Yin Z., Zhang J., Lu H., Zhang W. “Dynamics modeling and analysis of a four-wheel independent motordrive virtual-track train”, Proceedings of the Institution of Mechanical Engineers-Part K: Journal of Multi-body Dynamics, Volume 235, Issue 1, 2021.
79. Mao L., Wang W. J., Liu Z., Yang G., Song C., Qu S. “Research on causes of fatigue cracking in the motor hangers of high-speed trains induced by current Buctuation”, Engineering Failure Analysis, 2021.

80. Wu P., Guo J., Wu H., Wei J. “Influence of DC-link voltage pulsation of transmission systems on mechanical structure vibration and fatigue in high-speed trains”, Engineering Failure Analysis, Volume 130, 2021.
81. Yao Y., Yan Y., Hu Z., Chen K. “The Motor Active Flexible Suspension and Its Dynamic Effect on the High-Speed Train Bogie”, Journal of Dynamic Systems, Measurement, and Control, 2018.
82. Lee H., Park C., Lee J. “Improvement of Thrust Force Properties of Linear Synchronous Motor for an Ultra-High-Speed Tube Train”, IEEE Transactions on Magnetics, Volume 47, Issue 11, 2011.
83. Wang Z., Yin Z., Allen P., Wang R., Xiong Q., Zhu Y. “Dynamic analysis of enhanced gear transmissions in the vehicle-track coupled dynamic system of a high-speed train”, International Journal of Vehicle Mechanics and Mobility, Volume 60, Issue 8, 2022.
84. Wang Z., Cheng Y., Mei G., Zhang W., Huang G., Yin Z. “Torsional vibration analysis of the gear transmission system of high-speed trains with wheel defects”, Proceedings of the Institution of Mechanical Engineers-Part F: Journal of Rail and Rapid Transit, 2019.
85. Yin H., Zhang X., Ma F., Gu C., Gao H., Wang Y. “New Equivalent model and Modal Analysis of Stator Core-Winding System of Permanent Magnet Motor with Concentrated Winding”, IEEE Access, Volume 8, 2020.
86. Wang S., Li H. “Analysis of Electromagnetic Vibration of Permanent Magnet Synchronous Motor under Static and Dynamic Eccentricity Fault”, 6th International Conference on Control and Robotics Engineering (ICCRE), 2021.
87. Lan H., Zou J., Xu Y., Liu M. “Effect of Local Tangential Force on Vibration Performance in Fractional-Slot Concentrated Winding Permanent Magnet Synchronous Machines”, IEEE Transactions on Energy Conversion, Volume 34, Issue 2, 2019.
88. Bogdevičius M., Karpenko M., Bogdevičius P. “Determination of rheological model coefficients of pipeline composite material layers based on spectrum analysis and optimization”, Journal of Theoretical and Applied Mechanics, 2021.
89. Wu Q., Zhang C., Qiu Y., Zhu F., Kong S. “Vibration and Noise Analysis for an Interior Permanent Magnet Synchronous Motor with Improved Structure”, Journal of Physics Conference Series, 2023.
90. Вибрации в технике: Справочник. В 6-ти т./Ред. В. Н. Челомей (пред.). – М.: Машиностроение, 1980 – Т. 3. Колебания машин, конструкций и их элементов/ Под ред. Ф. М. Диментберга и К. С. Колесникова. 1980. 544 с, ил.
91. Pennacchi P. “Nonlinear effects due to electromechanical interaction in generators with smooth poles”, Nonlinear Dynamics, Volume 57, 2009.
92. Gustavsson R., Aidanpaa J. “The influence of nonlinear magnetic pull on hydropower generator rotors”, Journal of Sound and Vibration, Volume 297, Issues 3, 2006.
93. Song Z., Ma Z. “Nonlinear vibration analysis of an eccentric rotor with unbalance magnetic pull”, Journal of Vibration and Shock, 2010.
94. Nässelqvist M. “Simulation and Characterization of Rotordynamic Properties for Hydropower Units”, Engineering, Environmental Science, 2009.
95. Arkkio A., Antila M., Pokki K., Simon A., Lantto E. “Electromagnetic force on a whirling cage rotor”, IEE Proceedings, Electric Power Applications, Volume 147, Issue 5, 2000.

96. Burakov A. “Modeling the unbalanced magnetic pull in eccentric-rotor electrical machines with parallel windings”, Doctoral Dissertation, Helsinki University of Technology, 2007.
97. Wiak S., Napieralska-Juszezak E. “Computed field models of electromagnetic devices”, Studies in Applied Electromagnetics and Mechanics, Volume 34, 2010.
98. Епифанов А. П. “Электромеханические преобразователи энергии”, Учебное пособие для вузов, Издательство ЛАНЬ, 2021.
99. Gieras J. “Advancements in Electric Machines”, Advancements in Electric Machines, 2008.
100. Левин Н., Серебряков А. “Силы одностороннего магнитного тяжения в аксиальных индукторных машинах”, Computer Modelling & New Technologies, Volume 6, 2002.
101. Touhami O., Noureddine L., Ibtiouen R., Fadel M. “Modeling of the induction machine for the diagnosis of rotor defects. Part. II. Simulation and experimental results”, IEEE Industrial Electronics Society, 2005.
102. Баннов Д. “Метод диагностики обрывов стержней ротора в асинхронных электродвигателях на основе регрессионного анализа модуля результирующего вектора тока статора”, Известия Томского политехнического университета, Инжиниринг георесурсов, 2022.
103. Funk T., Usynin Yu., Grebnev A., Ponosov D. “Mathematical model of induction motor with series-connected stator and rotor windings”, Вестник ЮУрГУ, «Энергетика», 2017.
104. Mazur D., Trojnar M. “Modelling of electrical and mechanical phenomenain induction motors with air-gap eccentricity”, Renewable Energy and Power Quality Journal, 2003.
105. Кулак И., Полетаев В. “Конструкторско-технологическая модель воздушного зазора взрывозащищенного асинхронного двигателя”, Вестник КузГТУ, 2006.
106. Полетаев В. “Обеспечение точности выходных энергетических показателей взрывозащищенных асинхронных двигателей”, 2000.
107. Brinovar I., Srpčič G., Seme S., Štumberger B., Hadžiselimović M. “The classification of explosion-proof protected induction motor into adequate temperature and efficiency class”, AIP Conference Proceedings, Volume 1866, Issue 1, 2017.
108. Хоменко, А. “Разработка системного метода управления вибрационным состоянием подвижного состава”, Иркутск, 2000.
109. Goolak S., Liubarskyi B., Lukoševičius V., Keršys R., Keršys A. “Operational Diagnostics System for Asymmetric Emergency Modes in Traction Drives with Direct Torque Control”, Applied Sciences, 2023.
110. Гусев А., Новоселова М. “Прикладная теория колебаний”, Учебное пособие, Тверской государственный технический университет, Тверь, 2017.
111. Вульфсон И. “Краткий курс теории механических колебаний”, Библиотека ВНТР, 2017.
112. Куцубина Н., Санников А. “Теория виброзащиты и акустической динамики машин”, Учебное пособие, Министерство образования и науки РФ, Урал. гос. лесотехн. ун-т. – Екатеринбург, 2014.
113. Dvornikov I., Marinbahs M., Sliskis O., Ketners K. “Investigation of autonomous traction motor dynamic using method of mutual loading and computer simulation”, IEEE 59th

International Scientific Conference on Power and Electrical Engineering of Riga Technical University (RTUCON), Latvia, 2018.
114. Kobenkins G., Marinbahs M., Burenin V., Zarembo J., Sliskis O. “Carrying Out of Strenght Tests of Geared Motor Box as Part of a Frequency-Controlled Traction Electric Drive”, 17th Conference on Electrical Machines, Drives and Power Systems (ELMA), Bulgaria, 2021.
115. Dvornikov I., Marinbahs M., Kobenkins G., Sliskis O., Ketners K. “Carrying Out of Tests for the Functionality of the Traction Autonomous Drives in the Conditions of Industry and Serial Production”, 17th Conference on Electrical Machines, Drives and Power Systems (ELMA), Bulgaria, 2021.
116. Kobenkins G., Marinbahs M., Burenin V., Zarembo J., Bizans A., Sliskis O. “Determination of the Level of Own Vibration of Geared Motor Boxes in Industrial Conditions” IEEE 62nd International Scientific Conference on Power and Electrical Engineering of Riga Technical University (RTUCON), Latvia, 2021.
117. Kobenkins G., Marinbahs M., Bizans A., Rilevs N., Burenin V., Sliskis O. “Carrying Out of Strength Control of Mutual Loaded Traction Geared Motor Boxes as a Part of Industrial Tests”, 9th International Conference on Electrical and Electronics Engineering (ICEEE), Turkey, 2022.
118. Sheen Y. “A complex filter for vibration signal demodulation in bearing defect diagnosis”, Journal of Sound and Vibration, Volume 276, Issues 1, 2004.
119. WIKOV MGI // EG2Tv 08-805209-01, Calculation of the strength of the gearbox housing, Hronov, 2019, p. 49.
120. Marinbahs M., Kobenkins G., Pavelko V. Bizans A., Rilevs N., Sliskis O. “Determination of the Strength Characteristics of Traction Gears Under Shock Loads”, International Youth Conference on Energy (IYCE-2022), Hungary, 2022.
121. Umbrajkaar A., Krishnamoorthy A., Dhumale R. “Vibration Analysis of Shaft Misalignment Using Machine Learning Approach under Variable Load Conditions Shock and Vibration, 2020.
122. Lee S., Stone G., Antonino-Daviu J., Gyftakis K., Strangas E., Maussion P., Platero C. “Condition Monitoring of Industrial Electric Machines: State of the Art and Future Challenges”, IEEE Industrial Electronics Magazine, Volume 14, Issue 4, 2020.
123. Ocak H., Loparo K. “A new bearing fault detection and diagnosis scheme based on hidden Markov modeling of vibration signals”, IEEE International Conference on Acoustics, Speech, and Signal Processing, Proceedings, USA, 2002.
124. Русов В. “Спектральная вибродиагностика”, Вибро-центр, 1996.
125. Erkhan F., Korneychuk N., Bomeshko E. “The impact of bearing shield wear on the power factor of ac electric motors”, Pridnestrovian State University named after T. G. Shevchenko, 2020.
126. Селицкая О. “Ремонт электрооборудования”, Курсовое проектирование: учебно-методическое пособие, БГАТУ, Минск, 2018.
127. Копылов И. “Проектирование электрических машин 4-е изд., пер. и доп. Учебник для бакалавров”, Litres, 2019.
128. Барков А., Жуковский Д., Грищенко Д. “Новое поколение систем мониторинга и диагностики роторного оборудования”, Химическая техника, 2016.

129. Tiboni M., Remino C., Bussola R., Amici C. “A Review on Vibration-Based Condition Monitoring of Rotating Machinery”, Applied Sciences, 2022.
130. Malla C., Panigrahi I. “Review of Condition Monitoring of Rolling Element Bearing Using Vibration Analysis and Other Techniques”, Journal of Vibration Engineering & Technologies, 2019.
131. Marinbahs M. “Study of the Dynamics, Strength and Technical Condition Assessment of Traction Electromechanical Equipment”, RTU Press, 2023.
132. Suresh S., Naidu V. “Gearbox Health Condition Monitoring Using DWT Features”, Proceedings of the 6th National Symposium on Rotor Dynamics, 2021.
133. Gierlak P., Burghardt A., Szybicki D., Szuster M., Muszynska M. “On-line manipulator tool condition monitoring based on vibration analysis”, Mechanical Systems and Signal Processing, Volume 89, 2017.
134. Dvorņikovs I. “Virtual-Physical Tests of Vehicles with Combined Traction Electrical Drive”, PhD Thesis, Riga, 2021.
135. Ehya H., Lyng Rødal G., Nysveen A., Nilssen R. “Condition Monitoring of Wound Field Synchronous Generator under Inter-turn Short Circuit Fault utilizing Vibration Signal”, 23rd International Conference on Electrical Machines and Systems (ICEMS), Hamamatsu, Japan, 2020.
136. Sharma V. “A Review on Vibration-Based Fault Diagnosis Techniques for Wind Turbine Gearboxes Operating Under Nonstationary Conditions”, Journal of The Institution of Engineers, 2021.

Genādijs Kobenkins was born in 1996 in Riga. He obtained a Bachelor's degree in Electrical Engineering (2018), a qualification of an engineer in Power Engineering and Electrical Engineering (2019), and a Master's degree in Power Engineering and Electrical Engineering (2020) from Riga Technical University. Since 2018, he has been a design engineer in the Electrical Machines office at JSC "Riga Electrical Machinery Factory". Since 2021, he has been a Scientific Assistant at Riga Technical University. He has participated in several scientific conferences and symposia, where he presented the latest research in the field of electrical machine vibrations. His scientific interests are related to the discovery and solution of problems in the design, testing and operation of electrical machines.